VRIJE
UNIVERSITEIT
BRUSSEL

SUPERCONDUCTING DOMAIN WALLS

Master Thesis

Ruben Camphyn

2022- 2023

Prof. A. Mariotti, Dr. Simone Blasi, Aäron Rase

Science and Bio-Engineering Sciences

It's still magic even if you know how it's done.

–Terry Pratchet, from A Hat Full of Sky

Abstract

The Standard Model of particle physics successfully describes the elementary particles and their interactions. However, there remain open questions in fundamental high energy physics that should be solved. To address these issues, several Beyond the Standard Model (BSM) theories have been proposed. In many of these, the symmetry group of the Standard Model is embedded in a larger symmetry group. This larger group must spontaneously break down during the history of the universe to obtain the Standard Model as it is observed today. The breaking down of such a group occurs in the early universe and is called a phase transition. This process can lead to interesting physical effects. One class of these effects, called topological defects, is studied in this thesis. Topological defects are stable non-trivial solutions of the field theory that contain some energy density and are created at the phase transition. The dynamics of these topological defects can be a source for Gravitational Waves (GW), which travel through the Universe. By observing such cosmological GWs, we can infer information about early universe physics, information that could be traced back to an era even before the Cosmic Microwave Background (CMB) emission. This thesis studies the subject of topological defects and their emission of GWs, while focussing on the possibility that they behave like superconductors.

Acknowledgement

This work did not come to fruition on its own.

I would like to thank Professor Alberto Mariotti for his insights into the structure and physics behind this thesis. He was always available when needed, no matter the hour (a fact which I used extensively in the weeks leading up to the deadline) and I could not wish for a better promotor.

My co-promotor Aäron Rase is definitely the reason that this thesis came to its current quality. His coding skills and gravitational wave expertise were essential in finding the current results. Apart from that he was always available for a chat and to keep up the mental. I feel confident in saying that this thesis would not be finished without his help.

I would also like to thank Dr. Simone Blasi. His calculations and theoretical interpretations of superconductors led me to gain a much better understanding of the physics behind this thesis

Of course my family must be thanked as well. Mama, papa en zusje, thank you! You kept me going throughout the work and never failed to call me for a "koffiepauzetje". Their support is what made me the person I am today.

My girlfriend Jennifer Pham Van was critical in keeping the good work going. She always kept me ready to push on and has supported me throughout this whole year. Her encouragement is what made me get up every day to put all my effort into my work. At times when I felt down, she was there to pick me up.

Tristan Boen is also to thank for keeping me company when going to work in the SBC every day. His comments throughout the day kept me from going into full stress mode.

Last but not least I would like to thank my grandparents. Their call every week about updates on life gave me an excuse to talk about my work and lighten the load.

Contents

1 Introduction

In 2015, the LIGO collaboration made the first direct detection of a Gravitational Wave (GW) signal [1]. This heralded the start of a new era of research, in which gravitational wave measurements can be used to probe further than ever into the early Universe. This can be especially important in cosmology. Gravitational waves could lead to measurements beyond the Cosmic Microwave Background (CMB), the furthest back a photon detector can explore. This era of the Universe is home to a plethora of interesting structures and physics. In particular, in these early stages of the Universe there could be information about physics Beyond the Standard Model of particle physics (BSM).

While the Standard Model (SM) is one the greatest successes of modern physics [2], there are still some areas in which improvements can be made. Examples include dark matter [3], baryon asymmetry [4] and gauge coupling unification [5]. These and other problems are addressed in theories Beyond the Standard Model. In these theories, the symmetry group of the Standard Model is often enlarged to a bigger group, with new forces emerging at high energies. This larger group should spontaneously break into the SM group as to be compatible with current experimental observations [6].

However, in the early stages of the Universe, when the temperature was very high, we expect that the large symmetry group in these BSM theories is restored. Then, as the Universe cools down, a phase transition occurs that leads to the breaking of this larger group into the SM group. Therefore, phase transitions in the early Universe are common predictions of BSM theories.

Actually an example of a phase transition is already present in the SM, since the electroweak symmetry group $SU(2)_L \times U(1)_Y$ is spontaneously broken to $U(1)_{EM}$ around a temperature of order $T \sim O(100)$ GeV.

Generally, phase transitions allow for interesting physics in the early Universe. In this thesis, we focus on the phase transitions that can emerge in BSM theories with enlarged symmetries. As mentioned, moments after the Big Bang the Universe consists of a hot and dense plasma in which the temperatures are high enough to restore this larger symmetry group. As the Universe expands, it cools down and at a certain critical temperature the symmetry group spontaneously breaks into the known SM group. This process of transitioning between an unbroken and broken symmetry is the phase transition and it can be a source of new phenomenological signatures. In particular, the phase transitions can generate topological defects, which are the main focus of this thesis.

Among these, the two lowest dimensional examples of topological defects are investigated: strings and domain walls. It is the goal of this thesis to explore the underlying theories that lead to the formation of topological defects and consider their properties.

We split this task in three main subjects: the theory of topological defects and their configurations; their emission of gravitational waves and the possibility to generalise their theories to superconducting topological defects. These three subjects are broadly introduced in Chapter 2, after which the thesis specialises. Chapter 3 focuses on $1+1$

dimensional topological defects, cosmic strings. Their field theory is investigated and a numerical analysis is applied to compute the solutions to their equations of motion. Inspired by the work of Edward Witten [7], a re-elaboration of this theory is considered in Chapter 4. These computations serve to illustrate that cosmic strings can behave as superconductors and can even be charged by the cosmic plasma. The stability of this configuration is investigated and a proof for the superconductivity is provided.

After completing the string discussions, we can generalise these theories to $2 + 1$ dimensional topological defects, the domain walls. Chapter 5 introduces this new theory and again applies a numerical algorithm to solve the equations of motion. We perform calculations to approximate the domain wall properties and provide the parameterisations of their gravitational wave signal.

Subsequently, in Chapter 6, we aim to create a theory for superconducting domain walls. The stability of such a configuration is shown and a proof is built to show that domain walls can be superconducting in a similar manner to cosmic strings. We explore the dynamics of domain walls in the early Universe by identifying two regimes that dominate in different circumstances. One of these, the friction regime, is introduced and its impact on the domain walls is discussed. Afterwards, we show how this new type of domain walls interacts with photons, using a numerical algorithm to calculate their reflection coefficients.

Finally, Chapter 7 aims to elaborate more on the properties of superconducting domain walls, in particular their behaviour in the early Universe's cosmic plasma. The parameter space is explored with the goal of connecting a prediction of their dominant behaviour with the sensitivities of current and future gravitational wave experiments. We estimate the impact of friction on superconducting domain walls using the reflection coefficient computations from the previous chapter.

Throughout the discussion on domain walls their gravitational wave spectrum is introduced. After introducing the concepts of gravitational waves in Chapter 2, the power and spectrum of gravitational waves emitted by domain walls is specified upon in Chapter 5. These gravitational wave emissions allow us to link domain walls in the early Universe to current experiments in Chapter 7.

A graphical overview of the thesis is provided in Figure 1.1. The colors of the boxes are added to differentiate the topological defects on which the chapters focus, with the exception of the theoretical introduction. In addition a color code is used to distinguish the sections which are respectively: i) a review of existing results, ii) independent re-derivations of existing results and iii) original derivations and results.

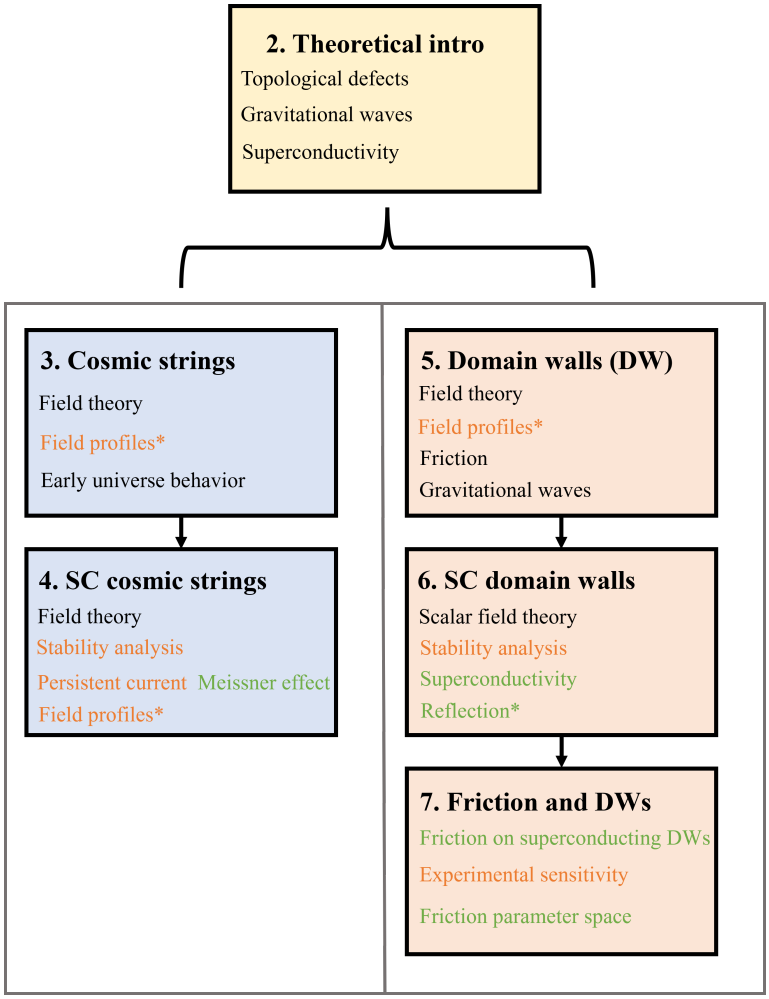

Figure 1.1: A graphical overview of the structure of the thesis. The boxes denote different chapters. Subjects colored in black denote a review of existing results, orange denotes independent re-derivations of existing results and green subjects denote original derivations and results. The asterisks denote subjects for which a numerical analysis was developed.

With this structure in hand, we can begin the study of topological defects and their superconductivity.

2 Theoretical Introduction

This chapter aims to provide a basic theoretical understanding of topological defects, gravitational waves and superconductivity. This to ease the reader into the world of these three basic domains, which will be connected later on in the thesis. No original work was performed in this chapter, rather it is an overview of the theoretical foundation on which this thesis relies.

Throughout this thesis the mostly minus convention, also known as the West Coast convention, will be used for raising and lowering indices.

$$g_{\mu\nu} \coloneqq (+,-,-,-). \tag{2.1}$$

The covariant derivative is defined as:

$$D_\mu \coloneqq \partial_\mu + ieA_\mu. \tag{2.2}$$

All quantities are defined in natural units $\hbar = c = 1$.

2.1 Topological defects

This thesis will start with a general discussion of topological defects. They will be introduced by ways of a simple example of what will be the most important topological defect in this work: a domain wall. The importance of topological defects in the early Universe will be discussed as well as their formation mechanism.

The Standard Model is built on symmetries. From Noether's theorem to the Brout-Englert-Higgs (BEH) mechanism and unto theories of grand unification and quantum gravity, theoretical physics has benefitted greatly from finding order in nature. Conservation of linear momentum is linked to translational invariance, angular momentum to rotational invariance and energy conservation can be traced back to a time symmetry. The fundamental interactions of the Standard Model i.e. the Electroweak and Strong forces, can be explained on the basis of gauge symmetries. The gauge group of these symmetries $SU(3) \times SU(2)_L \times U(1)_Y$, composes the general structure of Standard Model physics.

An important note in the history of the Universe is that these symmetry groups are not static. Indeed, during the cooling of the Universe, the electroweak symmetry was broken to the $U(1)$ symmetry of electromagnetism. This happened when the Universe was still very young, fractions of a second after the big bang, at a temperature of $T_{EW} \sim 100$ GeV. Grand unification theories aim to unite the whole Standard Model into one symmetry group G, which was reduced at several times after the Big Bang to eventually yield the Standard Model as it is now [8]. Such a transition can be understood as

a phase transition: the Universe changes from a phase with symmetry to a phase where the symmetry is broken. During such a phase transition topological defects can form. The classical example is that of ice forming on a lake. As the lake freezes over different patches begin forming ice. After a while these patches have grown enough to touch until the whole lake has frozen over. Yet what one sees is not a perfect continues plane of white ice. Cracks have formed all over the lake due to the patchy formation of the ice surface. These cracks are the topological defects.

Topological defects are not only a strange phenomena of Early Universe Cosmology. They can be spotted in all sorts of phase transitions. Take for example magnetism. It is customary in this field to denote the magnetic moment in a medium with an arrow. Aligning all arrows yields a magnet as one could stick on the fridge. For some types of ferromagnets the ideal lowest energy configuration is the one as shown in Figure 2.1. In this case domains of different alignments, but equal energy, have formed. The arrows cannot just flip discontinuously when changing domains, hence they gradually turn to achieve a continuous transition. This is called a domain wall in micromagnetism. This configuration does not exhibit the lowest energy, yet remains stable due to the continuous interpolation between two equivalent energy states. In other words, the system would need to increase its energy to transform the whole magnet into one domain, so it is energetically more favourable to keep the domain walls [9].

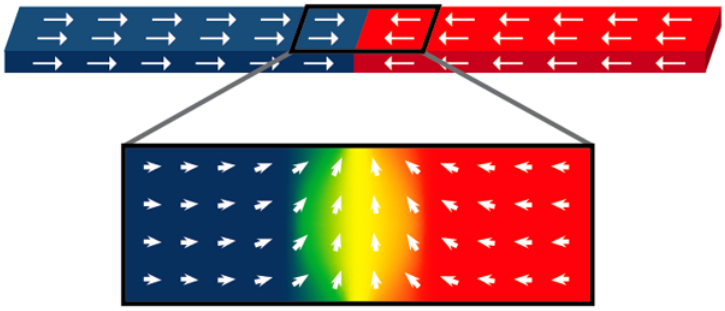

Figure 2.1: Demonstration of a domain wall in a ferromagnet. Both domains, made up of left and right pointing arrows respectively, are in a state of lowest energy. To interpolate between the two domains the arrows gradually change their orientation. Keeping this setup is energetically more favourable than flipping all arrows of one domain. The area in which the arrows change direction is defined as the domain wall. Illustration from [10].

2.1.1 Introductory example

A topological defect is a solution to the equations of motion of the system that diverts from the lowest energy state, but is stable when affected by small perturbations. To introduce this concept, it is perhaps best to start with an example. One of the most

well known and simplest models of a topological defect is the ϕ^4 kink. Consider a real scalar field ϕ with corresponding Lagrangian [11]

$$\mathcal{L} = \frac{1}{2}(\partial_\mu \phi)(\partial^\mu \phi) - V(\phi), \tag{2.3}$$

with a potential given by

$$V(\phi) = \frac{\lambda}{4}(\phi^2 - \eta^2)^2. \tag{2.4}$$

The shape of this potential is shown in Figure 2.2.

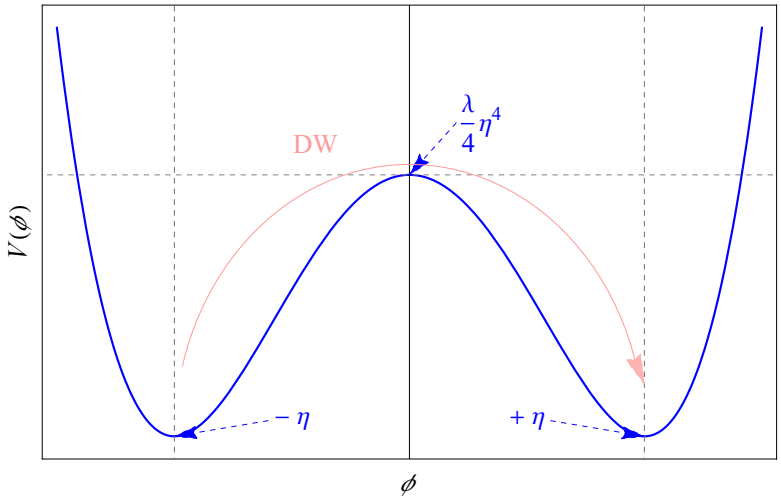

Figure 2.2: Sketch of the potential of the ϕ^4 kink as given in Equation (2.4). The minima of the fields at $\pm\eta$ are indicated. The top of the potential hill is located at $\phi = 0$ and yields a value $V(0) = \frac{\lambda}{4}\eta^4$. The behaviour of a domain wall's extrapolation is illustrated in pink.

One can see that the potential exhibits a Z_2 symmetry: two minima exist at $\phi = \pm\eta$. These two extrema share the same vacuum energy and hence a scenario is plausible where two distinct regions exist in which the system takes on a different vacuum expectation value (vev) in each. Imagine a Universe which exhibits two such regions, divided by the $xy-$plane at the origin. Negative z values take on the negative minimum and vice-versa:

$$\begin{cases} \phi(x^\mu) & = +\eta \quad z > 0, \\ \phi(x^\mu) & = -\eta \quad z < 0. \end{cases} \tag{2.5}$$

Since this setup is Lorentz invariant in the xy-plane, the solution only depends on the coordinates (t, z). Assuming this configuration to be static, the equation of motion of

$\phi(x^\mu) = \phi(z)$ is:

$$\partial_z^2 \phi = \lambda(\phi^2 - \eta^2)\phi. \tag{2.6}$$

The solution to this equation of motion is given by

$$\phi(z) = \eta \cdot \tanh\left(\sqrt{\frac{\lambda}{2}}\eta z\right). \tag{2.7}$$

The shape of this solution can be seen in Figure 2.3.

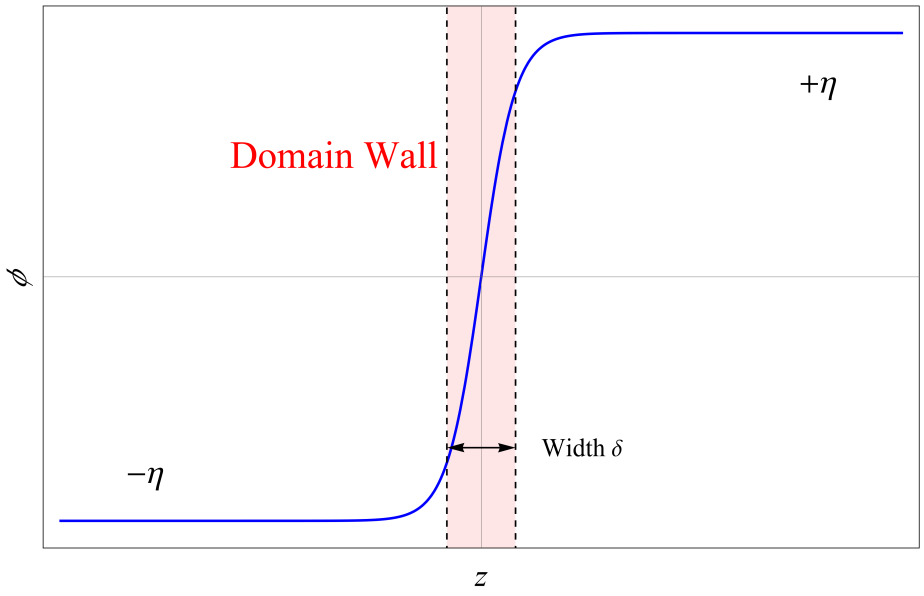

Figure 2.3: Sketch of the solution extrapolating between the two minima given in Equation (2.7). The width δ of the domain wall is illustrated by the dashed lines.

This boundary between two different valued regions is again a domain wall and is an example of a topological defect: a solution with a non-trivial space-time profile for the field that is stable despite not complying with the lowest energy state of the system. Both regions are in their minimal energy configuration, while the transition region is not. The transition region forms a two-dimensional surface (in the $x - y$ directions) in space-time that we identify as a domain wall. This configuration is classically stable since it would require energy to "pull" one of the regions to the *vev* of the opposing region. In other words, energy is needed to cross the potential hill between the two minima seen in Figure 2.2.

Since this configuration is non-trivial, as in that it is not set to the lowest energy value everywhere and the field possesses a gradient, the domain contains a non zero energy density. This energy is most often quoted as the tension σ of a domain wall, the energy per area unit. This is most often used since the width δ of a domain wall can be

seen as small and it is hence easier to observe domain walls as $2+1$-dimensional objects. To illustrate this, both quantities can be calculated in this example. To first order the solution $\phi(z)$ in Equation (2.7) can be written as

$$\phi(z) \approx \eta^2 \sqrt{\frac{\lambda}{2}} z. \tag{2.8}$$

And hence the length scale over which this approximation extrapolates between $\phi(\delta) = -\eta$ and $\phi(\delta) = +\eta$ is $\delta = \frac{\sqrt{2}}{\sqrt{\lambda}\eta}$. The same first order expansion can be used to guess the order of the energy density ρ at $z = 0$ as the sum of the kinetic and potential part of the Lagrangian density. This yields $\rho \sim \lambda\eta^4$. Note that since the only dimensionfull parameter is η, a relation like this was expected. Combining the width and energy density yields an expression for the tension: $\sigma = \rho \cdot \delta \sim \sqrt{\lambda}\eta^3$.

The tension for this example can also be calculated exactly by calculating the energy-momentum tensor of the Lagrangian and plugging in the analytical solution. The definition of the energy-momentum tensor is given by

$$T^{\mu\nu} = \frac{\partial \mathcal{L}}{\partial(\partial_\mu \phi)} \partial^\nu \phi - g^{\mu\nu} \mathcal{L}. \tag{2.9}$$

Substituting in the solution yields

$$T^{\mu\nu} = \partial^\mu \phi \partial^\nu \phi - g^{\mu\nu} \left(\frac{\lambda}{4} (\phi^2 - \eta^2)^2 \right). \tag{2.10}$$

The zero'th component represents the energy density and can be calculated as

$$\Rightarrow \quad T^0_{\ 0} = \frac{\lambda}{2} \eta^4 \operatorname{sech}^4(\sqrt{\frac{\lambda}{2}} \eta z). \tag{2.11}$$

Since domain walls can often be approximated as two-dimensional objects, an area density is of particular use. To obtain this area density, called the tension, one can integrate over the direction perpendicular to the domain wall plane.

$$\Rightarrow \quad \sigma = \int dz T^0_{\ 0} = \frac{2\sqrt{2}}{3} \sqrt{\lambda} \eta^3. \tag{2.12}$$

This validates the approximations made before. Such a non zero tension also hints that any closed domain wall, imagine for example a closed sphere of radius R, will want to collapse when there are no other forces in play. The energy of such a sphere is area $\times$

tension $\sim R^2\sigma$. Hence to minimise energy a closed domain wall tends to shrink $R \to 0$ and collapses. One can also imagine such a sphere to be charged, the charges in the surface will then oppose the contraction.

Note that the Universe is not empty and the tension will not be the only quantity dictating the motion of a domain wall. Although this will be discussed more in detail later, a domain wall can interact with the plasma making up the early Universe and hence will feel a friction force.

This short subsection introduced briefly the main properties of a domain wall: its profile, width δ and tension σ. This was done by observing one of the most simple potentials, the ϕ^4-kink, that can form domain walls as a solution to its equations of motion.

2.1.2 Spontaneous symmetry breaking

Now that the concept of topological defects, more specifically domain walls, has been introduced, it is possible to connect the concept of a topological defect to spontaneous symmetry breaking. It is the goal of this short section to show how the structure of spontaneous symmetry breaking allows for different topological defects. The discussion that follows is based on [11–13].

The simple example from the previous section already illustrated the concept of spontaneous symmetry breaking. The Lagrangian exhibits a Z_2 symmetry, yet applying such a transformation on the groundstates changes them from *vev* to $-vev$ and vice-versa. A better known example of spontaneous symmetry breaking is the Brout-Englert-Higgs mechanism (BEH), in which a scalar $SU(2)$ doublet, the Higgs field, lives on a Mexican hat potential. This potential and the Lagrangian describing the Higgs field dynamics exhibit a $SU(2) \times U(1)$ symmetry. Choosing a *vev* in the valley of groundstates, at the bottom of the potential, makes no change to the Lagrangian, which still looks to retain the original symmetry, but the groundstate is no longer symmetric. A symmetry transformation moves the groundstate around the valley at the bottom of the Mexican hat.

In a more general sense, consider a Lagrangian symmetric under a group G. Imagine picking a groundstate which breaks the symmetry group into a group H i.e. applying symmetry transformations from inside H on the groundstate leaves the groundstate invariant, while transformations outside of H do change the groundstate. The space of all possible vacua is called the vacuum manifold $\mathcal{M}$. Mathematically this manifold is given by the coset space G/H. In case of the BEH mechanism, the valley at the bottom of the Mexican hat is exactly this vacuum manifold.

It is the structure of this manifold that dictates what type of topological defects can arise. In the case of the example of Subsection 2.1.1 the vacuum manifold exists of two disconnected parts: $\mathcal{M} = \{-\eta, +\eta\}$. Any vacuum manifold made out of disconnected

components allows for the formation of domain walls, since these disconnected components allow for the formation of distinct regions with different vev's. Scalar fields can interpolate between these regions by forming domain walls.

Homotopy theory classifies manifolds by the possible homotopies that can be formed between the n-sphere S^n and the manifold. The homotopy groups $\pi_n(\mathcal{M})$ consists of all equivalence classes of $n-$spheres in the manifold. As an example consider the statement $\pi_1(\mathcal{M}) = 1$ i.e. the 1^{st} homotopy group is trivial. This means that any $1-$sphere on the vacuum manifold $\mathcal{M}$ can be continuously deformed in any other $1-$sphere on the manifold. Hence there are no holes in the surface of the manifold, since a circle drawn around such a hole would be unable to continuously transform into a circle that does not contain the hole.

As another example consider the statement $\pi_0(\mathcal{M}) \neq 1$.The 0^{th} $n-$sphere is nothing more than a line. Hence this statement can be interpreted as the vacuum manifold having two or more regions between which one cannot draw a line. In other words it is made up of distinct regions. This is exactly the condition previously stated to allow for domain wall formation. Table 2.1 allows for a brief overview of topological defects and their associated homotopy groups.

Homotopy group	Topological defect
$\pi_0(\mathcal{M}) \neq 1$	Domain walls
$\pi_1(\mathcal{M}) \neq 1$	Strings
$\pi_2(\mathcal{M}) \neq 1$	Monopoles
$\pi_3(\mathcal{M}) \neq 1$	Textures

Table 2.1: An overview of topological defects and their non trivial homotopy groups.

2.1.3 Phase transitions

Now that spontaneous symmetry breaking and its connection to topological defects was introduced, this work can elaborate on how these spontaneous symmetry breakings occur in the early Universe. At the end of this subsection, the reader should have an understanding of how a field theory can evolve from one symmetry into another. The crux of the discussion will be that a broken symmetry can be restored at higher temperatures.

As a starting point, consider that the potentials up till now were all treated in a classical way. When discussing a potential in the quantum realm, one has to take into account all higher order Feynman diagrams i.e. allowing for loop diagrams. These radiative corrections, as they are called, can be integrated into the potential by using a series expansion in the number of loops. A potential obtained in this way is called an effective potential. The 0^{th} order of this series expansion is the tree-level classical potential.

$$V_{eff} = V_{\text{tree level}} + V_{\text{one loop}} + V_{\text{two loops}} + ... \tag{2.13}$$

To study phase transitions in the early Universe, one has to consider the Universe filled with a perfect fluid of particles i.e. consider a thermal bath and the temperature corrections that come along with it. Thermodynamically speaking, the temperature dependent system will try to minimise its Helmholtz free energy F, by compensating a decrease in temperature T with an increase in entropy S, thus changing the phase. The entropy is a measure of the "chaos" in a system. Hence, in increasing the entropy, an ordered system, like e.g. a solid, transitions to a more chaotic system like a gas.

$$F = H - TS, \tag{2.14}$$

The field important to the electroweak symmetry breaking is the Higgs field, which will be denoted as ϕ. The Higgs field influences the perfect fluid by setting the masses of the particles. The lighter the mass of a particle the more "potential for chaos" a particle has i.e. a lower mass allows for a bigger phase space. In this way changing the expectation value of the Higgs field, changes the mass, which in turn changes the entropy.

The current model of the Universe states a very hot Universe at the Big Bang. The Helmholtz free energy is then reduced to $F \approx -TS$ and a higher entropy S is achieved by lowering the masses of the relevant particles. To lower the masses the Universe demands that the expectation values of the Higgs field are 0, hence at higher temperatures the electroweak symmetry is restored.

After this extremum the temperature lowers and the enthalpy term H becomes important. This term's behaviour can be seen as the system relaxing to a minimal energy state at zero temperature. Hence at a certain critical temperature T_c, the Higgs expectation value will evolve to the 246 GeV it measures today. To calculate this, a mathematical description of the Helmholtz free energy is needed. Weinberg [14], Dolan & Jackiw [15] and Kirzhnits & Linde [16] developped these formalisms. These calculations come to the conclusion that the Helmholtz free energy can be modelled as an effective potential.

In this description, the effective potential gets further temperature dependent corrections with respect to the ones in (2.14). We will not review the derivation of the temperature dependent corrections in this thesis. References as stated previously or reviews like [17, 18] can be consulted for a much more thorough derivation of these ideas. In the following we employ the temperature dependent effective potential to discuss the dynamics of phase transitions in the early Universe.

To cement these concepts, a simple example could prove to be helpful. Again consider the first example given in Equation (2.4). The lowest order correction to this potential is:

$$V_{eff}(\phi, T) = \frac{\lambda}{4}(\phi^2 - \eta^2)^2 + \frac{\lambda}{12}T^2\phi^2, \tag{2.15}$$

which indeed reduces back to the original potential for $T = 0$. This potential already carries information about the phase transition. Observe Figure 2.4, in which the potential is sketched for different temperatures. By dimensional analysis of the problem, one can already guess that the critical temperature should be of order η. At high temperatures $T > T_c$, the potential reduces to a simple parabola with a single minimum at $\phi = 0$. As the temperature lowers, the potential gradually relaxes into the original shape with two distinct minima. This allows the system to pick a non zero minimum as illustrated by the red arrow in the plot.

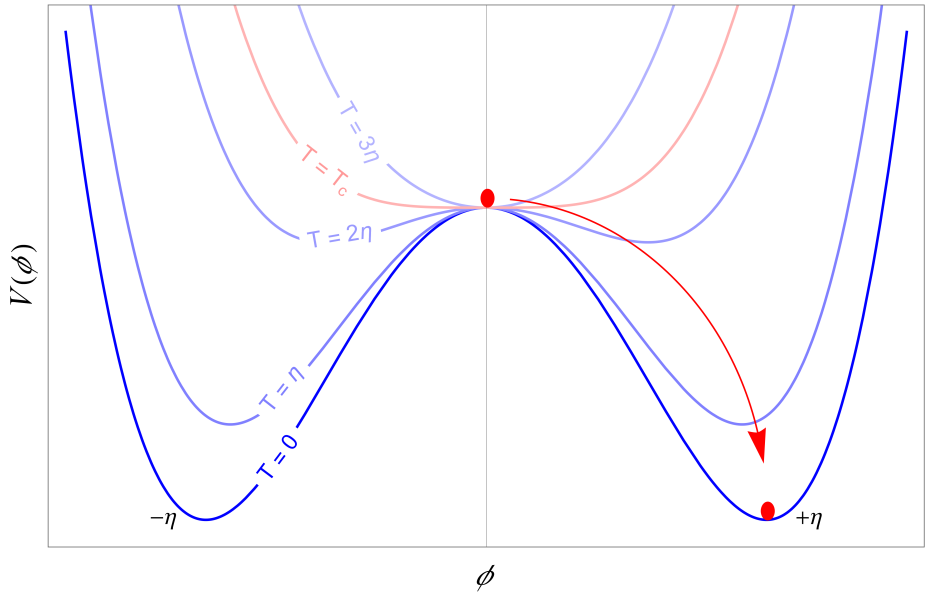

Figure 2.4: Sketch of the effective potential behaviour as the temperature changes from $T > T_c$ (lighter) to $T < T_c$ (darker). The red points denote minima of the system at $T > T_c$ and $T < T_c$ respectively. The red arrow sketches one of the direction in which the minima changes as the temperature decreases.

The critical temperature of the system can be found by calculating the minima of the effective potential in function of the temperature T.

$$\partial_\phi V_{eff} = 0 \Leftrightarrow \phi_\pm = \pm\frac{\sqrt{-T^2 + 6\eta^2}}{\sqrt{6}} \vee \phi_0 = 0. \tag{2.16}$$

Substituting these value into the potential, one can calculate the temperature for which their values are equal as

$$V_{eff}(\phi_0) = V_{eff}(\phi_\pm) \Leftrightarrow T_c = \sqrt{6}\eta. \tag{2.17}$$

The shape of the potential at $T = T_c$ is indicated in Figure 2.4. One can see that the potential at this temperature has almost completely reverted to a parabola with only a single minimum at $\phi = 0$.

This specific example illustrates a concept known as a second order phase transition. The difference between a first and second order phase transition lies in whether the field can transform continuously. In our current example, the field ϕ can gradually take on lower and lower minima, one can imagine the red circle in Figure 2.4 as a ball gradually falling to the right as the potential is lowered. A first order phase transition does not allow for this gradual behaviour. At very high temperatures $T > T_c$ the system also relaxes to one minimum, but as the temperature increases, somewhere else in the potential a deeper minimum forms, separated from the original minimum by a barrier. Hence without quantum tunneling or an influx of energy, the system cannot cross this barrier to achieve the true minimum energy configuration. Going back to the analogy of the ball: the ball is happy to stay where it was put at high temperature, unaware that somewhere over the ridge lies a deeper valley.

Now, all that is left is to connect these concepts to the formation of topological defects. Second order phase transitions can form topological defects by way of the Kibble mechanism [19]. As the temperature crosses the critical temperature $T < T_c$, the system will have to pick a minimum.

In the case of the example just discussed, the ball needs to pick a direction to fall. This choice is motivated by quantum fluctuations. An important caveat here is the scale. Locally, the system will try to minimize its energy by taking on a homogeneous field configuration i.e. once a minimum is chosen, the system will locally want to relax to that minimum. On a global scale this is not possible. Points in space outside of each others' causal horizon cannot possibly communicate the choice of minima and hence domains of minima on the scale of the causal horizon will form.

Since the ball metaphor is probably tiresome at this point, consider a row of people going around the circumference of the Earth from north to south pole. At the north pole one person decides to pick a positive minimum. He shouts this out and all people close enough to hear him make the same choice. After hearing the choice, they too shout out and the signal is able to travel along the Earth. On the south pole however, someone decided that a negative minimum suited them better. They too begin shouting out this choice. People around the south pole hear and continue perpetrating the negative minimum. Now consider what happens to the person standing on the equator. When the signal reaches him, there are people shouting negative in his left ear and positive in his right ear. Unable to decide the person makes a compromise and chooses 0. A domain wall has just formed, interpolating between two different regions of minima.

There are more situations possible in which other topological defects e.g. strings or textures can form. This thesis will forego that discussion, but the reader is invited to consult [11] for a more extensive review. The correlation length ξ is the typical distance between uncorrelated domains of minima. Its upper bound is the causal horizon as discussed before, but the exact expression depends on the physics of the second order phase transition.

This section set out to introduce the reader to topological defects. In particular, their topological nature and connection to second order phase transitions in the early Universe. It introduced topological defects by ways of a simple example. After this the mathematical structure in the form of homotopy theory was explored. A description of symmetry breaking in phase transitions was provided. The Section ended with a discussion on how this symmetry breaking could lead to the formation of topological defects by ways of the Kibble mechanism.

2.2 Gravitational waves

As the later part of the thesis aims to provide a prediction on the Gravitational Wave (GW) signal stemming from domain walls in the early Universe, this theoretical introduction also includes an overview of gravitational wave physics.

Gravitional waves pop up in literature as early as 1905, when Henry Poincaré postulated that gravity, in a similar way to electromagnetism, was carried by waves [20]. After Einstein introduced his General theory of Relativity (GR), the concept of gravitational waves was finetuned to what they are today: propagating ripples in spacetime, changing distances wherever they pass. As these effects are tiny, in the order of 10^{-21} percent spatial variation, their discoveries were remarkable.

Both indirect and direct observations mark a key point in the history of physics and were rewarded with a Nobel prize. The first indirect observation was made by Hulse and Taylor in 1974 [21]. In it, the discoverers observed the orbit of a binary star system, comprised of two neutron stars, one of which is a pulsar. Since a pulsar continuously emits electromagnetic radiation out of its poles, they can be used to measure the orbit of systems in which they are contained if their poles line up with earth in their rotation. Hulse and Taylor found the orbit to be decaying in exactly the way it was expected when energy was carried away from the system by gravitational waves. A direct observation was only achieved much later, in 2015 the LIGO collaboration measured the spatial variation in two interferometers specifically build to search for gravitational waves [1].

To mathematically calculate a GW signal from the Einstein equation, a linearisation of GR, often also called a weak field limit, is employed. It consists of viewing the general metric of spacetime $g_{\mu\nu}$ as a flat Minkowksi metric $\eta_{\mu\nu}$ enhanced by small perturbations $h_{\mu\nu}$:

$$g_{\mu\nu} = \eta_{\mu\nu} + h_{\mu\nu}, \tag{2.18}$$

in which $\eta_{\mu\nu}$ is the Minkowski metric given by

$$\eta_{\mu\nu} = (-1, +1, +1, +1). \tag{2.19}$$

Plugging this linearised version of the metric into the Einstein equations yields

$$\Box \bar{h}_{\mu\nu} = -\frac{16\pi G}{c^4} T_{\mu\nu}, \tag{2.20}$$

in which $\bar{h}_{\mu\nu}$ is the traceless part of the perturbation tensor

$$\bar{h}_{\mu\nu} = h_{\mu\nu} - \frac{1}{2} h^{\rho}{}_{\rho} \eta_{\mu\nu}. \tag{2.21}$$

Note that in these equations the de Donder gauge $\partial^{\nu} \bar{h}_{\mu\nu} = 0$ is chosen to simplify the equations.

Equation 2.20 can be interpreted as a wave equation for each component of $\bar{h}_{\mu\nu}$. The right hand side contains the energy-momentum $T_{\mu\nu}$ tensor as a source term. Matter acts as an "engine" for waves in spacetime, traveling at the speed of light.

To illustrate the effect of GW's on distance, observe a wave traveling in the z-direction act on two particles at coordinates $(0, 0, 0)$ and $(L, 0, 0)$. The proper distance can be calculated [22] ans is given by

$$\Delta s = \int_0^L dx \sqrt{1 + h_{11}^{TT}} \tag{2.22}$$

$$\approx L(1 + \frac{1}{2} h_{11}^{TT}). \tag{2.23}$$

This allows for defining a quantity $\frac{\delta L}{L}$, called the strain of the gravitational wave. This is what is measured in interferometer detectors like LIGO [23]. The strain is connected to the gravitational wave as

$$\frac{\delta L}{L} \approx \frac{1}{2} h_{11}^{TT}. \tag{2.24}$$

Solving the wave equation can be done by employing retarded Green's functions in an environment of sufficiently reasonable assumptions. Since GW detectors on Earth

are (luckily) far away from any event strong enough to generate detectable gravitational waves, the distance between source and detector r can be safely send to infinity $r \to \infty$. The gauge freedom remaining after imposing the de Donder gauge is used to put $\bar{h}_{\mu\nu}$ in the simple form of a transverse traceless matrix with only nonzero spatial indices, denoted as h_{ij}^{TT}, where $\{i, j\}$ denote spatial indices *.

The calculation of this tensor and its emitted power P is a straightforward albeit long procedure. To keep this chapter focused, we will not elaborate further on this calculation and state the important results. For the interested reader, the complete derivation can be found in [22].

Assuming that the matter sourcing the GWs moves at a velocity much slower than the speed of light, the GW tensor and its power can be written to lowest order as the quadrupole moment I_{ij} of the source. For a wave traveling along the z-axis, the power carried can be written as

$$P = \frac{G}{5c^5} \langle \dddot{Q}_{ij} \dddot{Q}_{ij} \rangle, \tag{2.25}$$

in which Q_{ij} denotes the traceless quadrupole moment $Q_{ij} = I_{ij} - \frac{1}{3}\delta_{ij} I^i_{\ i}$ of the mass generating the gravitational wave. These are the lowest order contributions to the multipole expansion of the power. The dipole moments must be 0 when demanding the conservation of angular momentum. The quadrupole moment is defined as

$$I_{ij} = \int d^3x T_{00}(t, \vec{x}) x_i x_j. \tag{2.26}$$

2.2.1 The Stochastic Gravitational Wave Background (SGWB)

A plethora of phenomena is capable of generating gravitational waves. While a subgroup of these can be localised on the celestial plane, the sum of those too weak to detect directly or those with no resolvable location, gives rise to a uniform and, to first order, isotropic background. This background is called the Stochastic Gravitational Wave Background (SGWB). We will elaborate on the contributions to this background and the way in which its signal is parameterised. This discussion will cover the basic ideas. For an extensive and detailed overview, the interested reader is encouraged to consult [24].

The SGWB is the superposition of gravitational wave signals from a large number of independent and unresolvable sources. These sources can be either astrophysical or cosmological in origin. Cosmological sources at early times cannot emit gravitational wave signals correlated at lengths beyond the causal horizon (at the time of emission),

*Which is equal to $\bar{h}_{ij}^{TT}$, since the only difference is the trace part.

often taken as the inverse Hubble parameter $H^{-1}(t_{em})$ [25]. Our redshifted field of view today includes many of these early time Hubble volumes. Every one of these volumes contains sources that emit uncorrelated gravitational waves. The result is a superposition of uncorrelated GW signals. One can compute the number of Hubble volumes visible today, given a time of emission. As an example, gravitational wave signals emitted at the electroweak phase transition $T \sim 100$ GeV could be emitted from $\sim 10^{24}$ Hubble volumes. This is the reason for the statistical nature of the SGWB. To avoid the statistics, a detector would have to be able to resolve all these 10^{24} volumes.

Due to the superposition and interference of all these independent signals, the measured signal will average out to 0. To observe a signal one has to look at the correlation functions $\langle h(t), h(t')\rangle$, in which $h(t)$ denotes the GW signal. These correlation functions can be calculated by expanding the GW tensor h_{ij} into its Fourier modes and assuming a homogeneous and isotropic and Gaussian background. These calculations were performed in [25] and yield a link between these correlation functions and the energy density of the gravitational wave signal. We can now link the energy density of a gravitational wave with detections made by experiments.

The signal observed by a detector in function of time $s(t)$ can be decomposed in two contributions as [22]

$$s(t) = h(t) + n(t), \tag{2.27}$$

in which $h(t)$ represents the gravitational wave signal and $n(t)$ the noise measured in the detector. The correlation between independent measurements of two detectors would yield $\langle s, s\rangle$. Since the noise function of two sufficiently separated detectors is uncorrelated $\langle n, n\rangle = 0$, as well as the gravitational wave signal and the noise $\langle h, n\rangle = 0$, the correlation between detectors yields

$$\langle s, s\rangle = \langle h, h\rangle, \tag{2.28}$$

which can be linked to the gravitational wave energy density, as outlined in [25].

This is very similar to the Cosmological Microwave Background (CMB) in that we have to measure a signal in terms of statistical correlation functions. This stochastic background cannot be directly detected by a single detector. It appears there as random noise. Only by combining several detectors and cross-correlating the detector outputs, could this background be mapped, since the systematic noise for locations sufficiently separated can be seen as statistically independent.

The SGWB is generally described in terms of the detected energy density per logarithmic frequency interval, weighed by the critical energy density of the Universe. This definition can be written down as [24]

$$\Omega_{GW}(f) \coloneqq \frac{1}{\rho_c}\frac{d\rho_{GW}}{d\ln f}, \tag{2.29}$$

in which the critical density is $\rho_c = \frac{3c^2H_0^2}{8\pi G} \approx 7.6\times10^{-9}\text{erg/cm}^3$ [24] and $H_0 = 67.74\frac{\text{km}}{\text{s}}/\text{Mpc}$ [26].

The challenge of finding this background is a current ongoing field of research and one that could influence several theories of cosmology and astrophysics. The background can provide a snapshot of the Universe even before recombination and the emission of the CMB, since first order phase transitions and topological defects happening before the CMB epoch can contribute to the signal. A short overview of the different components will be given after which the current constraints on the SGWB signal will be illustrated.

The components of the SGWB can be divided into two categories: cosmological and astrophysical contributions. Cosmological components refer to GW producing phenomena in the early Universe like inflation or phase transitions. Astrophysical components are the sums of mergers of black holes and neutron stars, supernovae, inhomogeneous pulsars and more over the whole history of the Universe. The detection of single Binary Black Hole mergers (BBH) and Binary Neutron Star mergers (BNS) was already accomplished by the LIGO-Virgo scientific collaboration [1, 27]. While the SGWB consists of several interesting GW producing mechanisms, this thesis will focus on those of immediate interest, both to conserve brevity and clarity.

The theory of inflation was proposed to solve both the horizon and flatness problem in cosmology. The homogeinity of the CMB suggests that at some point in the past, the part of the Universe visible in the CMB was in causal contact. A constant expansion of the Universe does not allow the particle horizons of the CMB to intersect at recombination, leading to the horizon problem [28].

The flatness problem is more of a fine-tuning problem. Current observations place the energy density of the Universe very close to the critical density $\rho \sim \rho_c$, the density for which the Universe would assume a flat configuration. Any deviation from the value ρ_c in the early Universe would grow exponentially, since the configuration $\rho = \rho_c$ does not define a stable Universe for matter or radiation dominated era [29]. The conclusion is that the early Universe must have been fine-tuned to be very close to critical density. The why and how are solved by an era dominated by a field ϕ, called the inflaton field, which behaves as a perfect fluid with equation of state: $P = w\rho$, with pressure P and constant $w < -\frac{1}{3}$, again leading to an era of exponential behaviour. Tensorial perturbations in the metric during inflation, give rise to gravitational waves [30]. Observing these waves in the SGWB would yield information on inflationary models.

Phase transitions in the early Universe are an integral part of the Standard Model (SM) and several Beyond the Standard Model (BSM) theories. Think for example of the breaking of the electroweak symmetry. The electroweak phase transition is neither a first nor second order phase transition, but could be first order in models slightly differing from the SM [31].

Grand Unified Theories suggest that the current symmetry groups of the standard model were once part of a larger symmetry group G. This automatically implies a

phase transition from the original group to the strong symmetry $SU(3)$ and electroweak symmetry group $SU(2) \times U(1)$: $G \to SU(3) \times SU(2) \times U(1)$ [32].

In first order phase transitions, expanding bubbles of the new phase form and expand. While the expansion of symmetric bubbles does not produce gravitational waves, the collision of two bubbles and the fluid dynamics of the plasma do [33]. This source is of particular interest, since the electroweak phase transition would produce GW's visible in the spectrum of the Laser Interferometer Space Antenna (LISA), set to launch in 2037 [34, 35].

While not all types of phase transitions give rise to bubbles, they all produce topological defects like strings, domain walls, branes, etc. as already discussed in 2.1. All of these effects also contribute to the SGWB signal.

The astrophysical SGWB is even closer to a potential discovery. The LIGO-Virgo collaboration's future upgrades would be sensitive to the proposed BBH and BNS background spectrum once the full design sensitivity is achieved [36–38]. These backgrounds contain all BBH or BNS signals too weak to directly detect. Their signals combine into a noise background with a spectrum that is illustrated in Figure 2.5. The sensitivity of advanced Virgo is also illustrated to demonstrate which part of the BBH and BNS spectrum is measurable. This Figure also includes future detectors LISA [39] and the Einstein Telescope (ET) [40]. Both of these sensitivity cures also overlap the BBH and BNS spectra. The calculation of sensitivity curves can be checked in [41]. Appendix A.1 aims to illustrate the general procedure of finding the sensitivity curves shown in Figure 2.5

The remainder of the figure consists of limits placed on the stochastic background.The pulsar limit, for example, can be seen in the NANOGrav sensitivity curve [42]. Pulsars are rotating neutron stars with a strong magnetic field, aligned along an axis that not necessarily coincides with the axis of rotation. They emit a beam of electromagnetic radiation along their magnetic axis, which can be observed on Earth if the pulsar's axis aligns correctly with Earth. Since pulsars have a very steady frequency, the arrival time of the pulses of radiation can be used as an astronomical clock. When a gravitational wave passes Earth or the pulsar, it varies the spacetime and changes the measured pulsar frequency and leads to the observation of an anomaly in the pulse arrival times. NANOGrav is a detector utilising this principle in the radio frequency range to impose limits on the SGWB .

The CMB limit can be imposed by observing that gravitational waves in the excluded region would have left their mark on the CMB, either as quadrupole anisotropies, due to GWs today with a wavelengths similar to the Hubble scale, or small angular fluctuations due to GW's at recombinations [45]. The CMB curve shown in Figure 2.5 was constructed with data from the Planck satellite [43].

The limits illustrated in the indirect limit curve are due to current Deuterium,

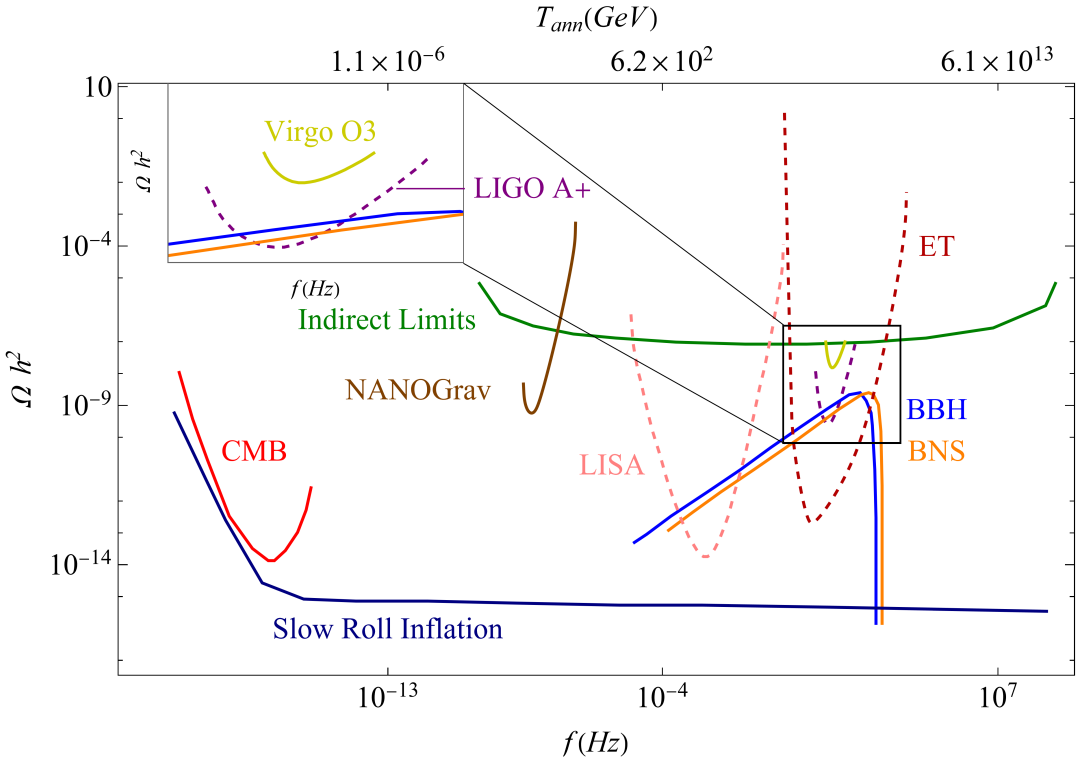

Figure 2.5: Plot of the sensitivity curves of experiments looking at the SGWB. Dashed lines indicate future experiments. The predicted power spectra of the BBH and BNS contributions to the SGWB are drawn to illustrate what experiments would be sensitive to their signal. One can see that both LISA [39] and ET [40] predict a measurement. Advanced LIGO+'s output would also intersect with the BBH and BNS signals [38]. The current sensitivity curve of the third Virgo run is drawn in yellow [24]. Pulsar timing array (PTA) measurements from the radio detector NANOGrav impose an upper limit on the SGWB signal [42] Other limits based on CMB observations [43] and inflation [44] The Figure was based on [24]

Lithium and Helium abundancy observations. Gravitational waves in the early Universe that do not agree with this limit would have increased the overall energy density, speeding up the expansion of the Universe and decreasing the rate at which particles could have interacted to form nuclei, hence influencing the abundances observed today [46]. The limits shown in Figure 2.5 were calculated in [47]

This concludes the discussion on gravitational waves. Their general definition was explained, along with the formulas that are of import to the thesis. To conserve brevity their calculations were omitted, but they can be consulted in [22]. After this introduction, the stochastic gravitational wave background (SGWB) was introduced as the combined signal of all sources to weak to be detected singularly or that are unresolvable.

Several components of the SGWB were explained, together with the limits imposed by current experiments.

The chapter ended with a figure that illustrates current and future experiment sensitivities to the SGWB. As an example two sources of the astrophysical SGWB were indicated. The binary black hole (BBH) and binare neutron star (BNS) power spectra would be visible to future experiments like ET [40] or LISA [39] or upgrades to current experiments like the Hanford-LIGO-Virgo collaboration [38].

Now that both topological defects and gravitational waves were introduced, we are ready to discuss the final theoretical field employed in this thesis. The last chapter will discuss superconductivity and how the phenomenon will be treated in the thesis.

2.3 Superconductivity

As final part of this introductory chapter, the notion of superconductivity will be explained. The focus will lay on the field theory aspect. The criteria by which superconductivity is defined in this thesis will be explained for use in later chapters, where the proof of superconductivity of strings and domain walls will be discussed.

As its name suggests, a superconductor exhibits zero resistivity below a certain critical temperature T_c. This implies that a superconducting wire, bend in a loop is able to carry a current indefinitely. No power source is needed to keep the current alive in the loop. A superconductor also expels any magnetic field lines outwards, making sure that no field lines can be drawn inside of the superconductor. This phenomenon is known as the Meissner effect. Finally a superconductor exhibits a charging effect in the form $dj/dt \sim E$, in which the electric current j is increased when applying an external electric field E. This thesis will utilise these criteria as the defining features of a superconductor. The proof that certain topological effects are superconducting will be given in terms of proving the previously discussed criteria.

To explain this behaviour, a quantum formalism is necessary. Several theories, ranging from phenomological to theoretical exist. These including London [48], Ginzburg-Landau [49] and Bardeen-Cooper-Schrieffer (BCS) [50] theory. This section will attempt to explain superconductivity in a field theoretical way, as this formalism will be applied in later chapters. For an extensive overview of superconducting theories and the history of this intriguing phenomenon, see [51–53].

Note that the concept of a superconductor entails many different classes, ranging form type I and II superconductors to high temperature superconductors. this thesis is only interested in the simplest of superconductors: type I low temperature superconductors.

Now that the reader has a general idea of what superconductivity entails and the leading theories that determine its behaviour, we can now move on to explaining the

formalism used in this thesis. This is the field theory formalism, which builds the properties of a superconductor by breaking a $U(1)$ symmetry inside the superconductor.

2.3.1 Field theory of superconductivity

This Section is based on calculations made in [54]. The field theoretical approach defines a Lagrangian which is invariant under a $U(1)$ symmetry. A potential is attached, constructed such that the field breaks the $U(1)$ symmetry inside the superconductor. It will be shown that by breaking the symmetry, one can explain the Meissner effect. In Chapters 4 and 6 the same formalism is used to show the existence of a persistent current and a charging mechanism. We demonstrate the formalism and the existence of the Meissner effect as an illustrative example.

This model is defined by a Lagrangian written as

$$\mathcal{L} = D_\mu \phi (D^\mu \phi)^* - V(|\phi|) - \frac{1}{4} F_{\mu\nu} F^{\mu\nu}, \tag{2.30}$$

with a potential

$$V(|\phi|) = \lambda(\phi\phi^* - \eta^2)^2. \tag{2.31}$$

ϕ is a complex scalar field and the covariant derivative is defined as $D_\mu \phi = \partial_\mu \phi + ieA_\mu$. Note that this definition differs from the one given in [54]. It was changed to be consistent in notation with the rest of this thesis. The results remain the same.

A_μ is the gauge field and can be interpreted as a photon. This Lagrangian is invariant under the $U(1)$ gauge symmetry. The potential is the Mexican hat potential of the Higgs mechanism and hence the field ϕ will assume a nonzero *vev*. ϕ in its groundstate can be parametrized as $\phi = \eta e^{i\theta}$. Solving the equations of motion for the electromagnetic four vector, assuming a static field $\phi = \eta$ yields

$$\partial_\mu F^{\mu\nu} + 2e^2\eta^2 A^\nu = 0. \tag{2.32}$$

The spatial components of this equation can be rewritten in terms of the field $\vec{B}$. This calculation will be omitted here, but will be performed when proving the Meissner effect in Chapters 4 and 6. The result is

$$\nabla^2 \vec{B} = 2e^2\eta^2 \vec{B}, \tag{2.33}$$

which indeed implies that any magnetic field $\vec{B}$ entering a region where ϕ takes on its *vev* will die out exponentially.

In this case the field ϕ was assumed to take on its *vev* η everywhere, without a change in phase or amplitude. For real applications the field ϕ is dynamic and should

be deconstructed into an amplitude and phase, both of which are determined by its equations of motion. When doing this complete calculation it turns out that not all superconductors nicely expel their magnetic fields. Situations are possible in which vortices form, places on the superconductor in which ϕ takes a value of zero [54]. These are called Type II superconductors and will be omitted for simplicity. We only mention them for completeness.

The breaking of the $U(1)$ gauge symmetry can be interpreted as the photons obtaining a mass in a superconductor. The photon mass gives rise to superconductivity by making it harder for the current inside the superconductor to lose energy by ways of photon production. Without a way to emit energy in the form of photons, the current does not dissipate and the resistivity drops to zero.

The concept of superconductivity will be made more clear when actually applying the concept to topological defects. The purpose of this theoretical introduction was to give a taste of what superconductivity means. More complicated cases of superconductivity, such as Type II superconductors or high energy superconductors fall outside of the scope of this thesis, but could make interesting topics for further application to topological defects.

3 Cosmic strings

The ultimate goal of this thesis is the consideration of superconducting domain walls similar to how E. Witten extended the concept of a cosmic string to a superconducting cosmic string in his 1985 paper [7]. To reach this goal the steps of Witten will first be reproduced. A natural starting point is a discussion on normal cosmic strings. Their field configuration and properties will be discussed, where the computation of the field profiles constitutes an independent derivation of existing results. Along with this introduction on cosmic strings, the general methodology used in the rest of the thesis will be explained. At the end of this chapter the reader should be familiar with cosmic strings and be able to follow the methods on which the following chapters are built.

3.1 String configuration

The introductory chapter on topological defects focused mainly on the domain wall example, which arose due to a discrete Z_2 symmetry being broken in a phase transition. The mathematical basis for this occurring is the vacuum manifold $\mathcal{M}$ exhibiting a non trivial 0'th homotopy group $\pi_0(\mathcal{M}) \neq 1$. A different structure of the vacuum manifold allows for different topological defects to form.

Consider the 1'st homotopy group $\pi_1(\mathcal{M})$. This group contains all equivalent classes of $1-$spheres which can be continuously deformed in one another. In other words if $\pi_1(\mathcal{M})$ is trivial, all $1-$spheres i.e. circles drawn on the manifold can be shrunk/stretched in a continuous way to form any other circle on the manifold. The non-triviality hence indicates parts of the manifold which do not allow for a circle to simply be stretched or moved across it.

To illustrate this observe Figure 3.1. If the circles A, B and F can be transformed in each other, they will be equivalent in the homotopy group and constitute only one element. Circle B can be moved to the location of F and subsequently be stretched to match. Hence, B and F are equivalent. Circle A, however, cannot move such that it no longer includes the hole in the manifold. The only way for A to move and stretch into F is to discontinuously "jump" over the hole. Hence this sketch of the vacuum manifold exhibits a non trivial first homotopy group $\pi_1(\mathcal{M}) \neq 1$.

3.1.1 Global strings

When the field values throughout space follow this loop around such a hole, cosmic strings can arise. A Mexican hat potential as one is familiar with in the Brout Englert Higgs mechanism indeed contains such a loop. Just like the domain wall example consisted of breaking a Z_2 symmetry, one can build models in which the breaking of a $\tilde{U}(1)$ symmetry leads to strings.

Note that we will use the notation $\tilde{U}(1)$ for the symmetry on the field "constructing" the string (in this case ϕ) to avoid confusion when discussing the superconducting string,

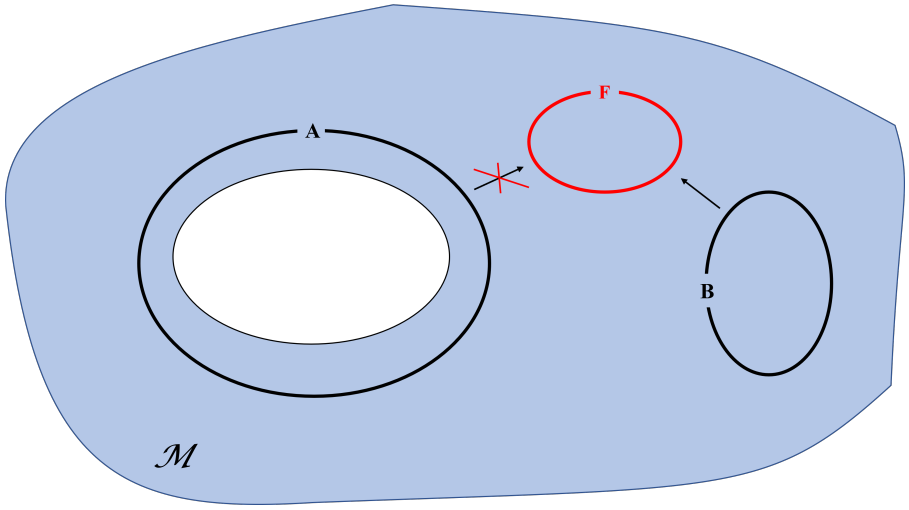

Figure 3.1: Sketch of the vacuum manifold $\mathcal{M}$ with different projections of S^1 drawn on its surface. The manifold exhibits a hole in its centre, making it impossible for circles drawn around this hole to continuously transform into circles not including the hole.

which contains two fields, each with such a symmetry.

For now, the thesis will focus on one field and one $\tilde{U}(1)$ symmetry. As a starting point the global $\tilde{U}(1)$ symmetry case will be considered. Although this case requires a caveat, it is a good example to introduce the concept and calculations of the profile. The subtleties to be considered will be discussed at the end of the global string formalism.

The Lagrangian to be considered will look familiar. It is again the ϕ^4 Lagrangian, but this time a complex scalar field ϕ is considered.

$$\mathcal{L} = \partial_\mu \phi \partial^\mu \phi^* - V(\phi), \tag{3.1}$$

with a Mexican Hat potential

$$V(\phi) = \frac{1}{4}\lambda(|\phi|^2 - \eta^2)^2, \tag{3.2}$$

the shape of which is shown in Figure 3.2.

The idea of a string can be physically explained by observing the minima of this potential. These minima, which satisfy $|\phi| = \eta$ can be parameterized as $\eta e^{i\theta}$. These are the lowest energy configurations and the field's *vev* will take values along the circle. Unlike the case of the domain walls, the vacuum is not simply a discrete choice, a whole continuous space $\theta \in [0, 2\pi[$ is available.

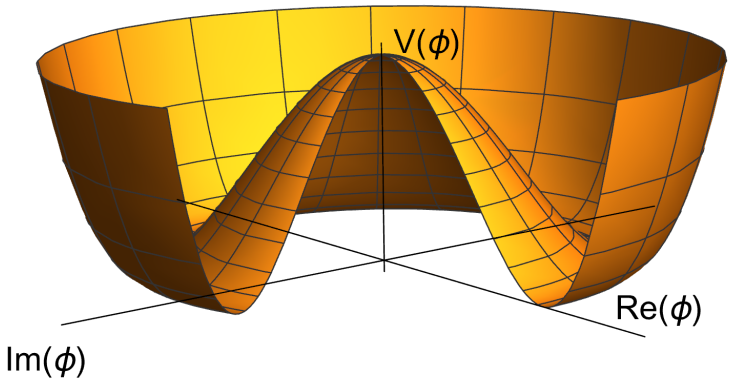

Figure 3.2: A sketch of the Mexican hat potential. The valley of minima corresponds to $|\phi| = \eta$.

Imagine a loop in physical space, a scenario is plausible in which the field runs through its phase n times before returning to the same point. Let the loop be defined by a parameter l. As the parameter l runs through the circumference, $\Delta l = 2\pi R$ with $R \in \mathbb{R}_0^+$; the phase θ runs from 0 to $2n\pi$ with $n \in \mathbb{Z}$, since the field value in a point on the loop should satisfy $\phi(l) = \phi(l + 2\pi R)$, one can state that the phase should return to its original value modulo 2π after traversing the loop once. Hence after one circumference the phase will be $\theta = 2\pi n$. n in this context is called the winding number. This behaviour is visualised in Figure 3.3.

Since the system maintains a continuous field configuration, defining a surface spanned by the original loop allows for defining a new loop on that surface, where the phase θ also runs through its values n times. By repeating this process, one comes to a point in which the loop is reduced to a point. A phase difference is undefined at this point and the field has no choice but to jump to the top of the Mexican hat potential at $\phi = 0$.

By repeating this process one can find for each surface bounded by the loop an intersection with the vortex, called the string core. These string cores connect linearly to form a $1+1$ dimensional topological defect: a string. Note that the field profile does not simply jump from its minimum to the top of the Mexican Hat, as this this would infer a discontinuous behaviour. Instead, the profile continuously runs around higher and higher loops on the Mexican Hat as we look closer to the string core. This behaviour is illustrated in Figure 3.4.

This process of rising on the potential indicates that the field profile of a cosmic string is a non-trivial shape. Numerics are needed to solve the equations of motion close to the string core. This thesis developed a numerical code to solve these equations of motion based on a relaxation algorithm. In the following, this will be applied to

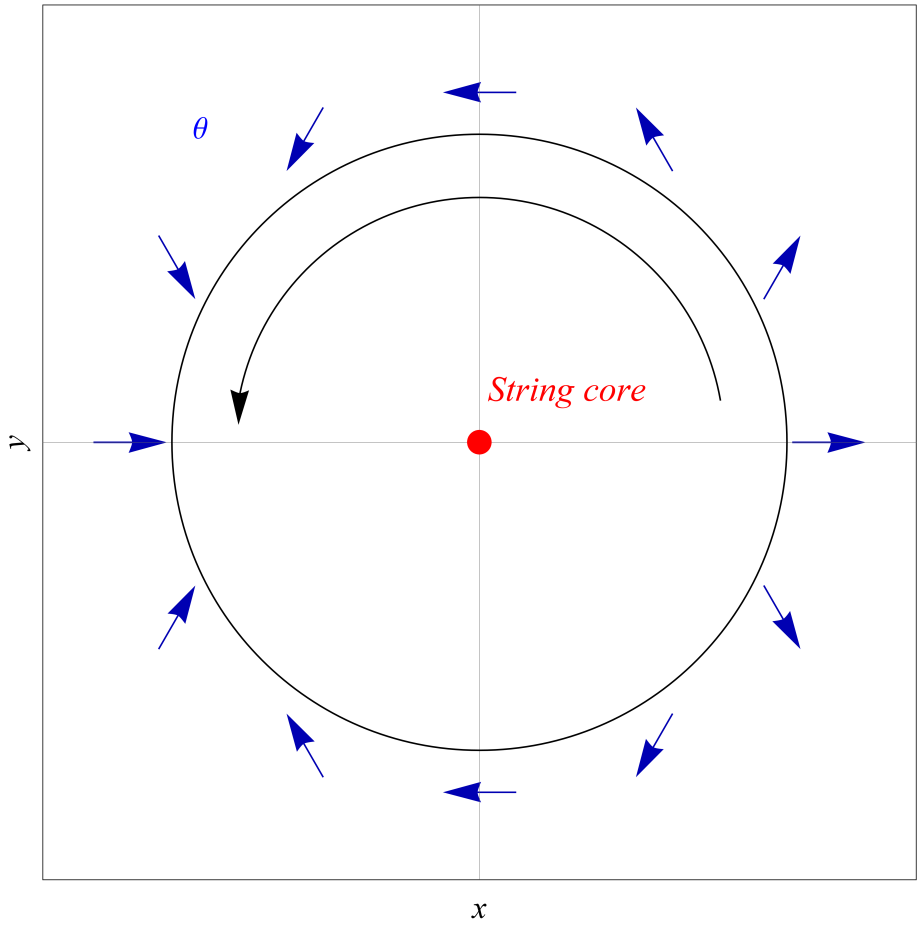

Figure 3.3: The field profile running through its phase $n = 2$ times whilst traversing a loop in physical space once. The loop was chosen sufficiently far away from the string core such that the field can take on its *vev* $\phi = \eta e^{i\theta}$. The phase of the field is denoted by blue arrows. The top arrow for example indicates that the field has a phase $\theta = -\pi$. The black arrow denotes in which direction one traverses the loop in physical space. It can be noted in this figure that the blue arrows rotate around themselves twice, hence the phase changes from 0 to 4π due to the winding number $n = 2$.

calculate the field profile of the cosmic string. Later in the thesis, the numerical code will be expanded to incorporate a superconductive regime and solve both normal and superconductive domain walls. The details of the numerical scheme can be consulted in Appendix B.1. We will now apply the scheme by calculating the equations of motion of the field ϕ and computing a solution numerically.

The equation of motion for the global string Lagrangian in Equation (3.1) is calculated to be

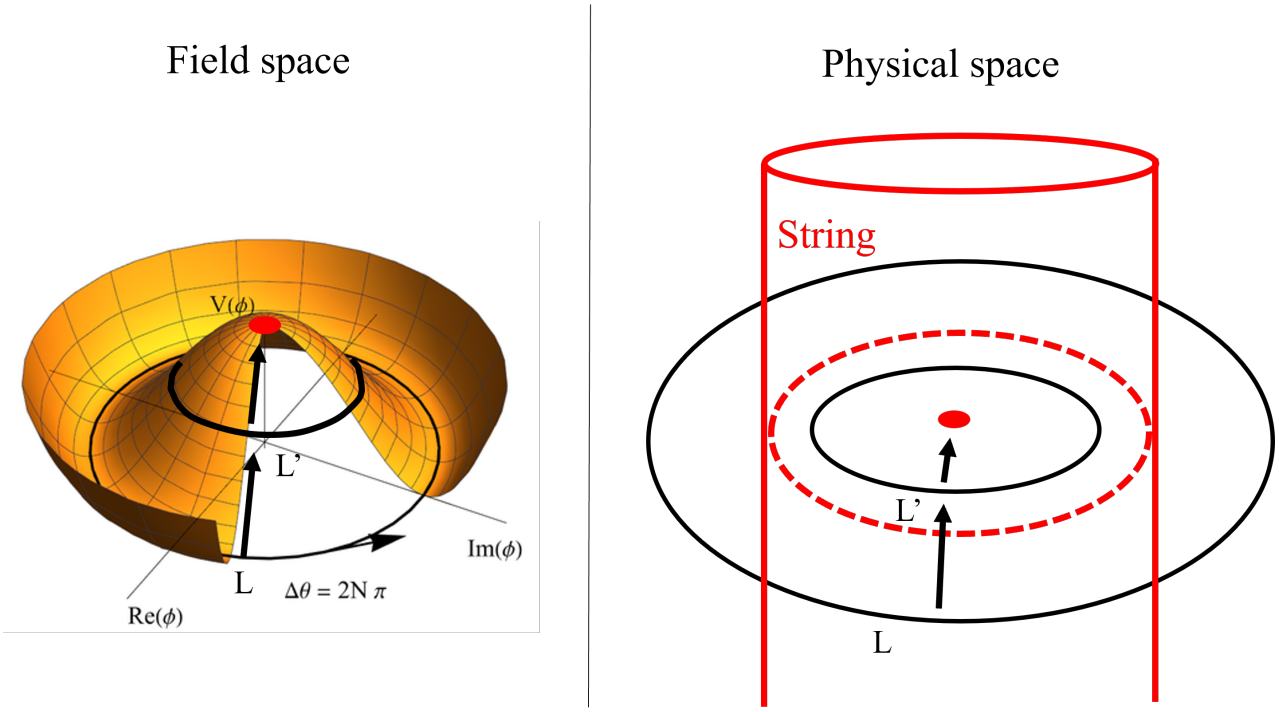

Figure 3.4: The behaviour of the field on the Mexican hat for loops closer and closer to the string core. For a loop L outside the string in physical space, the field lives in the valley of true vacua. A loop L' inside the string forces the field to take on values which correspond with potential values higher on the Mexican hat hill. At the string core, denoted by a red disc, the field is forced to take on the value $\phi = 0$ and rests atop the potential hill. **Left** The Mexican hat potential is shown. The black loops indicate on which part of the potential the field lives when traversing a loop in physical space. **Right** The string is denoted as a red cylinder. While one traverses the loops L and L' in physical space, the field takes on values denoted on the left hand side.

$$\partial_\mu \partial^\mu \phi + \frac{\lambda}{2}(|\phi|^2 - \eta^2)\phi = 0. \tag{3.3}$$

Inspired by the behaviour of the field across the vacuum valley, one can make an ansatz on a plane perpendicular to the string by assuming cylindrical symmetry. If the string is placed along the $z-$axis, the perpendicular plane is the $xy-$plane. The only parameters in physical space are the distance to the core r and the angle θ on the plane [55, 56].

$$\phi = f(r)e^{in\theta}. \tag{3.4}$$

n parameterises the times the field runs through its phase as it runs around a loop in physical space. It is hence the winding number mentioned before.

For a loop sufficiently far away from the core, this parameterization should satisfy the condition $|\phi| = \eta$ as the field will relax to its true vacuum state. At the exact center of the core, the field sit atop the Mexican Hat potential at $\phi = 0$. This yields the boundary conditions

$$f(r) = \eta \quad \text{for } r \to \infty, \tag{3.5}$$
$$f(0) = 0. \tag{3.6}$$

Substituting this ansatz into the equations of motion yields a differential equation on which our numerical analysis can be applied for the first time. This analysis will be applied several times over the course of the thesis to determine the field profiles of (superconducting) strings and domain walls.

The global string case is a simple example to check whether the numerics yield reasonable results. Reasonable meaning that the results fall in the naturally expected range of the variables. The differential equation

$$\frac{d^2 f}{dr^2} + \frac{1}{r}\frac{df}{dr} - \frac{n^2}{r^2} f - \frac{\lambda}{2}(f^2 - \eta^2) f = 0 \tag{3.7}$$

can be transformed into dimensionless quantities $F = f(r)/\eta$ and $R = \eta\, r$. This sets the *vev* in the differential equation to 1 and allows for checking the shape of the profile independently of choosing a value for η. The differential equation takes the form

$$\frac{d^2 F}{dR^2} + \frac{1}{R}\frac{dF}{dR} - \frac{n^2}{R^2} F - \frac{\lambda}{2}(F^2 - 1) F = 0. \tag{3.8}$$

The numerical solution found in this thesis is illustrated in Figure 3.5. We see that very far from the string core $r \to \infty$, the field tends to the true vacuum $F = 1$. Close to the string core $r = 0$ the field sits atop the Mexican hat potential $F = 0$. The string can be approximately identified with the region around the string core where the field is significantly different from its vacuum value. This region is shaded in Figure 3.5.

We can conclude that the numerical algorithm does indeed yield acceptable results with respect to the global string example. Comparing the shape of the field profile with plots from, for example, [11] indicates that the algorithm can be deemed ready to be applied to more complex cases like the local string configuration in the next Section.

To conclude the global string case, a few remarks are in order. The global string's energy density is divergent. To investigate this, one can estimate the width and energy density inside the core of the string. The width of the string is determined by the field ϕ getting excited from its vacuum ground state. With this in mind the width can be approximated by interpreting the mass term of the ϕ field as its inverse Compton wavelength. Hence the width equals

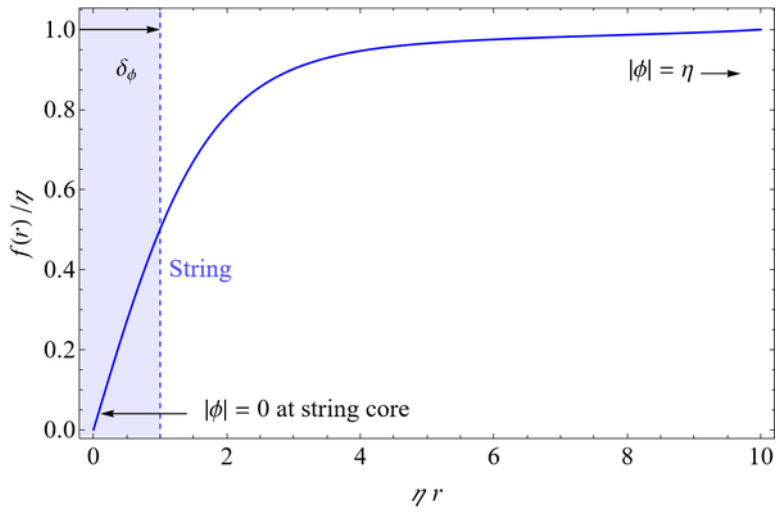

Figure 3.5: Numerical solution to Equation 3.7 for a winding number $n = 1$ and parameter $\lambda = 2$. The string core is defined by the width δ_ϕ and is indicated with a dashed blue line. The field profile tends to 0 when approaching the string core. This corresponds with the system assuming the local maximum of the Mexican hat potential hill. Far away from the string, the field tends to the true vacuum $f(r \to +\infty) \to \eta$. This corresponds with the system assuming values in the Mexican hat vacuum valley.

$$\delta_\phi \sim \frac{1}{m_\phi} \sim \sqrt{\frac{2}{\lambda}}\eta^{-1}. \tag{3.9}$$

The energy density ρ_0 at the center $\phi = 0$ can be approximated as the value of the potential hill of the Mexican Hat. This yields an approximate value

$$\rho_0 \sim V(0) \sim \lambda\eta^4. \tag{3.10}$$

Combining Equations (3.9) and (3.10) yields an expression for the energy per unit length of the string. It can be approximated as

$$\mu \sim \rho_0\delta_\phi^2 \sim \eta^2. \tag{3.11}$$

Here the volume energy density was multiplied by the area defined by the intersection of the string and the plane perpendicular to the string direction. The energy per unit length can be utilised when approximating the string as a $1+1$ dimensional object e.g. when looking at properties in the far field limit.

The approximation in Equation (3.11) does however neglect the behaviour of the phase θ outside of the string core. When the field ϕ takes on its vev $\phi = \eta$, the derivative of the phase appears in the Lagrangian (3.1) with an effective mass as

$$\mathcal{L}_\theta = \eta^2 \partial_\mu \theta \partial^\mu \theta. \tag{3.12}$$

In fact every configuration in which the field is nonzero $|\phi| \neq 0$ contributes in this way. The energy outside of the string is enhanced by the phase looping around the string, since this yields a nonzero derivative of the phase. The global string does not contain a mechanism to offset this contribution an hence the energy per unit length diverges [11].

One could interpret this as the kinetic energy of the field blowing up due to the field trying to rotate its phase everywhere in the space outside of the string. This can be checked by calculating the energy per unit length exactly. Taking the energy momentum tensor and integrating over the plane perpendicular to the string yields an expression

$$\mu \sim \eta^2 + 2\pi \int_{\delta_\phi}^{R} dr\, r \left(\frac{1}{r} \frac{\partial \phi}{\partial \theta} \right)^2. \tag{3.13}$$

One can see that the energy per unit length obtains an unchecked contribution from the gradient of the phase. An artificial cutoff R was introduced to avoid divergence. While this excludes the existence of a single infinite global string, a physical cutoff can be imposed by the curvature radius of the string itself or other strings in a network. In other words there exist physical structures which contain the fields rotating phase.

Another possibility is introducing a gauge field which offsets the contribution from the changing phase. A string generated by a local $\tilde{U}(1)$ symmetry hence does not suffer from such a divergence as just described. This will be the next topological defect to be explored.

The thesis is now ready to upgrade the string's symmetry to a gauged symmetry. The formalism will look similar to the one of the global string, except now the presence of a gauge field must be taken into account when computing the equations of motion.

3.1.2 Local strings

The local string can be described by a complex scalar field $\psi(x^\mu)$ charged under a local $\tilde{U}(1)$ symmetry. The Lagrangian is given by

$$\mathcal{L} = \tilde{D}_\mu \psi \tilde{D}^\mu \psi^* - \frac{1}{4} F_{\mu\nu} F^{\mu\nu} - V(|\psi|), \tag{3.14}$$

with the covariant derivative defined as $\tilde{D}_\mu \coloneqq \partial_\mu + ie\tilde{A}_\mu$ and a potential

$$V(|\psi|) = \frac{1}{4}\lambda(|\psi|^2 - \eta^2)^2. \tag{3.15}$$

The same procedures as the global string can now be applied. With the correct ansatz, modified to also include the gauge field, the equations of motion lead to a set of differential equations. These can then be solved numerically to obtain a profile for the amplitudes of the field ψ and the gauge field $\tilde{A}_\mu$.

The equations of motion due to the Lagrangian in Equation 3.14 are first computed and yield the expressions

$$(\partial_\mu - ie\tilde{A}_\mu)(\partial^\mu - ie\tilde{A}^\mu)\psi + \frac{\lambda}{2}(|\psi|^2 - \eta^2)\psi = 0, \tag{3.16}$$

$$\partial_\mu F^{\mu\nu} = 2e\mathrm{Im}\left(\psi^*(\partial^\nu - ie\tilde{A}^\nu)\psi\right). \tag{3.17}$$

The same assumptions as the global string apply here: the string lies along the $z-$axis and the profile is calculated along the distance to the string in the $xy-$plane with a cylindrically symmetric ansatz [55, 56],

$$\psi(\vec{r}) = f(r)e^{in\theta}, \tag{3.18}$$

$$\tilde{A}_i(\vec{r}) = -\epsilon_{ij}x^j\frac{n}{er^2}\alpha(r). \tag{3.19}$$

Here the coordinate x^j runs over x and y. The variables can again be rescaled to units of *vev* $\psi \to \psi/\eta$, $\tilde{A}_i \to \tilde{A}_i/\eta$ and $r \to \eta\, r$. Note that the quantity $f(r)$ is dimensionful and will hence be measured in units of the *vev* η, while the amplitude of the gauge field $\alpha(r)$ is dimensionless and does not get rescaled. The equations of motion reduce to

$$\frac{d^2f}{dr^2} + \frac{1}{r}\frac{df}{dr} - \frac{n^2f}{r^2}(\alpha - 1)^2 - \frac{\lambda}{2}(f^2 - 1)f = 0, \tag{3.20}$$

$$\frac{d^2\alpha}{dr^2} - \frac{1}{r}\frac{d\alpha}{dr} - 2e^2f^2(\alpha - 1) = 0. \tag{3.21}$$

The correct boundary conditions can again be understood as in the global case, that is

$$f(r) \to 1 \quad \text{for } r \to \infty, \tag{3.22}$$

$$\alpha(r) \to 1 \quad \text{for } r \to \infty. \tag{3.23}$$

These boundary conditions demand that both fields tend to their true vacuum configurations far away from the string. The boundary condition for α will become clear when

calculating the energy of the string configuration later in this Section. It is connected to the remarks made in the global string case. To offset the divergent behaviour of the phase, the gauge field has to exist where the gradient of the phase is nonzero.

The conditions at the centre are

$$f(0) = 0, \tag{3.24}$$

$$\alpha(0) = 0. \tag{3.25}$$

The field building the string ψ goes to 0 at the string core, indicating that the system will sit at the center of the Mexican hat potential hill. The value for α must be 0 at the centre since without a defined phase there is no need for a gauge field.

With these components in hand, the numerical analysis of Appendix B.1 can be used to calculate the field profiles for both $f(r)$ and $\alpha(r)$. The results can be seen in Figure 3.6. One can again observe that the field tends to the true vacuum $f = \eta$, while the gauge field arises to compensate the divergent energy of the phase gradient, as discussed in the global string case in Equation (3.13). Close to the string core the field climbs the potential hill $f \to 0$, while the gauge field dissapears.

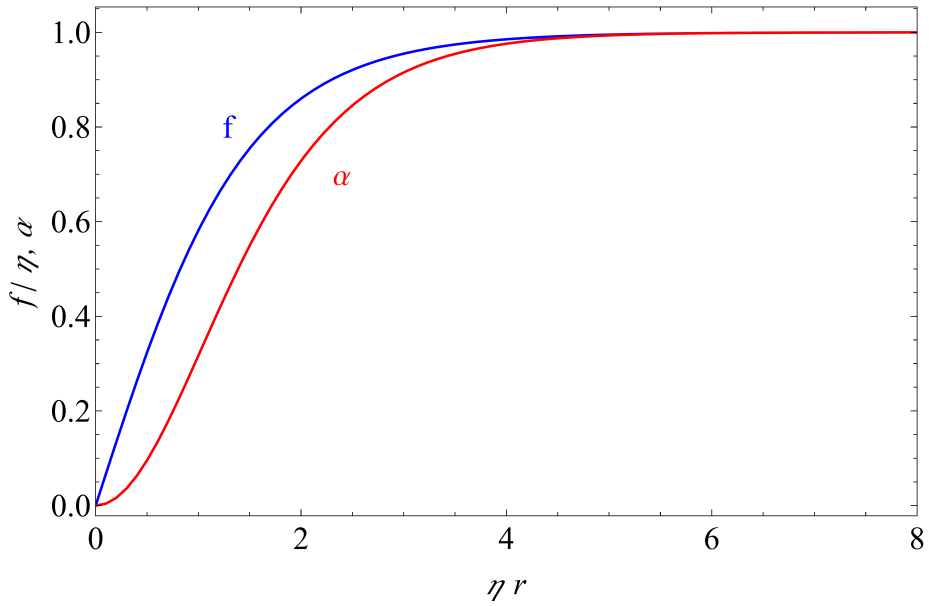

Figure 3.6: The numerical solutions to Equation (3.20) and (3.21) for a winding number $n = 1$ and parameters $\lambda = 1, e = 1$. The coupling constant was not chosen as the EM coupling constant since the later chapter on superconducting strings will show that the gauge field introduced here is not necessarily the electromagnetic four potential.

At a sufficiently large distance away from the string, one can approximate the string as a one dimensional object and average all internal quantities over its cross section

[11]. A string lying across the $z-$axis is invariant under Lorentz transformations in the $z-$direction, hence one can already expect the only nonzero components to be 00 and zz [57]. As an aside, when not stated otherwise, one can always assume this thesis considers a string lying across the $z-$axis [†]. The averaged energy-momentum tensor is given by

$$\tilde{T}^{\mu}{}_{\nu} = \mu\delta(x)\delta(y)\mathrm{diag}\,(1,0,0,1)\,. \tag{3.26}$$

One can observe that the tensor contains no forces perpendicular to the string. Hence when considering a curved string e.g. a circle, no internal forces act perpendicular to the curve. The energy of such a circle can be found by multiplying the energy per unit length with the circle radius R as

$$E_{\mathrm{circle}} \sim \mu R. \tag{3.27}$$

To minimize the energy the system will tend to send the radius to zero $R \to 0$. Hence this form of the tensor indicates that strings which are not completely straight will contract. It contains no stress forces to counteract the lowest energy configuration. Note that this form isn't an exact derivation, but follows from considering the symmetry of the problem. Exactly calculating the energy momentum tensor yields an expression for the total energy of the string solution.

By considering only the $xy-$plane, one can define an energy

$$E = \int d^2r \left(\frac{\partial\mathcal{L}}{\partial(\partial_\mu\psi)}\partial^\nu\psi - g^{\mu\nu}\mathcal{L}\right)^{00}. \tag{3.28}$$

The energy has three contributions: the kinetic part due to the derivatives of the field; the gauged part due to the field strength contributions i.e. the dynamics of the gauge field and the potential contribution,

$$E = \int d^2r|(\nabla - ie\vec{A})\psi|^2 + \frac{1}{2}(\vec{E}^2 + \vec{B}^2) + \frac{1}{4}\lambda(|\psi|^2 - \eta^2)^2. \tag{3.29}$$

To avoid divergences the integrandum should tend to zero as r approaches infinity. The potential term vanishes due to the field ψ taking on its *vev* $\eta e^{i\theta}$. The covariant derivative vanishing imposes a condition on the behaviour of the gauge fields:

$$\vec{A} \to \frac{n}{e}\nabla\theta, \qquad |r| \to \infty. \tag{3.30}$$

To illustrate this behaviour, the complex phase of the ψ field and the direction of the gauge field $\vec{A}$ were mapped in Figure 3.7. This condition on the gauge fields behaviour explains the boundary conditions chosen in Equation (3.23). The behaviour of the gauge

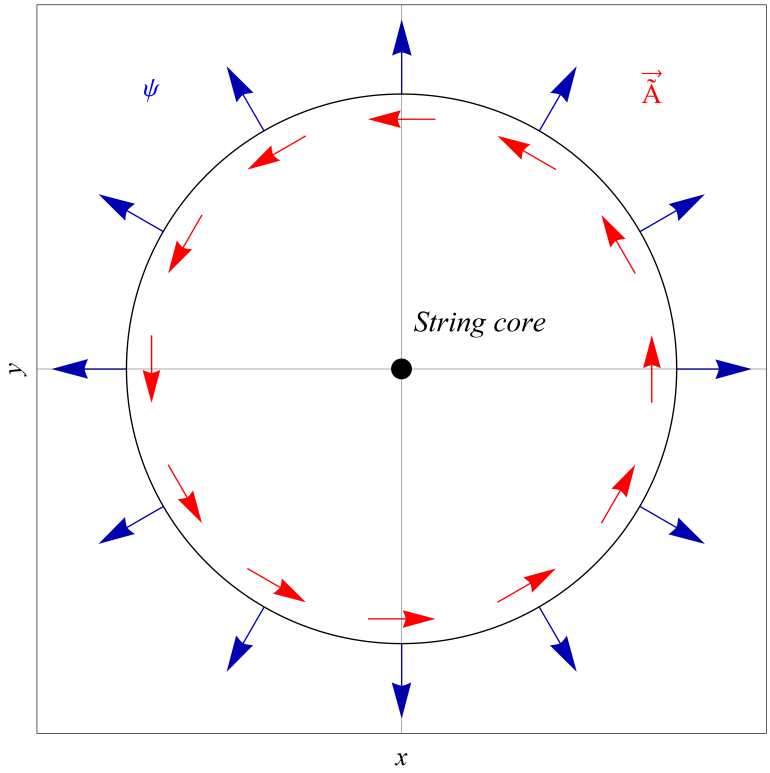

Figure 3.7: The asymptotic field profiles running over a sufficiently large loop around the string core for a winding number $n = 1$. The blue arrows representing ψ indicate the fields phase in complex space e.g. the blue arrow at the top of the circle indicates that the phase of ψ is $\theta = \frac{\pi}{2}$. The red arrows denote the direction of the gauge vector field $\vec{A}$. This sketch only serves to illustrate the behaviour and hence the arrow sizes do not correspond to the absolute field values.

field is such that the energy of the total configuration is finite.

At this point something can also be said about the width of the local string. The global string's width was derived from the Compton wavelength of the scalar field in Equation (3.9). In the case of the local string, the gauge field should also be taken into account. The Compton wavelength of the gauge field when observed far from the string is equal to

$$m_{\tilde{A}} \sim e\eta, \tag{3.31}$$

since the interaction with ψ through the covariant derivatives is the only "mass" term

[†]This is similar to a domain wall, where the energy-momentum tensor's time-time component is equal in size to its space-space components, as will be shown in Chapter 5.

in the Lagrangian. This yields a width

$$\delta_{\tilde{A}} \sim \frac{1}{e\eta}. \tag{3.32}$$

Hence the local string exhibits two characteristic distance scales. The properties of the local string depend on the ratio of these distance scales. In other words the ratio between the scalar particle mass and the gauge vector mass determines the local string behaviour. As an example consider again the energy density per unit length. This can be derived from the energy in Equation (3.29). Since this equation defines the energy in the plane perpendicular to the string, this is already the energy per unit length. Working to lowest order and assuming a cylindrically symmetric field profile, one arrives at an expression [11],

$$\mu \approx 2\pi\eta^2 \ln\left(\frac{m_\phi}{m_{\tilde{A}}}\right), \tag{3.33}$$

assuming that $\delta_{\tilde{A}} > \delta_\phi$. Both regimes $\delta_{\tilde{A}} \lesseqgtr \delta_\phi$ are possible. The current choice was for illustrative purposes only. This indeed shows that local string physics depend on the ratio of the masses.

A great deal more can be said about these different regimes. The regime in which the widths are equal $\delta_{\tilde{A}} = \delta_\phi$ is of particular interest since this assumption allows for rewriting the second order field equations as a system of first order equations. Since we only wanted to demonstrate how a local string depends on the ratio of these scales, the discussion will end here. Interested readers can be referred to [11, 54]. We shall now end the local string Section by showing why the gauge field is an integral, physical part of the local string.

The gauge region is crucial in preserving the string structure. One could argue that everything done up till now for the local string configuration can be undone by simply gauging away the θ behaviour locally. Equation (3.30) seems to imply this, since this looks like a simple gauge transformation. To debunk this claim one can show that for a nonzero winding number this behaviour does represent a physical quantity and hence is not purely a gauge phenomena. The physical quantity implied is a flux of the gauge field running along the string. By integrating over the area on the $xy-$plane which includes the string core, this flux can be found.

$$\Phi_{\tilde{B}} = \int dS\vec{\tilde{B}} = \oint dl\vec{\tilde{A}}. \tag{3.34}$$

Plugging in the behaviour of $\vec{\tilde{A}}$, assuming θ runs around the string n times, yields

$$\Phi_{\tilde{B}} = \frac{2\pi n}{e} \neq 0. \tag{3.35}$$

We found a nonzero physical quantity inside the string core that depends on the winding number. This indicates that the behaviour of the field outside of the string cannot be gauged away, since degrees of freedom that can be gauged away do not represent any physical phenomenon. Note that Figure 3.7 also hints at a nonzero vector $\vec{\tilde{B}} = \nabla \times \vec{\tilde{A}}$ at the string core since the curl of the gauge field is observed to be nonzero.

This concludes the discussion on local strings. It was shown that by introducing a gauge field, the energy density divergence of a global string can be averted. The profiles of both the scalar field and the gauge vector were calculated with the numerical algorithm of Appendix B.1. Finally, it was shown that local strings exhibit a nonzero flux inside the string core, proving that the configuration cannot be trivially gauged away.

3.2 Strings in the early Universe

To conclude this chapter, some brief final words can be said on the formation of strings in the early Universe. For a complete review of cosmic strings [58] can be consulted.

As described in Chapter 2.1.3, topological defects can form after spontaneously breaking a symmetry in a phase transition. The Kibble mechanism [19] was at the basis of this process happening, stating that regions sufficiently far apart choose their vacuum independently. In the case of breaking a $\tilde{U}(1)$ symmetry, the choice ranges over $[0, 2\pi[$. In a second order phase transition, the field gradually moves away from the unbroken phase at $\psi = 0$ everywhere. When disconnected regions form a scenario in which a loop runs through a phase $2\pi n$, a string can be formed.

A first order phase transition allows for bubbles of the broken state to appear in an unbroken Universe. When three or more of these bubbles meet a string can be formed at their meeting focal point, given that the difference in phase between the bubbles is $2\pi n$. This is shown in Figure 3.8.

Hence for the right phase transition the formation of a string network is certainly possible. Note that the EW phase transition at $T \sim 100$ GeV does not give rise to stable strings, while one could expect that the vacuum manifold of the $\tilde{U}(1)$ symmetry contains non contractable loops. It is the coupling to the SU(2) symmetry group that enlarges the vacuum manifold and provides a "backdoor" for loops in the $\tilde{U}(1)$ vacuum manifold to contract. In other words, when a situation arises in which the phase runs over modula 2π over a closed loop, the system has other options apart from forming a string at the center [58].

We can conclude that strings form in an as yet unobserved phase transition. Examples include Grand Unified Theories, which combine the symmetries of the Standard Model in a greater symmetry group. Breaking these symmetries in a phase transition could satisfy the homotopy condition that a noncontractable mapping of S^1 exists in the vacuum manifold.

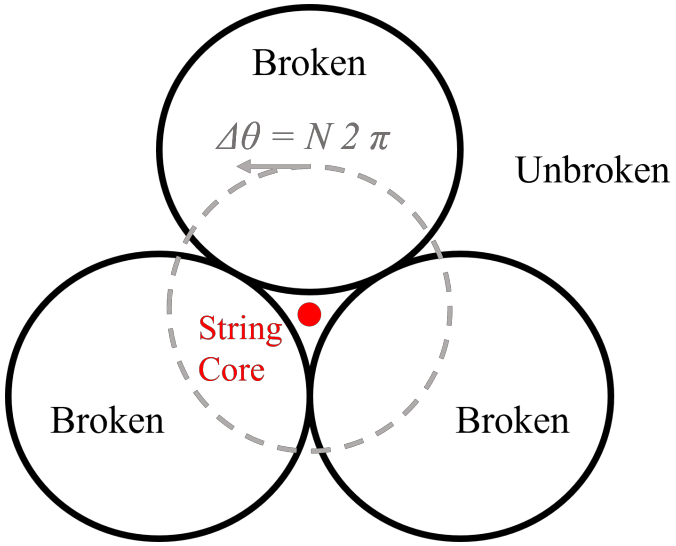

Figure 3.8: Scenario in which three bubbles of a broken phase collide, trapping a string between them. The overall phase difference between the three broken phases is $\Delta\theta = 2\pi n$.

Although this subsection barely scratches the surface on the behaviour of cosmic string in the early Universe, it will end on this brief discussion. The goal was to describe how strings can form out of phase transitions to demonstrate their plausibility.

We have now described cosmic strings and their field theory and applied a numerical algorithm to find the field profile of both a global and local string. The thesis is now ready to move on to Witten's superconducting strings.

4 Superconducting strings

The basic cosmological string can also be coupled to another complex scalar field. This field exhibits a local U(1) symmetry, gauged by a gauge vector which can be interpreted as the photon. This configuration allows for breaking the local U(1) symmetry in the string core. This chapter aims to elaborate on this configuration and show that this setup leads to superconductivity by proving the criteria set out in Chapter 2.3. The field profiles will be calculated in a similar way to Chapter 3. The stability of the superconducting string will be proven, after which a persistent current and the Meissner effect will be shown. Finally, a mechanism in which the string acquires non zero charge will be set out.

This chapter will review and re-elaborate the results obtained by Witten in [7] about superconducting strings. The Meissner effect applied to superconducting strings is original work. The goal is to apply these ideas to domain walls in the following chapters.

4.1 Superconducting string configuration

First introduced by Edward Witten in 1985 [7], a superconducting string consists of the cosmic string described in Chapter 3 coupled to another complex scalar field exhibiting another local $U(1)$ symmetry. The configuration depends on the strings scalar field coupling to what will be called the condensate: a field which has a vacuum value 0 outside of the string and only becomes nonzero in the string core.

The scalar potential describing the interactions of the scalar field will be such that it admits a string solution with the following properties for the two scalar fields: outside of the string, the field constructing the string ϕ should break $\tilde{U}(1)$, while the condensate field σ should still be unbroken and takes on value 0. This should be the energetically favourable setup i.e. the $\phi \neq 0$, $\sigma = 0$ configuration should compose the lowest possible potential. This to allow the Universe to build strings of the ϕ field. Inside the string the roles should reverse, since ϕ tends to 0 in the string core, the field σ should take on a non zero value to compensate and keep the potential low.

For now, we will denote the nonzero value of the condensate $\sigma \neq 0$ inside the string core as the condition for superconductivity. The reason for this will be elaborated upon later in this chapter.

The Lagrangian of this configuration is [7, 11]

$$\mathcal{L} = \tilde{D}_\mu \phi (\tilde{D}^\mu \phi)^* + D_\mu \sigma (D^\mu \sigma)^* - \frac{1}{4}\tilde{F}_{\mu\nu}\tilde{F}^{\mu\nu} - \frac{1}{4}F_{\mu\nu}F^{\mu\nu} - V(|\phi|, |\sigma|), \tag{4.1}$$

with a potential

$$V(|\phi|, |\sigma|) = \frac{1}{4}\lambda_\phi \left(|\phi|^2 - \eta_\phi^2\right)^2 + \frac{1}{4}\lambda_\sigma \left(|\sigma|^2 - \eta_\sigma^2\right)^2 + \beta |\phi|^2 |\sigma|^2. \tag{4.2}$$

The field ϕ will built the string and is gauged by the vector $\tilde{A}^\mu$, while the field σ is the condensate, gauged by A^μ, and will be responsible for superconductivity. Note that the

potential is a combination of two Mexican Hat potentials for each field, coupled by the final term $\beta|\phi|^2|\sigma|^2$. This final term is what ensures that the two fields cannot break the symmetry simultaneously, given that β is chosen sufficiently large compared to the other parameters.

The covariant derivatives are defined as

$$\tilde{D}_\mu = (\partial_\mu + ig\tilde{A}_\mu), \quad D_\mu = (\partial_\mu + ieA_\mu). \tag{4.3}$$

The field strengths are

$$\tilde{F}_{\mu\nu} = \tilde{A}_\mu\tilde{A}_\nu - \tilde{A}_\nu\tilde{A}_\mu, \quad F_{\mu\nu} = A_\mu A_\nu - A_\nu A_\mu. \tag{4.4}$$

The parameters should be chosen carefully as to fulfill what was discussed in the first paragraph: $(\phi \neq 0, \sigma = 0)$ should be the absolute minimum. The minima of this potential in the (ϕ, σ) plane are

$$\min_\phi = (\pm\,\eta_\phi, 0), \qquad \min_\sigma = (0, \pm\,\eta_\sigma), \tag{4.5}$$

where the subscripts denote which field takes on a nonzero value. The values of the potential for these minima are:

$$V(\min_\phi) = \frac{1}{4}\lambda_\sigma\eta_\sigma^4, \qquad V(\min_\sigma) = \frac{1}{4}\lambda_\phi\eta_\phi^4. \tag{4.6}$$

To demand that the "normal" configuration is of the form $(\phi \neq 0, \sigma = 0)$, $\min_\phi$ should be the absolute minimum, leading to the condition

$$\text{Vacuum condition:} \quad \lambda_\phi\eta_\phi^4 > \lambda_\sigma\eta_\sigma^4. \tag{4.7}$$

The conditions will be named to clearly keep track of them. To illustrate this, the potential is plotted in the (ϕ, σ) plane in Figure 4.1.

The red arrow in Figure 4.1 indicates the behaviour of the fields as they approach the string core. ϕ's local U(1) symmetry is spontaneously broken far away from the core. σ retains its symmetry as long as ϕ takes on its *vev*. Far away from the cosmic string the system hence stays in its lowest energy state.

When approaching the cosmic string, this regime changes. As ϕ moves away from its true *vev* the σ profile becomes non trivial. Of course, $\sigma = 0$ also solves the equations of motion, since this reverts the system back to the non-coupled cosmic string. The plausibility of σ taking on nonzero values will depend on the parameter values. The next section investigates when a superconducting string configuration is stable by applying a perturbation analysis similar to Witten's argument [7].

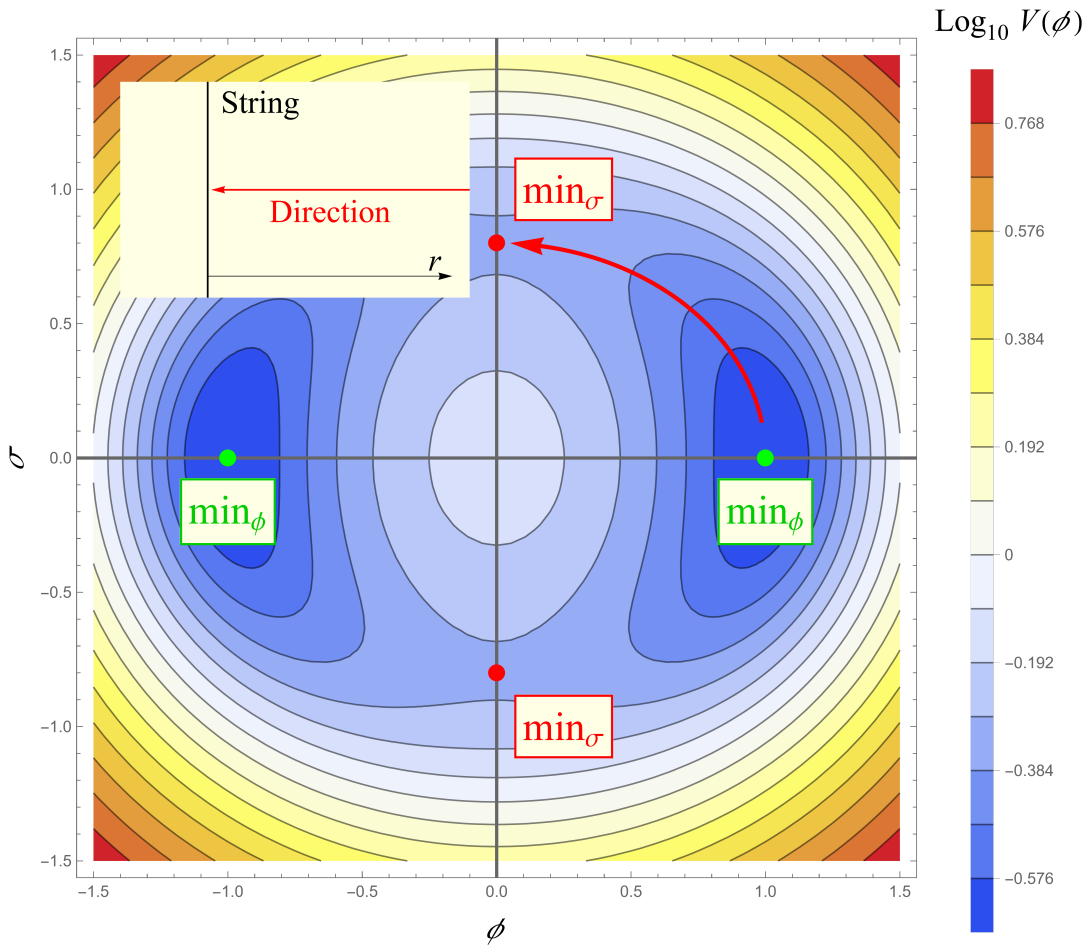

Figure 4.1: $\log_{10}$ of the potential $V(\phi, \sigma)$ defined in Equation 4.2. The green points denote $\min_\phi$, while the red dots denote $\min_\sigma$. The arrow denotes a sketch of the shift of the fields in the (ϕ, σ) plane when approaching the string core. The path of the arrow in the (x, y, z) space is shown in the box. The arrow lives in a plane perpendicular to the string, where the coordinate r denotes the distance to the string core.

4.2 Perturbation analysis

To test the stability of the superconducting string configuration, one can consider the regular cosmic string as a background perturbed by the σ field. The parameters for which the perturbation grows indicate an unstable cosmic string configuration and the fields will strive to evolve to the superconducting regime i.e. $\sigma \neq 0$ in the string core. The perturbation with coordinates x^μ is

$$\begin{cases} \sigma(x^\mu) = 0 + \delta\sigma(x^\mu) \\ A^\mu(x^\mu) = 0 \end{cases}, \tag{4.8}$$

Inserting this into the Lagrangian and computing the equations of motion of $\delta\sigma$ yields

$$\Box\delta\sigma + \frac{\partial V}{\partial \delta\sigma} = 0, \tag{4.9}$$

$$\Leftrightarrow \quad \Box\delta\sigma + (\beta|\phi|^2 - \frac{1}{2}\lambda_\sigma\eta_\sigma^2)\delta\sigma = 0. \tag{4.10}$$

Assuming the cosmic string lies along the z-axis, one can look at the behaviour of the σ field in the plane perpendicular to the string with an ansatz

$$\delta\sigma(t, x, y, z) = \delta\sigma(x, y, t) = e^{-i\omega t}\delta\sigma_0(x, y). \tag{4.11}$$

If solutions to the equations of motion admit values $\omega^2 < 0$ the perturbation will grow exponentially and the $\sigma = 0$ groundstate will be unstable. Plugging this ansatz into Equation 4.10 reduces the equation of motion to a Schrödinger equation

$$-\Delta\delta\sigma_0 + (\beta|\phi|^2 - \frac{1}{2}\lambda_\sigma\eta_\sigma^2)\delta\sigma_0 = \omega^2\delta\sigma_0. \tag{4.12}$$

The Schrödinger equation has a potential $\beta|\phi|^2 - \frac{1}{2}\lambda_\sigma\eta_\sigma^2$. Far away from the string this takes the form $\beta\eta_\phi^2 - \frac{1}{2}\lambda_\sigma\eta_\sigma^2$. In this regime a perturbation should die out, since the condensate field should only take on nonzero values inside the string core. The potential far away from the string core should be positive as to avoid exponential growth of the perturbation. Hence this yields another condition on the parameters,

$$\text{Stability condition:} \quad \beta\eta_\phi^2 - \frac{1}{2}\lambda_\sigma\eta_\sigma^2 \geq 0. \tag{4.13}$$

When approaching the string core, the field ϕ begins tending to 0. The exact behaviour of the ϕ field cannot be analytically calculated and depends on a numerical analysis which will be performed later in this chapter. One can however guess ϕ to first order by considering the assumption made for the string width in Equation (3.9) and letting ϕ go linearly from η_ϕ to 0 in this interval. To first order, with the distance to the string denoted as r, ϕ can be guessed as

$$\phi(r) \approx \sqrt{\frac{\lambda_\phi}{2}}\eta_\phi^2 r. \tag{4.14}$$

Plugging this approximation into the potential in Equation 4.12 yields

$$V_{Schrod} \approx \beta \frac{\lambda_\phi}{2} \eta_\phi^4 r^2 - \frac{1}{2} \lambda_\sigma \eta_\sigma^2. \tag{4.15}$$

One can now recall that the perturbative analysis is performed on the condensate σ, hence r can be guessed as the scale over which the σ field behaves non trivially. Similarly to ϕ, this scale can be interpreted as the Compton wavelength of σ, $\delta_\sigma \sim \sqrt{\frac{2}{\lambda_\sigma}} \frac{1}{\eta_\sigma}$. Substituting $r = \delta_\sigma$ into Equation 4.15 yields a final guess for the potential in terms of the parameters

$$V_{schrod} \approx \beta \lambda_\phi \eta_\phi^4 \frac{1}{\lambda_\sigma \eta_\sigma^2} - \frac{1}{2} \lambda_\sigma \eta_\sigma^2. \tag{4.16}$$

A Shrödinger equation with such a negative definite potential has bound states with negative energies and hence $\omega^2 < 0$. Setting this condition inside the string gives a bound on the parameters

$$\text{Condensate condition} \quad \frac{\beta}{\lambda_\sigma} \lesssim \frac{1}{2} \frac{\lambda_\sigma \eta_\sigma^4}{\lambda_\phi \eta_\phi^4}. \tag{4.17}$$

This proves that for a well chosen range of parameters, $\sigma = 0$ is unstable inside the string core and a condensate can be formed. This leads to a conservative condition on the parameter space.

We can now estimate whether the condition for superconductivity as found in Equation (4.17) can be fulfilled by non-fine tuned choices of parameters in the potential. A natural range of parameters would be that all parameters of the same order are similar. For example all parameters connected to a quartic term in the Lagrangian are $\beta \sim \frac{\lambda_\phi}{4} \sim \frac{\lambda_\sigma}{4}$. The quadratics yield $\lambda_\phi \eta_\phi^2 \sim \lambda_\sigma \eta_\sigma^2 \Rightarrow \eta_\phi^2 \sim \eta_\sigma^2$. Plugging these in Equation (4.17) would show

$$\frac{\beta}{\lambda_\sigma} \lesssim \frac{1}{2}, \tag{4.18}$$

which is indeed satisfied when $\beta \sim \frac{\lambda_\sigma}{4}$. This shows that the configuration for a superconducting string does not require exotic or finetuned choices of parameters to be stable, confirming their plausibility. This concludes the perturbative analysis of the superconducting string Lagrangian.

In what follows, it will be assumed that the parameters of the theory satisfy the vacuum (4.7), stability (4.13) and condensate (4.17) conditions.

4.3 Superconductivity

After exploring the potential of the superconducting string in Equation 4.2, this chapter set out to prove the stability of the superconducting configuration. It was shown that reasonable parameter choices do indeed lead to a stable field profile. Now this thesis is ready to prove that superconductivity indeed follows from the Lagrangian in 4.1. The goal is to recreate the double argument made in [7]: proving a current on a loop does not dissipate and proving the Meissner effect. To achieve this the theory will be reduced to an effective theory in $1+1$ dimensions.

4.3.1 Effective theory

The general equations of motion for the full Lagrangian include both the string structure and the electromagnetic properties in the string core.

$$(\partial^\mu + ig\tilde{A}^\mu)(\partial_\mu + ig\tilde{A}_\mu)\phi + \frac{1}{2}\lambda_\phi(|\phi|^2 - \eta_\phi^2)\phi + \beta|\sigma|^2\phi = 0, \tag{4.19}$$

for the field ϕ and

$$(\partial^\mu + ieA^\mu)(\partial_\mu + ieA_\mu)\sigma + \frac{1}{2}\lambda_\sigma(|\sigma|^2 - \eta_\sigma^2)\sigma + \beta|\phi|^2\sigma = 0, \tag{4.20}$$

for the field σ.

The equations of motion for the gauge field $\tilde{A}^\mu$ is given by

$$\partial_\mu \tilde{F}^\mu{}_\nu = ig\left(\phi^*\tilde{D}_\nu\phi - \text{h.c.}\right) \tag{4.21}$$

and similarly for A^μ,

$$\partial_\mu F^\mu{}_\nu = ie\left(\sigma^* D_\nu\sigma - \text{h.c.}\right). \tag{4.22}$$

The goal now is defining an effective theory which only describes the behaviour of the condensate along the string. This effective theory will describe σ and its coupling to A^μ in $1+1$ dimensions, these being t and z for a string lying along the $z-axis$. In other words the effective theory considers the string as a one dimensional object. This will be motivated shortly with an example.

This reduced theory will allow for identifying the charge carriers along the string and proving that their behaviour leads to superconductivity.

It is important to note that the gauge field $\tilde{A}^\mu$ will no longer appear in expressions after this point. It only exists to maintain the stability of the local string, as discussed

in Chapter 3. One can interpret the local string as a background on which an effective theory will be built. The gauge field $\tilde{A}^\mu$ will only reappear when considering the numerical profiles of the superconducting string fields. We can now start constructing the effective theory.

With the goal of building a $1+1$ dimensional field theory in mind, one can define an ansatz that splits the behaviour of σ into a static contribution from the plane perpendicular to the string, the xy-plane and the direction in which the string lies. We can assume a static xy-profile is justified, since Section 4.2 showed that a stable nonzero condensate profile exists in the directions perpendicular to the string when the parameters satisfy the condensate condition in Equation (4.17). In other words, we are considering a system in which a stable condensate has already formed.

The ansatz made by Witten in [7] provides this formalism and is written as

$$\begin{cases} \sigma(t,x,y,z) &= \sigma_0(x,y)e^{i\theta(t,z)} \\ A_\mu(t,x,y,z) &= A_\mu(t,0,0,z) \end{cases}, \tag{4.23}$$

in which $\sigma_0(x,y)$ minimizes the potential given in Equation (4.2). By extension this ansatz also minimizes the potential. The goal of this ansatz is to define equations of motion of perturbations on the string, parameterised by the real function $\theta(t,z)$.

The second assumption is to keep A^μ slowly varying in the directions perpendicular to the string as

$$A^\mu(t,x,y,z) = A^\mu(t,0,0,z). \tag{4.24}$$

We will take some time to motivate this assumption, since the motivation can also serve as an example for considering the string as a one dimensional object.

One can justify this by considering the dimensions of the string. The width of the flux tube of the gauge field δ_A in the xy-plane, is determined by its effective mass and can be estimated as

$$\delta_A \sim \frac{1}{m_A} \approx \frac{1}{\sqrt{2}e\eta_\sigma}. \tag{4.25}$$

By plugging in natural choices for the parameters, one can estimate this width. A natural choice for the quartic coupling would be $\lambda_\sigma \sim 1$. A choice for η_σ can be motivated by considering the critical temperature at which the strings were formed. Equation (2.17) states

$$T_c \sim \eta_\phi, \tag{4.26}$$

which allows for estimating the scale of η_ϕ when considering at what temperatures known and theorised phase transitions occur. As a representative value we can choose the electroweak phase transition [‡] at $T_c \sim 100$ GeV. Another natural choice for the parameters is that the two *vevs* are of similar order $\eta_\phi \sim \eta_\sigma$. With these choices the gauge vector width becomes of order $\delta_A \sim 10^{-2}$ GeV^{-1} i.e. of atomic order. When considering that the string length is of a cosmological order H^{-1} it is justified to keep quantities like A^μ independent of the directions perpendicular to the string.

The same considerations can be applied to the widths of the scalar fields, δ_ϕ and δ_σ, leading to a justification for considering the string as a one dimensional object

Now that the ansatz is justified, it can be substituted into the Lagrangian of Equation 4.1. Only retaining the terms which explicitly contain the perturbations $\theta(t, z)$ leads to a reduced expression

$$\mathcal{L}_\theta = (\partial_t\theta + eA_t)^2|\sigma_0|^2 - (\partial_z\theta + eA_z)^2|\sigma_0|^2. \tag{4.27}$$

Note that the terms in x and y were not included since these do not contain a factor $\theta(t, z)$. This partial Lagrangian can be used to construct an effective action

$$S_\theta = K \int dtdz(\partial_t\theta + eA_t)^2 - (\partial_z\theta + eA_z)^2, \tag{4.28}$$

in which K is defined as the behaviour of the condensate integrated over the $xy-$plane $K = \int dxdy|\sigma_0(x, y)|^2$. As sidenote, this K can be estimated by assuming a constant σ_0 over the cross section of the string, which has a diameter δ_σ. The constant σ_0 can be guessed by its maximum η_σ,

$$K = \int dxdy|\sigma_0|^2 \approx \delta_\sigma^2\eta_\sigma^2 \sim \frac{1}{\lambda_\sigma}, \tag{4.29}$$

in which an approximation for the width of the condensate

$$\delta_\sigma \sim \frac{1}{\sqrt{\lambda_\sigma}\eta_\sigma} \tag{4.30}$$

was used.

Physically, the $xy-$ behaviour was integrated out to create an action which only returns the physics of the Goldstone Bosons θ along the string, which were created by σ breaking a local U(1) symmetry inside the string core.

To get the full effective action the dynamics of the gauge vector are included.

[‡]Although strings made during the EW phase transition are not stable, other candidate phase transitions are found at even higher temperatures, hence the EW phase transition can serve as a conservative guess.

$$S_{EM} = -\frac{1}{4}\int d^4x F_{\mu\nu}F^{\mu\nu} \tag{4.31}$$

$$S_{eff} = S_\theta + S_{EM}. \tag{4.32}$$

The variables in this action only depend on t and z due to the reduction of the condensate σ to the real field $\theta(t, z)$ and the assumption that A^μ does not depend on the directions perpendicular to the string as shown in Equation (4.24). Thus a $3+1$ dimensional action was just reduced to solving the dynamics of a $1 + 1$ dimensional problem, coupled to $3 + 1$ dimensional electromagnetism.

As a final step one can calculate the equations of motion for the field θ and gauge vector A^μ.

$$\Box\theta + e\partial_\mu A^\mu = 0, \tag{4.33}$$

$$\partial_\mu F^{\mu\nu} + 2Ke(\partial^\nu\theta + eA^\nu) = 0. \tag{4.34}$$

With this formalism in hand, one can now begin proving the superconductivity. This will be done in two steps. First, it will be shown that a current on a closed string loop does not dissipate, hence proving the electromagnetic resistance drops to zero. To fully prove superconductivity one has to also include the Meissner effect. This cannot be explained by simple stating that the string exhibits perfect currents.

4.3.2 Persistent current

This subsection aims to prove that a current on a looped string can persist indefinitely. This will be shown by defining a current and comparing the equations of motion of the gauge field coupled to the condensate with Maxwell's equations. After that one can prove that such a loop contains a nonzero topologically invariant number, which leads to a constant, nonzero expression for the current.

To define a current one can compare the equations of motion of the gauge vector in Equation (4.34) with the Maxwell equation $\partial_\mu F^{\mu\nu} = j^\nu$.

$$j^\nu := -2Ke(\partial^\nu\theta + eA^\nu) \tag{4.35}$$

The goal is to check whether the electromagnetic current i.e. the spatial component of j^ν is nonzero in the groundstate of a looped string. The loop is defined with a circumference $2\pi R$. The topologically invariant number hinted at before will be denoted as N and is the winding number of the perturbation on the field σ on the closed string. The perturbation θ runs around this loop N times. Since θ was defined as a phase, it is only determined up to a modulo 2π. This setup is illustrated in Figure 4.2.

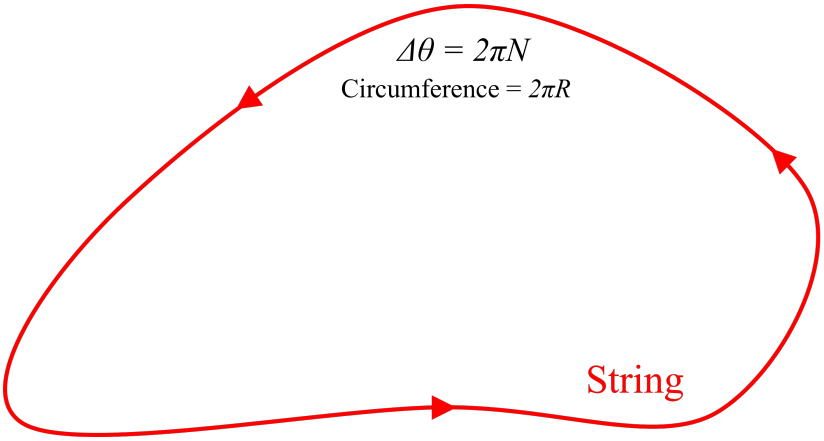

Figure 4.2: The string loop setup to investigate the current running through the superconducting string. The circumference of the loop is $2\pi R$, while the excitation on the σ field runs around its phase space N times over one circumference.

Equation (4.34) can be used to find an expression for the gauge vector in function of the current. The electromagnetic current is the quantity under investigation and hence the spacelike components of the four current will be considered. The spacelike components will be indexed with Latin letters $i, j, k, ...$

$$\Delta A_i(t, \vec{x}) = j_i(t, \vec{x}). \tag{4.36}$$

Here the Coulomb gauge, $\nabla \vec{A} = 0$, was chosen. This equation can be rewritten using the Green's function for the Laplace operator Δ. The quantities under consideration are the spacelike gauge vector components parallel to the loop direction. Since the excitations only have a spacelike component along the string, due to the ansatz in Equation (4.23), Equation (4.35) and Equation (4.36) indicate that the only components of the gauge vector that appear in the electromagnetic current $\vec{j}$ are exactly these under consideration,

$$A_i(\vec{x}) = -\frac{1}{4\pi} \oint dl \frac{j_i(\vec{x}(l))}{|\vec{x} - \vec{x}(l)|} \tag{4.37}$$

The loop was parameterised by the coordinate l. Note that the current only takes on the loop coordinates since it can only be defined inside of the string core along the loop direction. The previous derivations and discussions with a string along the $z-$axis are still valid since these string loops are typically of radii in the order of cosmic distances. Hence they can locally be approximated as straight.

Now it is time to recall the starting goal. To find a nonzero current in the lowest energy ground state for a nonzero winding of the excitation N. Since the regime is in the lowest energy state, one can observe that the current along the string should be constant. The point is proving that this constant is nonzero.

Equation (4.37) can be approximated by considering the current as constant and stating that the only dimensional parameters of the problem are the curvature radius of the string R and the string width δ_σ. The integral $\oint dl \frac{1}{|\vec{x}-\vec{x}(l)|}$ would be divergent for a string of zero width. It has to be modified when considering a realistic string of nonzero width. This yields an approximation for the gauge vector inside the string [7],

$$A_i(\vec{x}(l) \approx -\frac{1}{2\pi} \ln\left(\frac{R}{\delta_\sigma}\right) j_i(\vec{x}(l)). \tag{4.38}$$

As stated before, both the components of $\vec{A}$ along the string and the current along the string are constant when considering the lowest energy state. Equation 4.35 indicates that the spacelike derivative of the excitation θ is also constant,

$$\partial_i \theta = \text{Cst.} \tag{4.39}$$

Since the excitation runs over $2\pi N$ with $N \in \mathbb{N}$ over one loop of circumference $2\pi R$, the change in θ along the string can be approximated as

$$\partial_i \theta \approx \frac{N}{R} \tag{4.40}$$

Now both approximation in Equations (4.38) and (4.40) can be substituted in the definition of the current in Equation (4.35) to obtain an expression for the current

$$j_i(\vec{x}(l)) = \frac{2Ke}{1 + \frac{Ke^2}{\pi} \ln\left(\frac{R}{\delta_\sigma}\right)} \frac{N}{R}. \tag{4.41}$$

Hence by defining a current in line with Maxwell's equations and inferring the correct quantities to be static in the lowest energy state a nonzero current was found for a winding number $N \neq 0$. This constant current indicates that a zero resistance regime is in place when considering the lowest energy state. This derivation recreated Witten's arguments closely. In the next section the Thesis will deviate from these arguments and prove another aspect of a superconductor: the Meissner effect.

4.3.3 Meissner effect

The current defined in Section 4.3.2 can be employed to show a dampening of external magnetic fields inside the string. As discussed in Chapter 2.3, the photons obtain a mass inside a superconducting string by the symmetry breaking. This mass will act as a dampening factor, which makes the magnetic field die out exponentially. By simple vector calculus and using Maxwell's equations, the definition of the current in Equation (4.35) leads to the Meissner effect.

To prove this, the spatial components of Equation (4.34) will be rewritten in terms of the magnetic vector $\vec{B}$ with components B^i, defined as

$$B^i \coloneqq -\frac{1}{2}\varepsilon^{ijk}F_{jk}, \tag{4.42}$$

in which ε^{ijk} is the Levi-Civita tensor, chosen as $\varepsilon_{012} = +1$. The electromagnetic field strength of Equation (4.34) $\partial_i F^{ij}$ can be expressed as the curl of the magnetic field vector. The curl of a vector is defined as

$$\left(\nabla \times \vec{B}\right)^i \coloneqq \varepsilon^{ijk}\partial_j B_k. \tag{4.43}$$

substituting B^k with Equation (4.42) yields

$$\left(\nabla \times \vec{B}\right)^i = -\frac{1}{2}\varepsilon^{ijk}\partial_j \varepsilon_{klm}F^{lm}, \tag{4.44}$$

which can be rewritten by using a property of the Levi-Civita tensor $\varepsilon_{ijk}\varepsilon^{lmk} = (\delta^l_i\,\delta^m_j - \delta^m_i\,\delta^l_j)$

$$\left(\nabla \times \vec{B}\right)^i = -\frac{1}{2}\partial_j(\delta^i_l\,\delta^j_m - \delta^i_m\,\delta^j_l)F^{lm}, \tag{4.45}$$

$$= \partial_j F^{ji}. \tag{4.46}$$

The last step used the anti-symmetry of the field strength tensor. One can now substitute this in Equation (4.34). This yields

$$\left(\nabla \times \vec{B}\right)^i = -2Ke(\partial^i\theta + eA^i). \tag{4.47}$$

The discussion again reverts to a string along the $z-$axis. Since only the z component of the gauge field couples to the current on the string, we pick a gauge $A_t = A_x = A_y = 0$ as was done in Witten [7]. Furthermore one can assume that $A_z(t,x,y,z) = A_z(t,x,y)$ since the problem is independent of z due to the invariance of an infinite string under Lorentz boosts along the $z-$ axis. All these assumptions can be thought of as a consequence of the current only living on the string i.e. the z-axis. A vector notation makes the calculations much easier and hence the gauge vector will be rewritten as

$$\vec{A} = -\begin{pmatrix} 0 \\ 0 \\ A_z \end{pmatrix}. \tag{4.48}$$

Note the minus sign due to the metric. The derivative on the excitation θ will be written as

$$\partial_z \theta = \nabla \theta. \tag{4.49}$$

∂_z was interpreted as the gradient since the only spatial dependency of θ is in the z-direction $\theta = \theta(t, z)$.

Plugging these definitions into the equation of motion found in Equation (4.47) yields

$$\nabla \times \vec{B} = 2Ke(\nabla\theta - e\vec{A}). \tag{4.50}$$

One can now take the curl of the left and right hand side and apply the vector identity $\nabla \times \nabla \times \vec{B} = \nabla(\nabla \cdot \vec{B}) - \nabla^2 \vec{B}$ together with the definition of the electromagnetic potential vector $\nabla \times \vec{A} = \vec{B}$,

$$\nabla(\nabla \cdot \vec{B}) - \nabla^2 \vec{B} = -2Ke^2 \vec{B}. \tag{4.51}$$

The θ was eliminated by applying the vector identity $\nabla \times (\nabla\theta) = 0$. By using Maxwell's second equation $\nabla \cdot \vec{B} = 0$, one can reduce the equation even more.

$$\nabla^2 \vec{B} = 2Ke^2 \vec{B} \tag{4.52}$$

This is the final result that illustrates the Meissner effect. A magnetic field entering the string will be dampened by a factor $2Ke^2$.

Consider as an example $\vec{B}$ to be moving in the x-direction with a polarisation in the $y-$direction. Equation (4.52) reduces to a simple differential equation:

$$\frac{d^2}{dx^2} B = 2Ke^2 B \tag{4.53}$$

$$B = B_0 e^{-\sqrt{2K}ex} \tag{4.54}$$

This exponential decay is exactly the Meissner effect described in Section 2.3. Hence this Section managed to show both the ability to maintain a current without losing energy and the dampening of magnetic fields. One can now state that the string described by the Lagrangian in Equation (4.1) is superconducting.

4.4 Charging mechanism

After proving superconductivity one can ask what new mechanisms come along with this property, in particular what mechanism initiates the current living on the string. This section sets out to show that by interacting with external electric fields, the superconducting string can acquire and increase its current. This scenario is plausible since

cosmic strings live in the early Universe plasma. In that environment, several physical phenomena can produce electric fields to interact with the strings.

The goal is to derive a formula of the form $\partial_t j^z = ...$ for a string along the $z-$axis. The four-current living on the string is composed of the energy density and the current vector. In this case this current vector's only nonzero component is the z component. This is justified since a string along the $z-$axis can be approximated as a $1+1$ dimensional object.

$$j^\mu = \left(j^t, 0, 0, j^z\right). \tag{4.55}$$

Due to the string being invariant under Lorentz boosts in the $z-$direction, it is an acceptable ansatz to consider the energy density to be invariant along the string. This can be translated as a condition on the string:

$$\partial_z j^t = 0. \tag{4.56}$$

When plugging in the definition of the current (4.35) one obtains

$$\partial_z \partial^t \theta = -e \partial_z A^t \tag{4.57}$$

What is left is to calculate the time derivative of the current defined in Equation (4.35), assuming the only non zero spatial component is the $z-$component,

$$\partial_t j^z = -2Ke\partial_t \left(\partial^z \theta + eA^z\right). \tag{4.58}$$

Plugging in Equation (4.57) yields a final result

$$\begin{aligned} \partial_t j^z &= -2Ke^2 \left(\partial_z A^t + \partial_t A^z\right), && (4.59)\\ &= 2Ke^2 \left(\partial_t A_z - \partial_z A_t\right), && (4.60)\\ &= 2Ke^2 E^z, && (4.61) \end{aligned}$$

in which the final step used the definition of the electric field in function of the field strength,

$$E^z = -F^{tz} = \partial_t A_z - \partial_z A_t. \tag{4.62}$$

This concludes the proof that an electric field, as can be created by the cosmic plasma, can create a charge along the superconducting string. Equation (4.61) provides

a mechanism that links the current directly with an external electric field. Superconducting strings can form with no initial current, for example when the condensate takes the value $\sigma = \sigma_0$ everywhere, which corresponds with a $\theta = \theta(t)$ scenario in the ansatz (4.23), but they obtain a current due to their interaction with the cosmic plasma.

We should note that this derivation assumed that the full external electric field can penetrate up to the superconducting string core. In reality the electric field is dampened to an extent, due to the scattering of photons on the superconducting string. This was modelled in [7] by modifying the electric field E^z with an efficiency parameter. This efficiency is calculated by Witten to be the ratio of the field at the center of the string over the incoming field. In deriving the superconducting domain walls in Chapter 6, we will propose how this efficiency parameter can be approximated and computed for the case of superconducting domain walls.

A final remark on this charging mechanism is that it does not work indefinitely. Strings cannot acquire arbitrary amounts of energy by charging up to an arbitrarily high current. As is common in physics, there exists an energy/current cut-off after which the theory breaks down. The key of this breakdown lies with the symmetry breaking. The effective theory described in Section 4.3.1 integrated out the behaviour of the condensate in the plane perpendicular to the string by collecting σ_0 in the parameter K and approximating K as a constant, as seen in Equation (4.28).

The original behaviour of the fields coupled to the current can be seen in Equation (4.27). One sees that a current along the string appears as a quadratic term for the field σ_0. Incorporating this term in the effective potential enhances parabolic behaviour. One can also interpret this as the current contributing to an effective mass for the condensate. The higher this mass, the less energetically favourable it is for the system to maintain a nonzero condensate inside the string core.

In other words the larger this term the more the effective potential reverts back to a simple parabola. Hence for large currents the true minimum will revert back to $\sigma = 0$ and restore the symmetry. This behaviour falls outside of the scope of the effective theory, since it assumes a nonzero condensate. One can nonetheless see that the current stops growing when $\sigma \to 0$, since this would make $K \to 0$ in Equation (4.61). To illustrate this a crude guess for the maximum current can be found by observing the minima of the modified potential obtained by adding the effective mass term of the condensate from the Lagrangian in Equation (4.27).

$$V_{mod} = \frac{\lambda_\sigma}{4}\left(|\sigma_0|^2 - \eta_\sigma^2\right)^2 + (\partial_z\theta + eA_z)^2|\sigma_0|^2. \tag{4.63}$$

σ_0 will tend to the minima

$$\sigma_{0,\text{mod}\ \ \min}^2 \approx \eta_\sigma^2 - \frac{2}{\lambda_\sigma}(\partial_z\theta + eA_z)^2. \tag{4.64}$$

In the approximation for K in Equation (4.29) the value of σ_0 at its minimum was used, replacing this guess with Equation (4.64) and substituting in the current from Equation (4.35) yields

$$K_{mod} \approx \delta_\sigma^2 \left(\eta_\sigma^2 - \frac{2}{\lambda_\sigma} (\partial_z \theta + eA_z)^2 \right), \tag{4.65}$$

$$= \delta_\sigma^2 \left(\eta_\sigma^2 - \frac{2}{\lambda_\sigma} \left(\frac{j^z}{2Ke} \right)^2 \right) \tag{4.66}$$

which can be further simplified by replacing the original K by its approximation from Equation (4.29) $K \sim \frac{1}{\lambda_\sigma}$. K_{mod} then tends to 0 as the current approaches

$$j^z \to e\eta_\sigma \sqrt{\frac{2}{\lambda_\sigma}}, \tag{4.67}$$

which can be interpreted as a conservative guess for the maximum current.

This concludes the treatment of the electromagnetic properties of a superconducting string. The previous Sections first provided a proof for the superconductivity of the string by showing both the appearance of an indefinite current and the Meissner effect. The current Section continued the discussion by illustrating that superconducting cosmic strings can build up a current up to a maximum. The next Section will deviate from the theoretical discussion and show the numerical profiles of the superconducting string fields.

4.5 Numerical analysis

To conclude this Chapter, it will be shown that the numerics of this thesis, explained in Appendix B.1 are able to reproduce the condensate profiles for both a global superconducting and local superconducting string. While the global string was shown to be unstable on its own, it is still an interesting object since a network of them, which introduces a cutoff on the long range behaviour of the fields, could be plausable.

Global string By demanding a cylindrical ansatz [56]

$$\begin{cases} \phi &= f(r) e^{i\vartheta}, \\ \sigma &= g(r) \end{cases} \tag{4.68}$$

and plugging these into the equations of motion of Equations (4.19) and (4.20), with the gauge field $\tilde{A}^\mu$ set to 0, one finds the profiles shown in Figure 4.3. Note that no phase

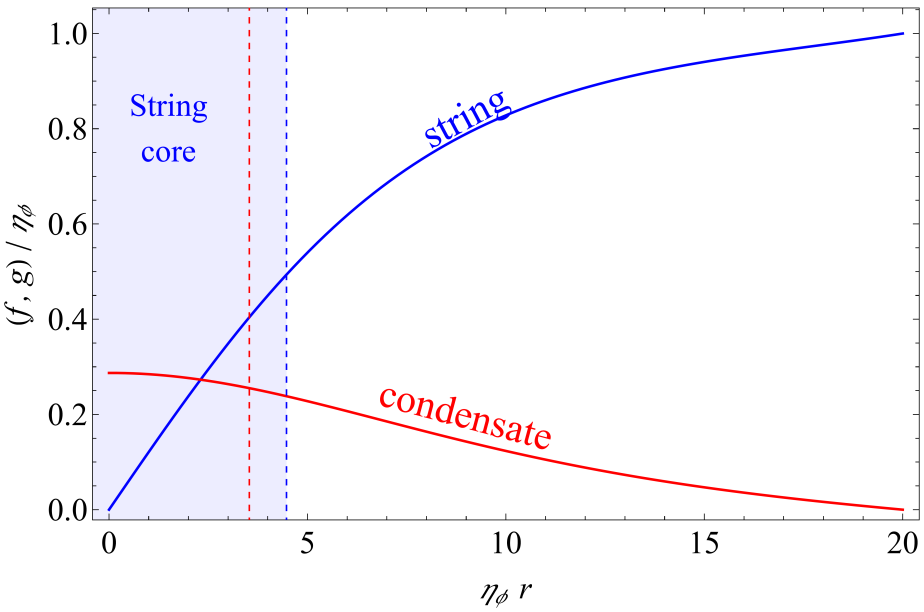

Figure 4.3: Plot showing the superconducting string field profiles using the parameterization of Equation (4.68). The dotted blue line denotes the string radius δ_ϕ, while the dotted red line denotes the condensate radius δ_σ. One can note that for values far away from the string the field ϕ returns to its vev, while the condensate σ goes to 0. All quantities are given in units of the ϕ field vev. The parameter values chosen satisfy all conditions previously derived (the vacuum condition (4.7), stability condition (4.13) and condensate condition (4.17)) $\lambda_\phi = 0.1$, $\eta_\phi = 1$, $\lambda_\sigma = 1$, $\eta_\sigma = 0.4$, $\beta = 0.1$ [11].

was demanded of σ since it was assumed that this phase acted as an excitation along the $z-$axis.

This illustrates the behaviour expected by the fields. When approaching the string, the field ϕ tends to 0 as described in Chapter 3. Due to this behaviour of ϕ, the system tends to the local minima in which the condensate field σ takes on nonzero values. This behaviour of the condensate is what breaks the $U(1)$ symmetry inside the string, allowing for Goldstone bosons to move across the z-axis and carry a current.

Local string The same procedure can be applied to a local string with a modified ansatz:

$$\begin{cases} \phi & = f(r)e^{i\vartheta}, \\ \tilde{A}_i(\vec{r}) & = -\epsilon_{ij}x^j \frac{n}{er^2}\alpha(r), \\ \sigma & = g(r). \end{cases} \tag{4.69}$$

Equations (4.19) and (4.20) can again be calculated with this ansatz and numerically

solved. The result can be seen in Figure 4.4.

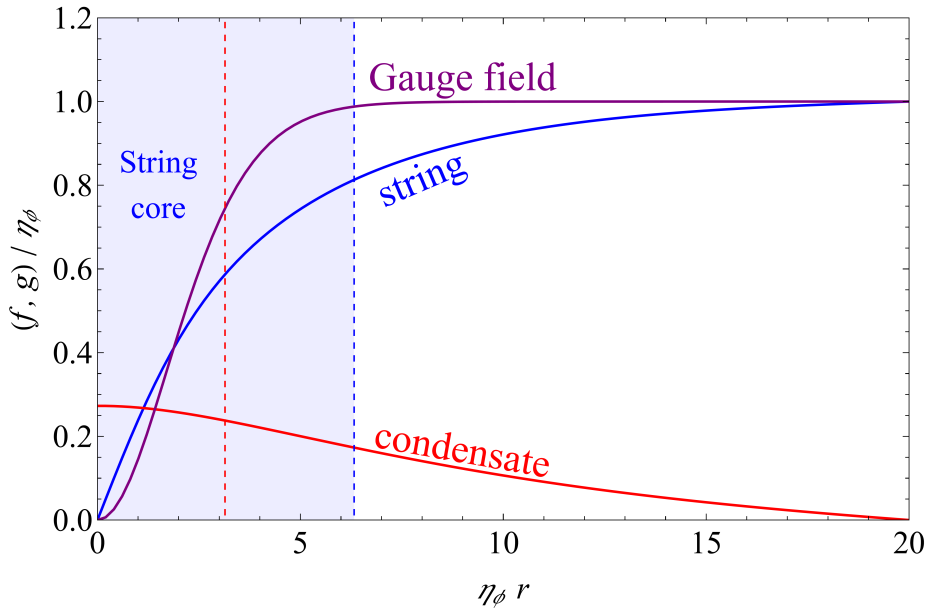

Figure 4.4: Profiles of the fields as defined by the ansatz in Equation (4.69). The dotted blue line denotes the string radius $\frac{1}{2}\delta_\phi$, while the dotted red line denotes the condensate radius $\frac{1}{2}\delta_\sigma$. Both the gauge field keeping the local string stable and the field ϕ evolve to their maximum at a distance far away from the string core. The condensate takes on a nonzero value in the string core. The parameters chosen agree with all conditions set before (the vacuum condition (4.7), stability condition (4.13) and condensate condition (4.17)) $\lambda_\phi = 0.05$, $\eta_\phi = 1$, $\lambda_\sigma = 1$, $\eta_\sigma = 0.45$, $\beta = 0.11$ and a gauge coupling for $\tilde{A}^\mu$ $g = 1$ [11]

The plot demonstrates the behaviour of the ϕ field as it would behave for a non conducting local sting, followed by its gauge field amplitude to compensate for the winding around the string, as discussed in Chapter 3. In Figure 4.4 we also see the expected behaviour for the profile of the field σ. Indeed the field σ take a nonzero value in the interior of the string, which is what leads to superconductivity for the $U(1)$ gauge field.

After starting from the simplest case of a global string defined by a single field, the numerical algorithm of this thesis solved a local string system, defined by a field ϕ and a gauge field $\tilde{A}^\mu$ by choosing an appropriate cylindrically symmetric ansatz. This chapter can now end by stating that the numerics can be applied to both a global superconducting string as to a local superconducting string.

In the coming chapters this logic will be applied to a new topological defect, domain walls. The same train of thought and structure of the previous chapters on cosmic and superconducting strings will be followed. The goal being to proof superconducting domain walls are possible and recreating the same profiles as shown in this Section.

5 Domain Walls

After introducing the concept of domain walls briefly in Chapter 2, a more thorough derivation is in order to properly discuss domain wall dynamics in the early Universe and the properties important when discussing them. This chapter aims to give a concise, but complete overview of all domain wall concepts. The ultimate goal is to apply superconductivity in the same way as Witten proposed for strings, as shown in Chapters 3 and 4. The first section utilises a new example to reintroduce thickness and tension. These concepts will then be used to illustrate the forces acting on domain walls in the early Universe. The place of domain walls in the ΛCDM model will be challenged, leading to the domain wall problem, after which a mechanism to solve this problem will be discussed. The chapter ends with a discussion of the gravitational wave signal of domain walls and how they are parameterised.

This chapter includes reviews of existing results. The numerical computations of the domain wall field profiles is an independent recreation of existing results.

5.1 Domain wall configuration

To start, recall the basic example given in Section 2.1.1 and Equation (2.3). The equation of motion for this real scalar field could be solved analytically, granted the correct ansatz is chosen. As demonstrated in the previous chapters, this thesis uses a numerical relaxation algorithm to solve equations of motion without an analytical solution. As another check that the algorithm behaves correctly and a reminder of the shape of the solution, Figure 5.1 illustrates both the analytical solution and the numerical solution to Equation (2.3).

To illustrate that domain walls are not confined to this single example and to reintroduce the concepts of thickness δ and tension σ, the Lagrangian

$$\mathcal{L} = -\frac{1}{2}\partial_\mu\phi\partial^\mu\phi - \frac{2\lambda\eta^4}{N^2}\left(1-\cos\left(\frac{N\phi}{\eta}\right)\right), \tag{5.1}$$

will be discussed. The solution to the equation of motion is again analytically solvable,

$$\phi = \eta\left(\frac{2\pi k}{N} + \frac{4}{N}\tan^{-1}(e^{\sqrt{2\lambda}\eta z})\right). \tag{5.2}$$

This shape is illustrated in Figure 5.2. One can observe that the field indeed interpolates continuously between two minima, similarly to the ϕ^4 example. The width was approximated as the prefactor of z in the analytical solution and used to shade an estimate of the domain walls dimensions. We can conclude from the figure that different models can lead to the same shape of domain wall, increasing their plausability.

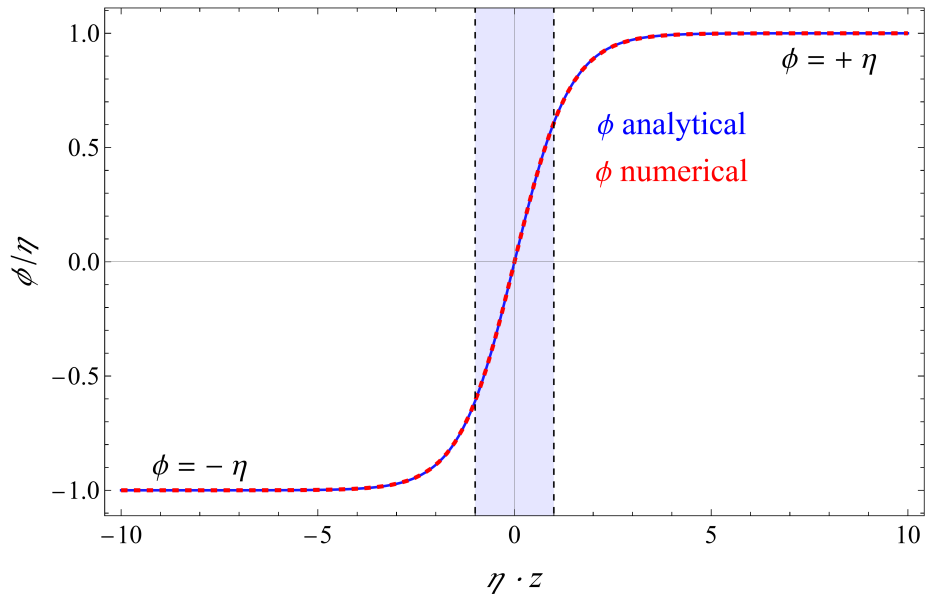

Figure 5.1: Plot comparing the analytical solution of Equation (2.3) in blue with the numerical result, plotted as a red dashed line. The field interpolates between the two minima at $\pm\eta$ by crossing the potential hill at $\phi = 0$. The region in which the crossing happens is denoted as a domain wall and is shaded in blue.

To reintroduce the tension, one can calculate the energy momentum tensor of the domain wall's Lagrangian via its definition. It yields a result similar to the ϕ^4 example and can be written as

$$T^{\mu}{}_{\nu} = \frac{\partial \mathcal{L}}{\partial(\partial_\mu \phi)} \partial_\nu \phi - g^{\mu}{}_{\nu} \mathcal{L} = \left(\frac{d\phi}{dz}\right)^2 \mathrm{diag}(1,1,1,0). \tag{5.3}$$

The energy density per unit area can be found by integrating over the direction perpendicular to the wall

$$\sigma = \int dz T^{00} = \frac{8\sqrt{2\lambda}\eta^3}{N^2} \tag{5.4}$$

The spatial components T^{11} and T^{22} can be integrated in the same way to find the stress acting in the x and y directions. The result yields the same quantity modulo a sign

$$-\sigma = \int dz T^{11} = \int dz T^{22}. \tag{5.5}$$

This last line also reveals the reason behind the name tension. $-\sigma$ is the stress exerted on the plane of the domain wall, like pulling on a sheet. This is an important

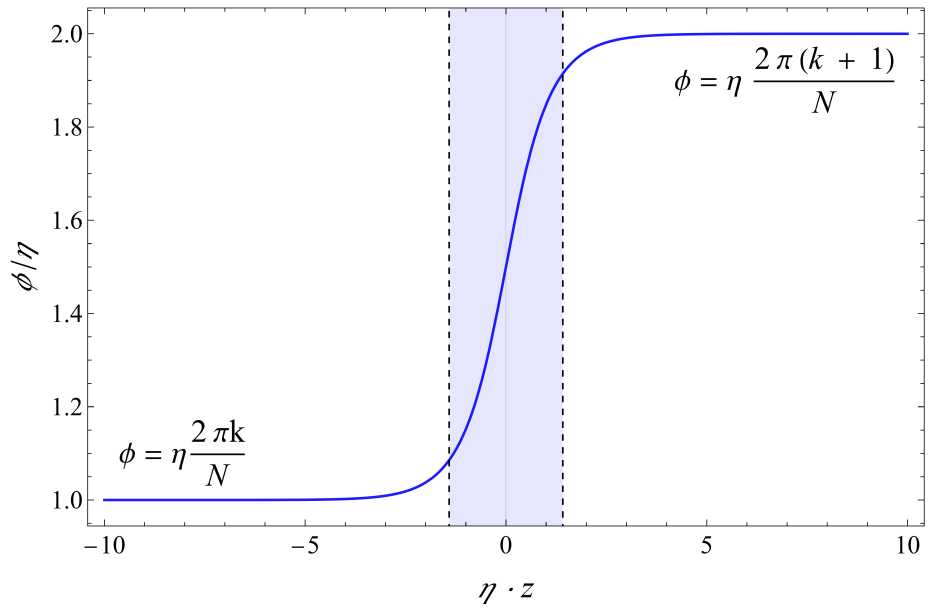

Figure 5.2: The solution to the equation of motion of Equation (5.1). The solution interpolates between the minima $\eta\frac{2\pi k}{N}$ and $\eta\frac{2\pi(k+1)}{N}$. Parameters $N = 2\pi$ and $k = 1$ were chosen. One can see that the field indeed interpolates between two minima . The width of the domain wall was approximated as the prefactor of the spatial coordinate z in the analytical solution of Equation (5.2). The domain wall is shaded in blue.

Lagrangian since it is quite common in certain axion models. The discussion of these models however, lies outside the scope of the thesis. The sole purpose of this example is to demonstrate that domain walls can be found in several different theories.

5.2 Domain walls in the early Universe

At this point, the concept and basic properties of a domain wall were demonstrated with two examples. To explain their place in the Universe, this section aims to provide further clarification on the life of domain walls throughout the Universe.

We will start with the formation mechanism briefly discussed at the end of Section 2.1.3. The Kibble mechanism [19] allows for the formation of domain walls in any second order phase transition which involves breaking a discrete symmetry, by stating that the field values were randomly determined by quantum fluctuations. These fluctuation tended to die out on a scale of the correlation length ξ since the ideal lowest energy state consists of a homogeneous field configuration. The correlation length corresponds to the distance beyond which the fluctuations are uncorrelated i.e. for distances greater than ξ the field fluctuations are random. A natural value for the correlation length can be determined by imposing causality. This yields the causal horizon as an upper bound. Beyond causal processes, we do not expect any correlation to occur.

This upper limit is very conservative and a better guess of the correlation length is possible when considering the specific phase transition [19]. To show this and to take a closer look at the exact field behaviour at the critical temperature transition $T \approx T_c$, one can again consider the ϕ^4 Lagrangian with temperature corrections [18]

$$\mathcal{L} = \frac{1}{2}\partial_\mu\phi\partial^\mu\phi - V(\phi, T) \tag{5.6}$$

with a potential

$$V(\phi, T) = \frac{\lambda}{4}(\phi^2 - \eta^2)^2 + \frac{\lambda}{12}T^2\phi^2. \tag{5.7}$$

As a reminder, the critical temperature was defined in Section 2.1.3 as the temperature between the unbroken $T > T_c$ and broken symmetry phase $T_c > T$. The critical temperature can be found be finding the temperature for which the minima at non-zero temperature are lower than the zero temperature minimum. The minima of the potential are found by setting the derivative to zero as

$$\partial_\phi V(\phi, T) = 0 \Rightarrow \left(\phi_0 = 0 \vee \phi_{min} = \pm\sqrt{\eta^2 - \frac{T^2}{6}}\right). \tag{5.8}$$

The potential values at the minima are calculated as

$$V(\phi_{\min}, T) = \frac{T^2}{12}\left(\eta^2 - \frac{1}{12}T^2\right) \quad \text{and} \quad V(\phi_0, T) = \frac{\lambda\eta^4}{4}. \tag{5.9}$$

By demanding that these are equal, the critical temperature is found to be

$$T_c = \sqrt{6}\eta. \tag{5.10}$$

In a Hot Big Bang model, once the Universe cools down to $T = \sqrt{6}\eta$, the field ϕ will begin selecting nonzero minima ϕ_{min}. The scale on which ϕ begins selecting these minima is determined by the effective mass of this potential. An infinitesimally small fluctuation $\delta\phi$ can be interpreted as a "particle" with effective mass. By neglecting all higher order terms one finds an expression for the Lagrangian of the form

$$\mathcal{L} \approx \frac{1}{2}\partial_\mu\delta\phi\partial^\mu\delta\phi + \frac{\lambda}{2}(\eta^2 - \frac{T^2}{6})\delta\phi^2. \tag{5.11}$$

The effective mass term of the fluctuation can be read off as

$$m_{eff}^2(T) = \lambda\eta^2(1 - \frac{T^2}{6\eta^2}). \tag{5.12}$$

Note that for $T = 0$, this is just the mass the scalar field obtains when applying the BEH mechanism. By interpreting this mass as a Compton wavelength, one can obtain a guess for the correlation length of the fluctuations[§]

$$\xi \sim \frac{1}{m_{eff}(T)}. \tag{5.13}$$

The goal of finding a more sufficient estimate of ξ is hereby completed. In essence this now gives a picture of the Universe at a certain temperature T. At orders larger than ξ, the field will select random values of minima and the Universe can be divided in volumes of ξ^3, each of which takes on a random *vev*.

In the current ϕ^4 example, this means volumes with either a positive or negative minimum. In the case of the cosine example given in the beginning of this section, N different values of minima exist and hence N different kinds of domains can form. When two such domains border and the space of minima is discrete ($\pi_0(\mathcal{M}) \neq 1$), the field has no choice but to leave its minima and interpolate continuously between the two domains. A domain wall has formed. In this way one can imagine the Universe as transversed by infinite or closed domain walls. The latter of which will collapse when their curve is closed inside of their Hubble volume. Closed domain walls that exceed the Hubble volume do not contract since their points closing the curve lay outside of each others' causal horizon.

One can study this simplified system of volumes and random minima by defining a grid of volumes. Each of these volumes can be assigned a random value for its minimum with a certain probability. This research is known as percolation theory and is useful in determining the physics of the formation of domain walls. Later in the thesis, this theory will be referred to, to set a bound on certain domain wall properties.

After forming these domains and the domain walls separating them, the Universe enters an era $T_c > T$. The question remains of how these domain walls will evolve as the temperature lowers further. The forces acting on the domain walls should first be identified. There are two that dominate the dynamics of the domain walls: tension and friction. The tension force was indirectly encountered before in Chapter 2.1. It is this force that forces closed domain walls to collapse. It can be modelled as a pressure [60]

$$p_T \sim \frac{\sigma}{R_{wall}}. \tag{5.14}$$

[§]In reality this correlation length should be calculated by looking at the correlation function of two points $\langle\phi(x)|\phi(y)\rangle$. For further information one can consult [59].

The bigger the area density σ of a domain wall, the stronger the force that acts upon it. R_{wall} represents the curvature radius of the wall. The flatter a wall, the less force acting upon it. Hence infinite domain walls with only a tension force acting upon it will be forced to flatten out.

The other force is the friction force. It arises due to the plasma content of the Universe interacting with the domain walls. It can be roughly estimated as the momenta of the particles colliding with the wall Δp times the number density n

$$p_F \sim \Delta p \, n \sim v T^4. \tag{5.15}$$

The momentum transfer is proportional to the speed of the domain wall v times the energy of the thermal bath i.e. the temperature T. The number density can be substituted as determined by statistical mechanics: $n \sim T^3$. The next section will provide a more elaborate description for the friction force. For now, this force will be neglected. This assumption can be justified by stating that the interactions with the plasma weaken at lower temperatures and hence at later times the plasma-temperature independent tension force becomes dominant. The regime in which one neglects friction is also called the scaling regime, since the tension force leads to an energy solution of the form (following the conventions of [60]):

$$\rho_{DW} = A\frac{\sigma}{t}. \tag{5.16}$$

A self-similar solution of this form was derived numerically in [61–68] and analytically in [69, 70]. σ is again the tension, divided only by the first power of time. From that, one can infer that the energy density of domain walls dilutes slowly. A is a constant called the area parameter. It was derived numerically in [68] as

$$A \approx 0.8 \pm 0.1. \tag{5.17}$$

With this "late time" behaviour of domain walls in hand, one can begin comparing this energy density with the other components of the Universe: matter, radiation and the cosmological constant, whose behaviour at their respective domination periods is determined by the Friedman equations [71],

$$\rho_{rad} \sim a(t)^{-4}, \tag{5.18}$$
$$\rho_{mat} \sim a(t)^{-3}, \tag{5.19}$$
$$\rho_{\Lambda} \sim \text{Cst.}, \tag{5.20}$$
$$\rho_{DW} \sim t^{-1} \sim a^{-2}. \tag{5.21}$$

$a(t)$ is the scale factor of the Universe. The final proportionality holds in the radiation dominated period, where $a(t) \sim t^{\frac{1}{2}}$. By stating that domain walls form in the early

Universe phase transitions, their occurrence in the radiation dominated period is a valid assumption [¶]. The Hot Big Bang model states a radiation dominated period in the early Universe, followed by a matter dominated period. The current epoch is still in this regime. The final period would be domination by the mysterious cosmological constant. [28].

Observing the energy density behaviours, it becomes clear a period would exist where the domain wall energy density would dominate. This is a serious problem for domain wall physics and hence the time will be taken to explain the problem qualitatively. A possible solution to this problem will be provided at the end of this Section.

The time at which this transition occurs can be estimated by stating a flat Universe, as approximately confirmed by experiments [72]. The total energy density in this regime is equal to the critical energy density. Calculating the critical density in the radiation dominated era yields

$$\rho \approx \rho_c = \frac{3H^2}{8\pi G} = \frac{3}{4}\frac{M_{pl}^2}{t^2}, \tag{5.22}$$

in which the Hubble parameter during radiation domination $H = 1/2t$ and the reduced Planck mass $M_{pl} \coloneqq \sqrt{\frac{1}{8\pi G}} \sim 10^{18}$ GeV were used to reparameterize the expression. The condition for the domain walls to dominate the energy density is $\rho_{DW} > \rho_c$. This transition occurs at $\rho_{DW} = \rho_c$ and yields a time [60]

$$t_{dom} = \frac{3}{4}\frac{AM_{pl}^2}{\sigma} \approx 2.93 \times 10^3 \text{sec} A^{-1} \left(\frac{\sigma}{\text{TeV}}\right)^{-1}. \tag{5.23}$$

The time at which domain walls begin dominating the Universe is inversely proportional to their surface energy density, as can be intuitively expected. A domain wall domination regime would lead to an expansion of the Universe $a(t) \sim t^2$, which contradicts modern cosmology [11]. If the domination time is yet to come, the Universe is still in a regime $\rho_{DW} < \rho_c$. One can estimate the energy density perturbations as observed today $t = t_0$ by comparing Equation (5.16) and (5.22) as [60]

$$\frac{\delta\rho_{DW}}{\rho_c} \approx \frac{4}{3}\frac{t_0^2}{M_{pl}^2}\rho_{DW} \approx \frac{4A}{3}\frac{\sigma}{M_{pl}^2}t_0 \sim 10^{12}\left(\frac{\sigma}{\text{TeV}^3}\right). \tag{5.24}$$

As shown in [73], to be compatible with cosmic microwave background (CMB) observations the tension should be bound from above. The temperature fluctuations of the CMB are of order $\frac{\delta T}{T} < 10^{-5}$ [74]. The energy density depends on temperature as $\rho \sim T^4$, hence the density perturbations should satisfy the condition $\frac{\delta\rho}{\rho} < 10^{-5}$. Substituting Equation (5.24) into this condition yields

[¶]The same reasoning in the matter domination period yields $\rho_{DW} \sim a^{-\frac{3}{2}}$.

$$\sigma^{\frac{1}{3}} < O(\text{MeV}). \tag{5.25}$$

This is a serious constraint, demanding that only "low" energy domain walls can exist in the current epoch. Keep in mind that this constraint is only valid for domain walls that never come to dominate the energy density of the Universe, hence a low energy per unit area is an expected result.

These properties describe the behaviour of domain walls as described in the Sections above. It will now be shown that a modification of the theory can omit the problem of domain wall domination. The idea of this modification is demanding that domain walls not satisfying Equation (5.25) disappear at a certain time $t < t_{dom}$.

To avoid domain wall domination, several solutions can be implemented in the theory. The two most popular are introducing either a population or potential bias. A population bias consists of introducing sufficiently strict initial conditions such that more domains in a certain minimum form. In other words a greater population of one type of minimum will dominate. Interested readers can be referred to [75] for a thorough discussion on population biases.

This thesis will instead focus on the second solution to avoid the initial condition selections, which corresponds to adding a bias term (a small tilt) in the potential. Specifically, by adding extra terms to the potential $V(\phi, T) = V_o + \Delta V$, one can favor a minimum. To illustrate this, we will again refer to the ϕ^4 model. The potential can be enhanced with a term

$$V(\phi, T) = \frac{\lambda}{4}(\phi^2 - \eta^2)^2 + \frac{\lambda}{12}T^2\phi^2 + C\eta(\frac{1}{3}\phi^2 - \eta^2)\phi. \tag{5.26}$$

This potential is sketched in Figure 5.3. One can observe that the discrete symmetry on which the theory was built is now explicitly broken. Therefore only small biases are considered for which there is still an approximate discrete symmetry present. This condition will be made more rigorous later in this section by introducing an upper bound on the bias using percolation theory. For now, we will continue the discussion on the bias.

One of the minima is no longer equivalent with the other. At the onset of the phase transition this difference is not yet obvious and domains will form as discussed before, given that the potential bias is small [76]. After the formation the domains will "realise" the minima are not equivalent and domains of the disadvantaged minimum will begin to collapse. The potential bias is defined as the potential difference between the two minima at $T = 0$,

$$V_{bias} = \frac{4C}{3}\eta^4. \tag{5.27}$$

This is indicated on Figure 5.3 as the gray arrow.

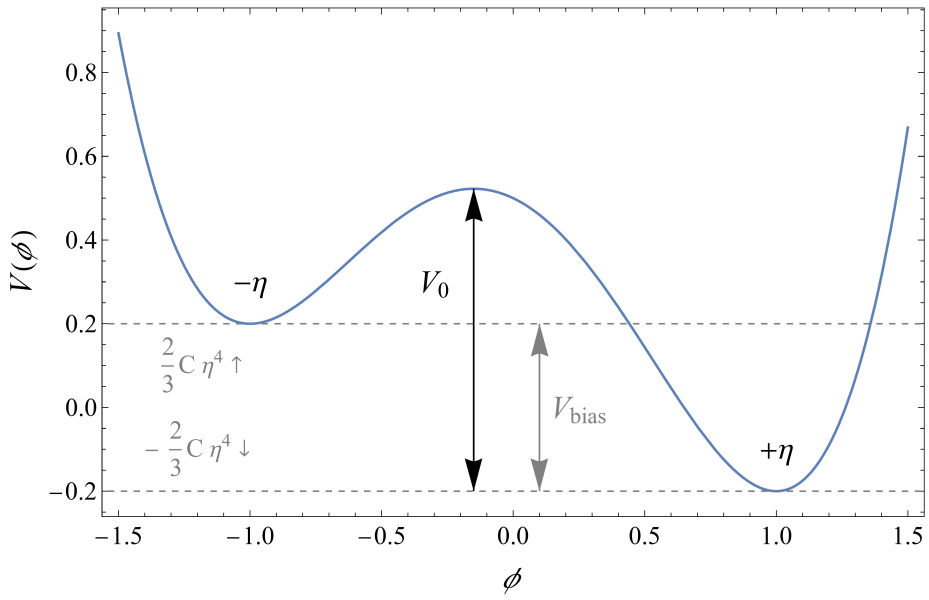

Figure 5.3: The modified potential with parameters $\lambda = 2$, $\eta = 1$ and $C = 0.3$ at temperature $T = 0$. The potential bias is indicated by the gray arrow. The height of the potential hill is indicated by the black arrow. One can observe that the two minima are still at $\phi = \pm\eta$, but their "weight" has changed. In this plot the true vacuum is at $\phi = +\eta$ and domains that take on the local minimum $\phi = -\eta$ will be suppressed.

By considering both the existence of DWs and the demand that their energy density does not exceed the critical density of the Universe, the bias can be bound both from above and from below.

The existence of DWs is not guaranteed since a huge bias would completely break the Z_2 symmetry and the whole reasoning behind the degenerate minima domains would collapse. To further elaborate on this, a new quantity has to be introduced. In explaining phase transitions in Section 2.1.3, it was stated that the field chooses different minima after passing the critical temperature T_c on a scale of the correlation length ξ. This was an oversimplification, since the effective potential was only modified by the lowest order of temperature corrections. This corresponds to the one loop correction mentioned in Section 2.1.3. Close to the critical temperature this criterion breaks down and one should only consider the formalism valid at temperatures far enough away from T_c.

Physically, close to the critical temperature, the temperature is sufficiently high to let the minima jump over the potential barrier at V_0. The temperature after which the previous first order corrections become valid is denoted as the Ginzburg temperature T_G. One can find this quantity by calculating the Helmholtz free energy needed for a domain to cross the potential barrier [11]. When the temperature of the system is similar to this energy, the system has enough thermal energy to make the field jump between minima. This can be parameterised as

$$T_G \approx F_{barrier} \approx V_0 \xi^3. \tag{5.28}$$

Note the factor ξ^3, which represents the domain volume. The height of the potential hill V_0 is indicated in Figure 5.3 as the black arrow.

The domain structure only becomes fixed after the temperature crosses the Ginzburg temperature $T_G > T$. Now to return to the reason for this aside. We were looking for an upper bound on the bias V_{bias}. The condition for a maximum bias is found by comparing the probabilities that a domain picks a certain minimum [76]. In the current example the choice is between $+\eta$ (p_+) and $-\eta$ (p_-). When the temperature passes the Ginzburg temperature the choice of minimum becomes fixed and one can approximate the system as in equilibrium. Applying Boltzmann's entropy formula [77] yields

$$\frac{p_-}{p_+} = \exp\left(-\frac{F_{bias}}{T_G}\right) \approx \exp\left(\frac{V_{bias}}{V_0}\right), \tag{5.29}$$

in which F_{bias} was derived in the same manner as the barrier energy of Equation 5.28. This expression connects the probabilities with the bias V_{bias}.

Turning back to percolation theory, the study of such a network of domains, one can calculate the minimal chance for which infinite domain walls will form. This minimal probability p_c is defined as the probability for a domain to take on the negatively biased minimum above which an infinite connection of such domains can form. In this case that means the probability for a domain to take on $-\eta$. The value of p_c can be found by numerically simulating networks of domains. This was done in [78] and yields a value for the critical probability $p_c = 0.311$ in the current ϕ^4 theory. Substituting this into Equation 5.29 and demanding that the probability to pick a negative minimum is greater than the critical probability $p_c < p_-$ yields

$$\frac{V_{bias}}{V_0} < (\ln\left(\frac{1-p_c}{p_c}\right) = 0.795), \tag{5.30}$$

in which p_+ was rewritten as $p_+ = 1 - p_-$. The goal of finding an upper bound on the bias is now fulfilled. If V_{bias} satisfies this condition, a network of domain walls will form. One can interpret this bound as the maximum value below which the system still approximately exhibits a discrete symmetry.

As time goes on the pressure due to the bias will push the $-\eta$ domains closed and eliminate the domain wall network, thus solving the energy domination problem if this occurs before the radiation energy density can decay below ρ_{DW}. This can be translated in a lower bound for V_{bias}.

While the upper bound is a condition for the formation of domain walls to occur, the lower bound is a condition for them to disappear at a sufficiently early time before they

begin dominating the energy of the Universe. To find the annihilation time of biased domain walls one has to model the force pushing on the false vacuum domains as [79]

$$p_V \sim V_{bias}, \tag{5.31}$$

where p_V is called the volume pressure force. A greater bias will result in a bigger energy difference between the minima and hence the pressure to assume the true vacuum will increase.

Since friction was neglected at the beginning of this section, only two forces act on the domain wall network. The pressure due to tension p_T aims to flatten the domain walls, while the pressure due to the bias aims to close the false vacua and hence tries to curve the domain walls closed. When the bias pressure dominates the domain walls will begin closing the false vacuum domains. The time at which the domain wall network transitions from tension pressure domination to volume pressure domination can be found by considering when the bias pressure becomes equal to the tension pressure $p_T = p_V$. Substituting their previously derived expressions (Equations (5.14) and (5.31)) into this condition yields

$$\frac{\sigma}{R_{DW}} = V_{bias}, \tag{5.32}$$

in which R_{DW} is again the curvature radius of the domain wall. Physically one can think of $(V_{bias} \cdot R_{DW})$ as the potential lowering of the energy per unit area. When $\sigma > (V_{bias} R_{DW})$ the system would have to move an energy area density that is larger than the difference in energy it could lose when the domain is finally closed. When $\sigma < (V_{bias} R_{DW})$ the energy to be lost when closing a domain is worth the moving of energy area density σ.

One can now substitute R_{DW} by considering the domain walls to be in the scaling regime before this transition. The curvature scales as $R_{DW} = \frac{t}{A}$, which can be seen in Equation (5.16). This substitution yields

$$t_{ann} = C_{ann} \frac{A\sigma}{V_{bias}}. \tag{5.33}$$

t_{ann} is called the annihilation time and is defined as the time at which the false vacua domains close and the domain walls annihilate. The dimensionless constant C_{ann} was implemented to allow for numerically fixing the value t_{ann} to a greater precision. The value for this constant is numerically found to be in the range [80]

$$C_{ann} \approx 2 - 5, \tag{5.34}$$

depending on the number of discrete vacua in a Z_N theory. This thesis assumes a value $C_{ann} = 2$.

With this time expression in hand the lower bound for V_{bias} is found by demanding that the domain walls disappear before getting the opportunity to start dominating $t_{ann} < t_{dom}$. Combining Equation (5.23) and Equation (5.33) yields a constraint on V_{bias}

$$V_{bias}^{\frac{1}{4}} > 2.18 \times 10^{-5} \text{GeV} C_{ann}^{\frac{1}{4}} A^{\frac{1}{2}} \left(\frac{\sigma}{\text{TeV}^3} \right)^{\frac{1}{2}}. \tag{5.35}$$

Physically, when the bias is too small the system realises too late that the two vacua are not equivalent and the domain wall energy density begins to dominate before the bias pressure has a chance to close the false vacua domains.

Customary, the temperature of the Universe at which the domain walls annihilate T_{ann} is used as a parameter, replacing V_{bias}. To connect the bias to a temperature, one assumes radiation domination and compares the Hubble parameter's time behaviour

$$H = \frac{1}{2t} \tag{5.36}$$

with its expression derived from the distribution function of the cosmic plasma [71]

$$H = \frac{\pi}{3} \left(\frac{g_*}{10} \right)^{\frac{1}{2}} \frac{T^2}{M_{Pl}}, \tag{5.37}$$

in which M_{Pl} again denotes the reduced Planck mass and g_* is the effective number of degrees of freedom of the cosmic plasma. Setting these two expressions equal to one another yields an expression for the temperature in function of time

$$T = \sqrt{\frac{3}{2}} \sqrt{\frac{M_{Pl}}{\pi}} \left(\frac{g_*}{10} \right)^{-\frac{1}{4}} \frac{1}{\sqrt{t}}. \tag{5.38}$$

Plugging in the expression for t_{ann} of Equation (5.33) yields [60]

$$T_{ann} = 3.41 \times 10^{-2} \text{ GeV } C_{ann}^{-\frac{1}{2}} A^{-\frac{1}{2}} \left(\frac{g_*(T_{ann})}{10} \right)^{-\frac{1}{4}} \left(\frac{\sigma}{\text{TeV}^3} \right)^{-\frac{1}{2}} \left(\frac{V_{bias}}{\text{MeV}^4} \right)^{\frac{1}{2}}. \tag{5.39}$$

One can see that the annihilation temperature increases with the bias. This can be interpreted as a bigger bias exerting a larger force to close the false vacuum domains. Hence annihilation happens at an earlier time and a higher temperature.

Both constraints in Equations (5.30) and (5.35) can be rewritten as a condition on the annihilation temperature T_{ann} in function of the wall tension σ.

Upper bound:

$$T_{ann} < 3.04 \times 10^4 \text{ GeV } C_{ann}^{-\frac{1}{2}} A^{-\frac{1}{2}} \left(\frac{g_*(T_{ann})}{10}\right)^{-\frac{1}{4}} \left(\frac{\sigma^{\frac{1}{3}}}{\text{GeV}}\right)^{-\frac{3}{2}} \left(\frac{V_0}{\text{GeV}^4}\right)^{\frac{1}{2}}, \tag{5.40}$$

Lower bound:

$$T_{ann} > 1.62 \times 10^{-5} \text{ GeV } C_{ann}^{\frac{1}{4}} A^{\frac{1}{2}} \left(\frac{g_*(T_{ann})}{10}\right)^{-\frac{1}{4}} \left(\frac{\sigma}{\text{TeV}^3}\right)^{\frac{1}{2}}. \tag{5.41}$$

Given that these bounds are satisfied, this modified model allows for a population of domain walls in the early Universe in a period $T_c > T > T_{ann}$.

We have now solved the domain wall domination problem by introducing a bias on the potential. By demanding that the bias is small enough to still allow for domain wall formation and big enough to solve the domination problem, both an upper and lower bound were found on the bias. By switching parameters, the bounds were expressed in terms of the temperature at which the domain walls annihilate.

The next part of the thesis will focus on the friction force. After which the Chapter will end with discussing the domain wall gravitational wave signal.

5.3 Friction

The previous section neglected the friction pressure p_F in favor of the scaling regime, dominated by the tension pressure p_T. This section aims to go deeper on the subject of friction. The balance between friction and tension will be discussed, as well as showing at what times friction dominates domain wall dynamics. The usual example of the ϕ^4 model will serve to illustrate friction calculations and which parameters come into play. Most of this sections arguments and calculations follow [81].

One can model the friction pressure on the domain wall by computing its equations of motion in the thin wall approximation. This approximation considers the domain wall as a two dimensional object. By adding an appropriate force term the friction pressure can be included and a general formula for the pressure can be found. As an aside when discussing pressure, we refer to the pressure due to friction. The details of these calculations are given in Appendix C. The pressure on a domain wall is calculated in [81] and takes the following form

$$\Delta P = v \frac{g}{\pi^2} \int_0^\infty dp_z p_z^3 \mathcal{R}(p_z) \exp\left(-\frac{\sqrt{m^2 + p_z^2}}{T}\right). \tag{5.42}$$

The quantity p_z over which is integrated is the momentum of incoming particles, m is the mass of the interacting particles in a thermal bath T. v is the velocity of the domain wall on which the particles exert their momenta. The quantity $\mathcal{R}(p_z)$ is the probability

that a particle with momentum p_z interacts with the domain wall. The exponential is the Boltzmann distribution of the particles. When multiplied by the probability $\mathcal{R}$, this gives a distribution of particles that scatter on the domain wall. The p_z^3 factor is due to integrating the momentum p_z over the three-sphere with radius p_z in momentum space $d^3p_z \sim p_z^2 dp_z$. This pressure can now be used to quantify a regime in which the friction pressure dominates.

To quantify an exact condition for when friction will be taken into account, one can look back at the equations of motion with a friction force implemented. The conclusion is that friction can be offset by the Hubble parameter. In other words, if the Universe expands rapidly enough, particles and domain walls do not interact frequently enough to have an effect on the domain wall dynamics. This is similar to how particle species freeze-out after their interaction rates become smaller than the Hubble constant. The condition can be written as [81]

$$3H \lesssim \frac{1}{l_f}, \tag{5.43}$$

in which l_f is called the friction length. One can interpret this friction length l_f as a sort of mean interaction length of particles and DWs. The exact form of this quantity depends on the momentum of the plasma interacting with the domain wall and hence the pressure it exerts.

As we showed in Equation (5.42), the pressure force ΔP can be computed by considering particles scattering off the the domain walls. This scattering depends on the reflection coefficient R. The pressure determines the friction length through the relation

$$\frac{1}{l_f} \approx \frac{\Delta P}{\sigma v}. \tag{5.44}$$

One can see that a higher pressure due to particles in the cosmic plasma results in a lower mean interaction length, as can be expected.

This formalism is important, since it will allow for determining when either friction or tension dominate a certain domain wall model. As an example consider the familiar ϕ^4 example, interacting with another scalar field χ with a term

$$\mathcal{L}_{int} = -\frac{1}{2}\tilde{\lambda}\phi^2\chi^2. \tag{5.45}$$

The first step is finding the probability of interaction R, interpreted as the reflection coefficient. The problem hence reduces to a scattering problem. By assuming the wall to be perpendicular to the $z-$ axis and treating χ as an incoming wave in a scattering problem, a plane wave ansatz is justified

$$\chi = \chi(z)\exp\left(i(-\omega t + k_x x + k_y y)\right). \tag{5.46}$$

Using this ansatz on the ϕ^4 Lagrangian given in Equation (2.3) supplemented by the interaction term of Equation (5.45) and calculating the equations of motion yields an expression for the amplitude $\chi(z)$.

$$\chi(z)'' + k_z^2\chi(z) - \tilde{\lambda}(\phi^2(z) - \eta^2)\chi = 0. \tag{5.47}$$

The parameter k_z incorporates all information within the wave parameters as $k_z^2 = \omega^2 - k_x^2 - k_y^2 - m_\chi^2$. m_χ^2 is the rest mass of χ. It allows for writing $(\phi^2 - \eta^2)$ since $m_\chi^2 = \tilde{\lambda}\eta^2$, when the only contribution is the interaction with ϕ. This equation can be interpreted as a Schrödinger equation with potential $U(z) = \tilde{\lambda}(\phi^2(z) - \eta^2)$. The domain wall solution originally found in Equation 2.7 can be substituted and leaves a potential:

$$U(z) = -\tilde{\lambda}\eta^2 \operatorname{sech}\left(\sqrt{\frac{\lambda}{2}}\eta z\right). \tag{5.48}$$

This potential is known as a Pöschl-Teller potential. It is one of the few potentials for which an exact solution to the Schrödinger equation can be found. This calculation was performed in [82]. It eventually yields a reflection coefficient

$$R = \frac{\cos^2\beta}{\sinh^2\alpha + \cos^2\beta}. \tag{5.49}$$

With the variables β and α defined as

$$\beta = \frac{\pi}{2}\left(1 + \frac{8\tilde{\lambda}}{\lambda}\right)^{\frac{1}{2}} \quad \alpha = \left(\frac{2}{\lambda}\right)^{\frac{1}{2}}\frac{\pi k_z}{\eta}. \tag{5.50}$$

The shape of the reflection probability can be observed in Figure 5.4. One can conclude that lower wavenumbers i.e. lower energies interact with the domain walls and bounce off, while higher wavenumbers pass through.

The integral describing ΔP cannot simply be solved analytically and requires a numerical calculation. These precise quantities will be calculated for a superconducting domain wall interacting with photons in the next chapter.

5.4 Domain walls and gravitational waves

Gravitational waves were already introduced in Section (2.2). Now that a substantial amount of time was spent on describing domain wall configurations and dynamics, this thesis is ready to link the two concepts together. Since domain walls constitute a substantial energy density moving across the Universe, a GW signal can be expected to be measured. While the exact shape of the spectrum has to be simulated, an analytical

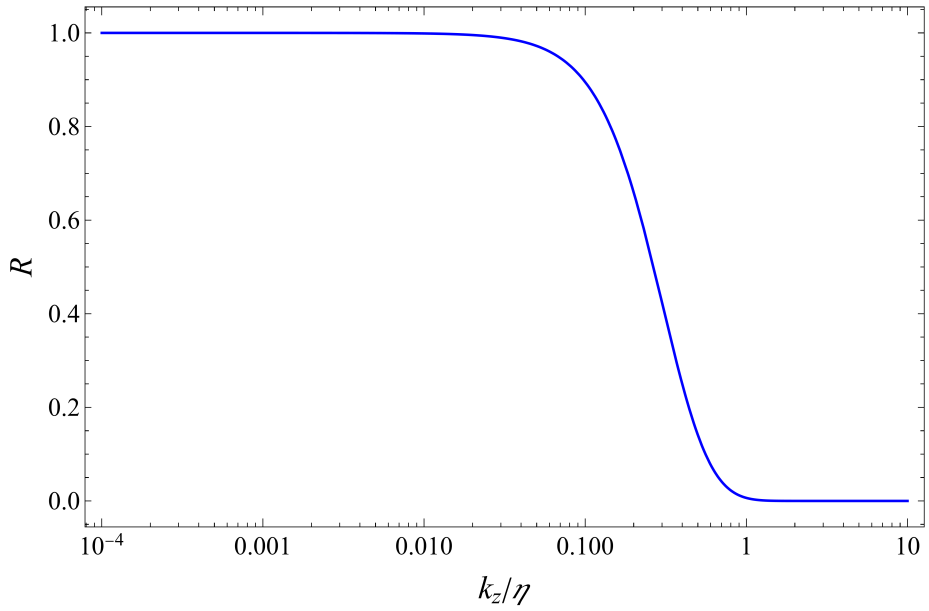

Figure 5.4: The shape of the reflection coefficient R from Equation (5.49) for parameters $\lambda = 2$, $\tilde{\lambda} = 1$. The horizontal axis was rescaled by η to obtain a dimensionless quantity.

approximation is available in the scaling regime by applying Equation 2.25. To apply this the quadrupole moment of a domain wall should be calculated. Equation (5.16) implies that the curvature of a domain wall scales as $R_{DW} \sim t$. This can be applied to the quadrupole formula as

$$Q_{ij} \coloneqq \int d^3x \rho_{DW} x_i x_j \approx M_{DW} t^2, \tag{5.51}$$

in which the coordinate scales under the integral were approximated as $x_i \sim R \sim t$.

The energy density of a domain wall in the scaling regime is given by Equation (5.16). Multiplying this with the typical volume of the problem t^3, yields an expression for the mass, $M_{DW} \sim A\sigma t^2$. The power defined in Equation (2.25) can hence be written in terms of the domain wall properties as

$$P \sim G \frac{M_{DW}^2}{t^2} = GA^2\sigma^2 t^2. \tag{5.52}$$

One can note that the power carried by gravitational waves emitted by domain walls depends on the tension of the domain walls, as expected. The dependency on time can be thought of as the time it takes for the domain walls to get to a scale H^{-1}. The greater the time, the greater the scale becomes and hence the greater the quadrupole moment is.

Since power is energy per time unit, this approximation leads to an expression for the energy density carried by GWs produced by a domain wall with tension σ on a timescale t.

$$\rho_{GW} \sim GA^2\sigma^2. \tag{5.53}$$

The tension carried by domain walls directly influences the energy emitted in their gravitational waves.

The discussion on gravitational waves emitted by domain walls was filled with approximations. To obtain exact results one has to refer to numerics. These numerics involve modeling a 3D cubic lattice with periodic boundary conditions (periodic as to mimic an infinite Universe) and the scalar field ϕ as the source of gravitational waves. One can build the equations of motion of the scalar field ϕ in the ϕ^4 theory with a Friedman-Robertson-Walker background and compute the energy density of emitted gravitational waves by ways of the energy-momentum tensor of the field ϕ. This work was performed in [68, 83, 84].

As an aside, these works have shown that domain walls can indeed be described by the scaling regime of Equation (5.16) at late times. The bias V_{bias} was also included in [83], allowing the simulations to confirm the annihilation time estimated in Equation (5.33).

The results of [68] are shown in Figure 5.5 in the form of a spectrum $S_k(t)$, defined as the energy density per logarithmic wave number, as explained in Section 2.2.1. In other words this denotes energy density per logarithmic frequency. The specifics of the calculation of this quantity can be consulted in [85]. The spectrum's definition is noted as

$$S_k(t) = \frac{2\pi^2\, V\, a^4(t)}{G} \frac{d\,\rho_{GW}}{d\,\ln k}(t), \tag{5.54}$$

in which V denotes the comoving volume of the calculations, $a(t)$ is the scale factor and G is Newton's constant. It is of importance to note that the wavenumber k is the comoving wavenumber. The factor $a^4(t)$ cancels the dilution of the energy density ρ_{GW} (since radiation scales as a^{-4}). This is a consequence of using comoving coordinates. The time t is defined as the time at which the domain wall emits their gravitational waves.

The spectrum found in such a way allows for approximating spectra analytically with a step formula by observing the shape of the numerical spectrum. The resulting spectrum can be parameterised as [68, 86]

$$S_k(t) \sim \begin{cases} k^3 & k < k_{peak} \\ k^{-1} & k_{peak} < k \end{cases}. \tag{5.55}$$

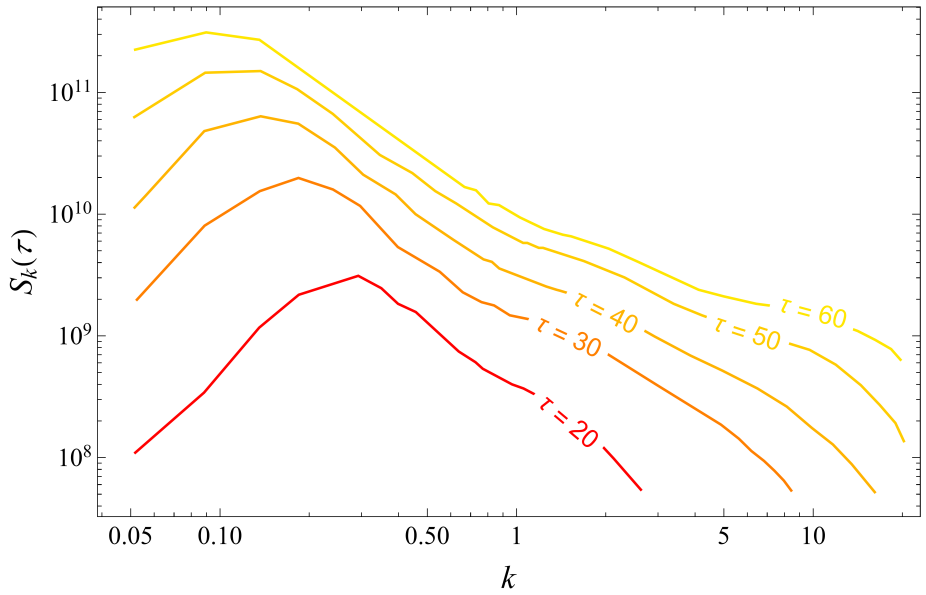

Figure 5.5: Figure taken from [68], The energy density per logarithmic unit wavenumber is shown in function of the comoving wavenumber k for different values of conformal times τ. All dimensionful variables are scaled in units of the *vev* $\eta = 1$.

The peak of the spectrum marks the transition between sub- and superhorizon wavelengths i.e. $k_{peak} \sim a\,H$. A typical domain wall is of scale H (domain walls of a smaller scale collapse soon after their formation) confirming the position of the peak. This leads to different behaviour for small $k < k_{peak}$ and large $k > k_{peak}$ values of the comoving wavenumber. A small value for k correspond with long wavelengths. For wavelengths sufficiently large i.e. greater than the spatial variations of the domain wall, the gravitational wave's spectrum behaviour is determined only by causality and scales as $S_k \sim k^3$ [‖] [86, 87].

One can now introduce a quantity to estimate the "correctness" of the approximations, called an efficiency parameter [88]. While a quantity like $\rho_{DW\,\mathrm{num}}/\rho_{DW\,\mathrm{approx}}$, seems like a good candidate, [68] pointed out that it contains systematic uncertainties when computing $\rho_{DW\,\mathrm{num}}$ by integrating the spectrum S_k. It is therefore more accurate to define an efficiency parameter with respect to a differentiation over k. Since the approximation in Equation (5.16) is independent of the wavenumber, this reduces to an expression

[‖] The power spectrum of the source term associated to super-horizon modes is flat, as this reflects the absence of causal correlations. One can then evaluate the Einstein equations to obtain how the perturbation h is connected to the source. This leads to the k^3 behaviour [87].

$$\tilde{\epsilon}_{GW} = \left(\frac{d\rho_{GW}}{d\ln k} \right)_{peak} \frac{1}{GA^2\sigma^2}, \tag{5.56}$$

in which the derivative at the peak was chosen to ensure $\tilde{\epsilon}_{GW}$ is a constant in the scaling regime. The numerical simulations yield a value for this parameter

$$\tilde{\epsilon}_{GW} \approx 0.7 \pm 0.4. \tag{5.57}$$

This value indicates that the approximation of the energy density in a scaling regime is in the correct order of magnitude. To keep track of this approximation one can keep the parameter $\tilde{\epsilon}$ as a factor in the approximated formula.

We can now turn back to the spectra of gravitational waves emitted by domain walls as defined in Equation (2.29).

$$\Omega_{GW}(t, f) = \frac{1}{\rho_c} \frac{d\rho_{GW}(t)}{d\ln f}, \tag{5.58}$$

which is the energy density per logarithmic frequency, in function of the critical density of the Universe. The link between the two expressions for the spectra can be made by considering the comoving wavenumber k in function of the frequency f

$$f = \frac{k}{2\pi a(t)}. \tag{5.59}$$

Note that the frequency now represents the physical frequency at a time t.

The gravitational wave spectrum given in Equation (5.58) can now be expressed in terms of frequency as shown in Equation (5.59) from the simulation results in Equation (5.55). The spectrum will increase as f^3 for frequencies $f < H$, reach a peak amplitude with associated peak frequency $f_{peak} = H$ and then decrease as f^{-1} for $f > H$. The peak amplitude Ω_{peak} can be deduced from the efficiency parameter $\tilde{\epsilon}_{GW}$ in Equation (5.56), which gives

$$\Omega_{GW}(t_{ann})_{peak} = \frac{8\pi\tilde{\epsilon}_{GW} G^2 A^2 \sigma^2}{3H^2(t_{ann})}, \tag{5.60}$$

in which the critical density was written in function of the Hubble parameter $\rho_c(t) = 3H^2(t)/8\pi G$. The peak was evaluated at the annihilation time t_{ann}, since the biased solution assumes that domain walls disappear at $t = t_{ann}$. The amplitude of the spectrum peak hence depends on the energy contained in a domain wall, parameterised as

its tension σ and the time at which domain walls annihilate. Since in a radiation dominated Universe $H \sim t^{-1}$, one can conclude that both the tension and annihilation time increase the GW amplitude, as could be intuitively expected.

After the domain wall annihilation, Ω_{GW} will decay as radiation up to the current epoch t_0. A rescaling of the values to $t = t_0$ yields

$$\Omega_{GW}(t_0)_{peak} = \frac{\rho_c(t_{ann})}{\rho_c(t_0)} \left(\frac{a(t_{ann})}{a(t_0)} \right)^4 \Omega_{GW}(t_{ann})_{peak}, \tag{5.61}$$

in which the first factor accounts for the change in critical density of the Universe up to the current epoch. Rewriting the critical density factor as

$$\frac{\rho_c(t_{ann})}{\rho_c(t_0)} = \frac{\rho_{rad}(t_0)}{\rho_c(t_0)} \frac{\rho_c(t_{ann})}{\rho_{rad}(t_0)} = \Omega_{rad}(t_0) \frac{\rho_c(t_{ann})}{\rho_{rad}(t_0)} \tag{5.62}$$

and using the cosmological formula [71]

$$\rho_{rad}(t) = \frac{\pi^2}{30} g_*(T) T^4 \quad \text{and} \quad T \sim g_{*,s}^{-1/3} a^{-1}, \tag{5.63}$$

in which g_* and g_{*s} are the effective degrees of freedom contributing to the energy density and entropy respectively, yields a result for the peak of the GW spectrum that can be written as

$$\Omega_{GW}(t_0)_{peak} = \Omega_{rad}(t_0) \left(\frac{g_*(T_{ann})}{g_*(T_0)} \right) \left(\frac{g_{*s}(T_0)}{g_{*s}(T_{ann})} \right)^{\frac{4}{3}} \Omega_{GW}(t_{ann})_{peak}. \tag{5.64}$$

This formula allows for shifting the time of the spectrum from the current epoch t_0 to the time of annihilation t_{ann} by use of well measured quantities .

Equation (5.64) can be rewritten in function of annihilation temperature T_{ann}, by using $H^2 = \frac{8\pi}{3}\rho$ and substituting Equation (5.63). Combining this with Equation (5.60) and Equation (5.64) and plugging in the known values today, $g_*(T_0) = 3.36$, $g_{*s} = 3.91$ [71] yields

$$\Omega_{GW} h^2(t_0)_{peak} = 7.2 \times 10^{-18} \tilde{\epsilon}_{GW} A^2 \left(\frac{g_{*s}(T_{ann})}{10} \right)^{-\frac{4}{3}} \left(\frac{\sigma}{\text{TeV}^3} \right)^2 \left(\frac{T_{ann}}{10^{-2}\text{GeV}} \right)^{-4}, \tag{5.65}$$

in which $h(t_0) = \frac{H_0}{100} \frac{\text{km}}{\text{sec}} \frac{1}{\text{Mpc}} = 0.67$ is the reduced Hubble constant. Quantities like $\Omega_{rad}(t_0)$ were substituted in accordance with the values given in [60]. This is the final expression for the peak of the spectrum. A large peak corresponds with a high DW

tension and low annihilation temperature i.e. heavy and long lived domain walls.

The peak of the spectrum f_{peak} can also be approximated. Since $f \sim k$ the only adjustment from the peak location of S_k at $k \sim H$ is due to the chosen frequency no longer being comoving i.e. the spectrum gets redshifted. These considerations allow for writing f_{peak} as

$$f_{peak} = \left(\frac{a(t_{ann})}{a(t_0)}\right) H(t_{ann}). \tag{5.66}$$

By again applying the cosmological identities in Equation (5.63) one obtains an expression

$$f_{peak} = 1.1 \times 10^{-9}\text{Hz} \left(\frac{g_*(T_{ann})}{10}\right)^{\frac{1}{2}} \left(\frac{g_{*s}(T_{ann})}{10}\right)^{-\frac{1}{3}} \left(\frac{T_{ann}}{10^{-2}\text{GeV}}\right). \tag{5.67}$$

Note that the frequency location of the peak does not depend on the tension, only on the lifetime of a domain wall. This can be interpreted as the peak only depending on the dimensions of a domain wall. Since a domain wall is of scale H^{-1}, this scale grows with the expansion of the Universe. Hence the shifting of the peak to lower frequencies (and longer wavelengths) at later times and lower temperatures.

By adapting the peak values and the numerical behaviour of the spectrum as given in Equation (5.55), translated to frequencies, a good approximation of the real spectrum can be constructed. As an example an approximated spectrum can be seen in Figure 5.6. In this figure the sensitivity curves of the Laser Interferometer Space Antenna (LISA) and the Einstein telescope (ET) are included. On can observe that for a well chosen range of parameters, these experiments are able to detect domain walls in the early Universe.

In conclusion, this chapter introduced the concept of domain walls after encountering them in Chapter 2. It was shown that domain walls can exists in several different models, after which properties such as their tension and width were approximated. The formation of domain walls in the early Universe was discussed together with the scaling regime before encountering the domain wall domination problem. By introducing a bias on the ϕ^4 potential, this problem was solved by letting domain walls annihilate at a certain time t_{ann}.

The conditions for formation and annihilation were applied to the domain wall properties, yielding bounds on the annihilation time in function of the domain wall tension. After exploring another domain wall regime, called the friction regime, the emission of gravitational waves was considered and the spectra of the domain walls were approximated.

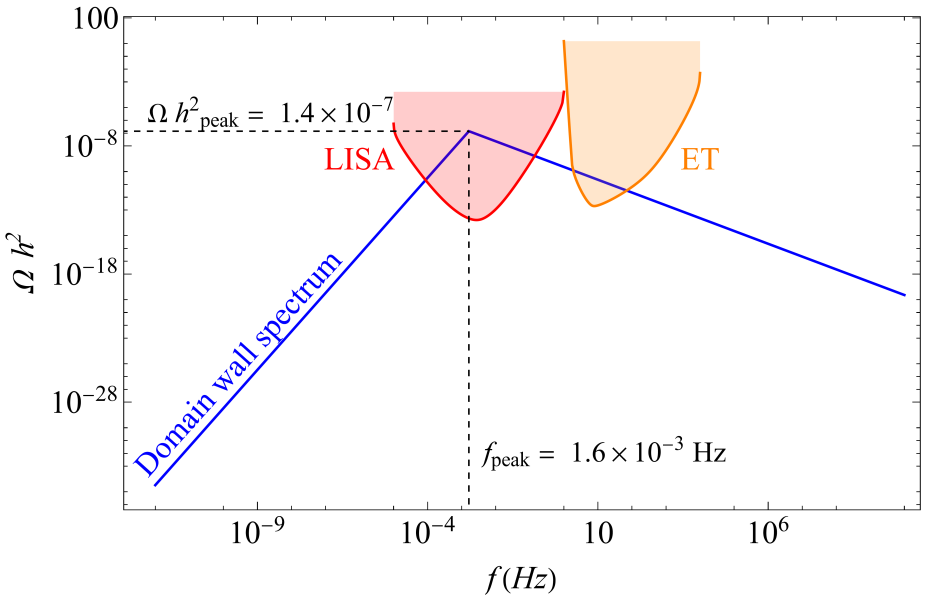

Figure 5.6: A gravitational wave spectrum emitted by a domain wall with tension $\sigma = 10^8$ GeV and annihilation temperature $T_{ann} = 10^4$ GeV. The sensitivity curves of the Laser Interferometer Space Antenna (LISA) and the Einstein telescope (ET) are included to illustrate to what types of domain wales these esperiments will be sensitive.

This concludes the chapter on domain walls. We are now ready to apply superconductivity on domain walls in a similar manner to its application to strings. This will be discussed in the next chapter.

6 Superconducting domain walls

Like superconducting strings, the field ϕ which constitutes the domain wall can be coupled to a new complex gauged field σ, leading to possibly interesting solutions. Depending on the parameters, this new field can take on a zero vacuum expectation value everywhere, without affecting the domain wall profile of ϕ. However, a more interesting case of course is when the parameters imply a new non-trivial solution where the new field σ takes a non vanishing expectation value in the interior of the domain wall.

This chapter aims to build this theoretical model, providing a perturbation analysis which, when exactly solved, proves that there exists a parameter space for which this non-trivial σ profile is the lowest energy solution to which the system tends. This will be complemented by a numerical relaxation analysis, showing the parameter space in which nonzero condensates can form. The numerical algorithm will solve the equations of motion (eom), yielding a domain wall solution for the field ϕ and a condensate profile for the field σ.

After computing the field profiles, the superconducting properties of this field configuration will be explored. This will be followed by calculating the reflection coefficient of photons and superconducting domain walls, which can be used in the next chapter to determine the friction forces acting upon a superconducting domain wall in the early Universe.

This chapter builds the field theory using an existing result. The stability analysis is a recreation of existing results. Proving the superconductivity and calculating the reflection coefficients are original work.

6.1 Superconducting domain wall configuration

We start this investigation by considering the Lagrangian studied in [89], which includes two real scalar fields. The field ϕ yields a domain wall solution, while the field σ leads to the formation of a nonzero condensate inside the domain wall. After solving the equations of motion of this initial Lagrangian, the theory will be generalised to the case in which σ is complex, in order to couple it to a $U(1)$ gauge field.

The Lagrangian is

$$\mathcal{L} = \frac{1}{2}\partial_\mu\phi\partial^\mu\phi + \frac{1}{2}\partial_\mu\sigma\partial^\mu\sigma - V(\phi,\sigma), \tag{6.1}$$

with a potential

$$V(\phi,\sigma) = \frac{1}{4}(\phi^2-1)^2 + \frac{1}{2}m^2\sigma^2 + \frac{1}{4}\lambda\sigma^4 + \frac{1}{2}d\sigma^2(\phi^2-1). \tag{6.2}$$

In this potential, the fields ϕ and σ are rescaled as to normalize the vev_ϕ of the ϕ field to ± 1. $\lambda, m^2, d > 0$ are the parameters which will dictate whether σ takes on nonzero

values. Note that the quartic for the field ϕ is set to 1 without loss of generality (it can be removed with a coordinate redefinition [89]).

We will now look for domain wall solutions of this system in which both fields take a nontrivial profile. To ensure that this system acquires a nontrivial lowest energy state, we will set a condition on the parameters d, m^2 and λ. The goal is to obtain a profile like $\phi \neq 0, \sigma = 0$ outside of the domain wall and $\phi \to 0, \sigma \neq 0$ inside the domain wall.

$$\begin{cases} \phi = \pm 1 & \sigma = 0 \quad \text{outside DW} \\ \phi \to 0 & \sigma \neq 0 \quad \text{inside DW} \end{cases} \tag{6.3}$$

To accomplish this, the absolute minima of the potential should always be at ($\phi = \pm 1, \sigma = 0$). Only when ϕ begins taking on nontrivial profiles like a domain wall, does σ get the opportunity to deviate from zero. The potential shows four minima, two at $\sigma = 0$ and two at $\phi = 0$ as demonstrated in the contourplot of Figure 6.1. The choice of λ will be made clear later. Correct parameter values were chosen to clearly show the correct potential situation.

Hence, of these four minima, the two associated to $\phi = \pm 1$ should be the deepest. Calculating the exact positions of the minima in the (ϕ, σ) plane can be done by demanding the derivative with respect to the fields of the potential to be zero. This yields values for the minima

$$min_\phi = (\pm 1, 0) \quad \text{and} \quad min_\sigma = (0, \pm\sqrt{\frac{d - m^2}{\lambda}}), \tag{6.4}$$

in which the subscript denotes the nonzero field. Demanding that $V(min_\phi) < V(min_\sigma)$ leads to a constraint in the parameters. This constraint will be noted as the vacuum condition and is written as

$$\text{Vacuum condition} \quad \lambda > (d - m^2)^2. \tag{6.5}$$

Equation (6.5) partly defines the parameter space in which this thesis is interested. More conditions can be imposed to obtain the "interesting" (i.e. nontrivial) solutions. In the next Section we will derive a condition which imposes a stable, nonzero solution for the condensate field σ.

6.2 Perturbation analysis

We now want to prove that a nonzero σ solution is optimal for a range of parameters. To prove this, we will observe a domain wall solution for ϕ together with a zero condensate

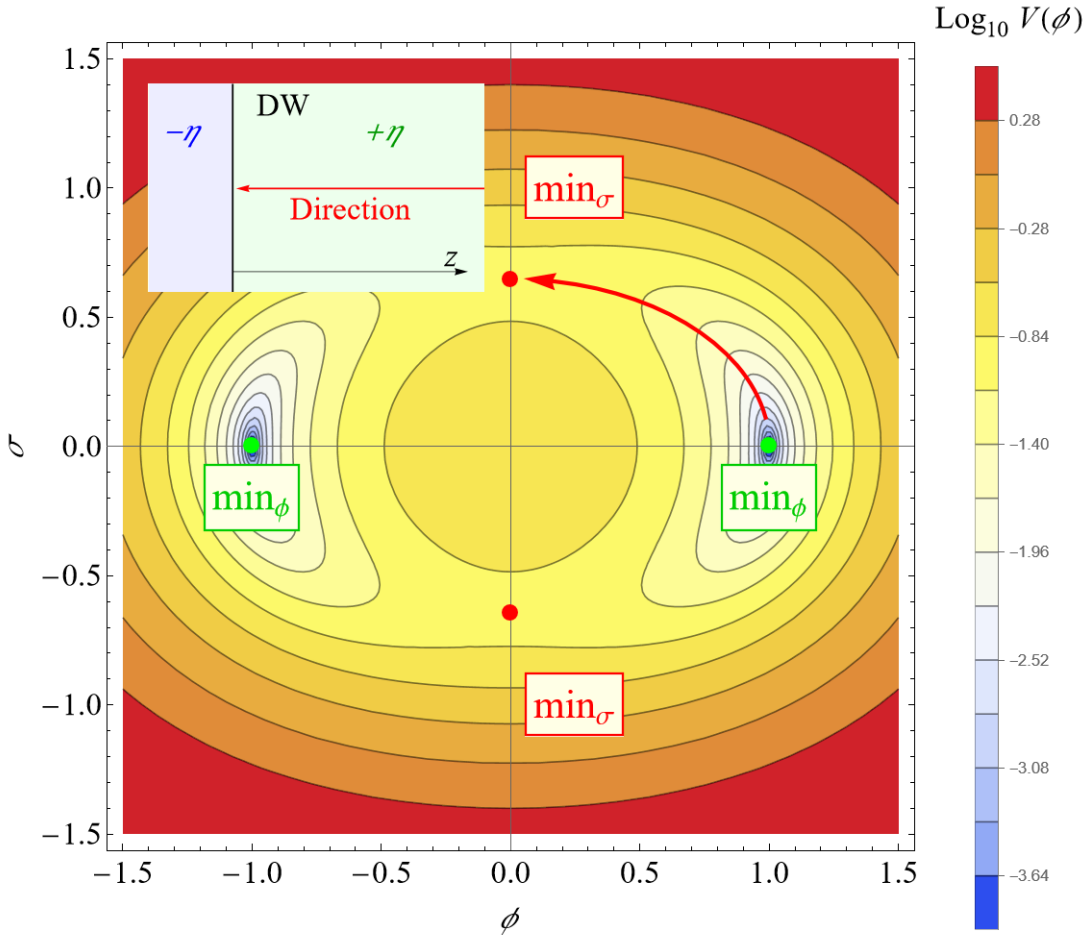

Figure 6.1: The contourplot of the $\log_{10}$ of the potential $V(\phi, \sigma)$ in Equation (6.2), for natural parameter values $m = 0.5$, $d = 1.5$ and $\lambda = \frac{d(d-2m^2)}{1-2m^2}$. The green points denote the $\phi \neq 0$ minima, while the red dots denote the $\sigma \neq 0$ minima. The red arrow sketches the behaviour of the fields in the (ϕ, σ) plane.

field $\sigma = 0$. By showing that this configuration is unstable, it is implied that σ will evolve to a nontrivial solution, as in Equation (6.3), to obtain a stable solution for the fields ϕ and σ.

To attempt this, a static $\sigma = 0$ background together with a standard domain wall along ϕ will be investigated. On this a small perturbation $\delta\sigma$ will be left to relax. Demonstrating that this perturbation grows, will show that the standard domain wall configuration $\sigma = 0$ is unstable for the chosen parameters and a nontrivial σ profile will appear

Observe the equations of motion stemming from the Euler-Lagrange equations on

the Lagrangian of Equation (6.1).

$$\phi: \quad \Box\phi + (\phi^2 - 1)\phi + d\sigma^2\phi = 0, \tag{6.6}$$

$$\sigma: \quad \Box\sigma + m^2\sigma + \lambda\sigma^3 + d(\phi^2 - 1)\sigma = 0. \tag{6.7}$$

The static background $\sigma = 0$ consists of the normal domain wall profile. Assuming the domain wall lies in the xy plane, the only dependency of the domain wall profile is along the $z - axis$: $\phi = \phi(z)$. We can substitute this and $\sigma = 0$ in Equation (6.6) to obtain the background solution. This yields

$$-\frac{\partial^2\phi}{\partial z^2} + (\phi^2 - 1)\phi = 0 \tag{6.8}$$

$$\Rightarrow \qquad \phi(z) = \pm\tanh\left(\frac{z}{\sqrt{2}}\right). \tag{6.9}$$

Note that the amplitude of the tanh is 1 since the original Lagrangian rescaled ϕ's vev to be ± 1. The $+$ sign is chosen in the solution, the $-$ sign is equivalent.

With this background solution in mind, we can introduce a perturbation on the condensate $\sigma = \delta\sigma$. The equations of motion with this perturbation substituted in can be simplified by only keeping terms to the lowest order. This yields exactly the same equation of motion for the domain wall field ϕ. The equation of motion of the condensate dictates the dynamics of the perturbation $\delta\sigma$. This reduced equation can be written as

$$\Box\delta\sigma + \left(m^2 + d\left(\tanh^2\left(\frac{z}{\sqrt{2}}\right) - 1\right)\right)\delta\sigma = 0, \tag{6.10}$$

in which the background solution to ϕ was already substituted. Assuming the perturbation to exhibit the same dependencies as the domain wall allows for defining an ansatz $\delta\sigma = \delta\sigma_0(z)e^{-i\omega t}$. This reduces the equation of motion to

$$-\frac{\partial^2\delta\sigma_0}{\partial z^2} + \left(m^2 - d\cdot\operatorname{sech}^2\left(\frac{z}{\sqrt{2}}\right)\right)\delta\sigma_0 = \omega^2\delta\sigma_0. \tag{6.11}$$

This equation is a one dimensional Schrödinger equation with a Pöschl-Teller potential. This is exactly solvable, given that the correct substitutions are made [82]. The desired result would be the existence of a reasonable condition for which the lowest energy state is negative $\omega^2 < 0$. This would imply an exponential growth of the perturbation $\delta\sigma \sim e^t$, leading to the conclusion that the background $\sigma(z) = 0$ is unstable.

Before exactly solving this equation, however, we will repeat the argument made by Witten in [7]. This argument was already applied in Section 4.2 to obtain a similar condition for which the superconducting strings contain a stable nonzero condensate.

Although the argument is more "handwavy" and yields a less strict condition it could provide an extra insight. In order to demand $\omega^2 < 0$, Equation 6.11's potential should at least not be positive definite. Demanding that the potential is not positive is equivalent to demanding that there exists at least one negative potential value. Demanding this of the potential found in Equation (6.11) yields

$$\exists\, z:\ m^2 - d \cdot \operatorname{sech}^2\left(\frac{z}{\sqrt{2}}\right) < 0. \tag{6.12}$$

We would prefer a condition that is independent of the coordinates. Since a condensate will only form inside the domain wall, the function sech^2 can be approximated by its function value at $z = 0$. This assumption interprets a domain wall as a two dimensional object by neglecting its width, a common practice when considering domain wall dynamics. The same "thin wall" assumption was already applied in Section 5.3. By substituting $\operatorname{sech}^2(0) = 1$ into Equation (6.12), the final condition is obtained. The expression reduces to

$$\text{Witten condition:} \quad m^2 < d, \tag{6.13}$$

which is labeled as the Witten condition. While this illustrates a procedure of finding conditions when no analytical solution is available, we can define a stronger condition by solving the Pöschl-Teller potential in Equation (6.11). We will now proceed in deriving this condition and showing that the results are more stringent than the Witten condition. A similar analysis was performed in [90]. The final condition will be shown to perfectly match the numerical results.

We revert back to the original Schrödinger equation, rewritten here for clarity

$$-\frac{\partial^2 \delta\sigma_0}{\partial z^2} + (m^2 - d \cdot \operatorname{sech}^2(\frac{z}{\sqrt{2}}))\delta\sigma_0 = \omega^2 \delta\sigma_0. \tag{6.14}$$

By choosing the correct substitutions, this equation can be rewritten to the defining equation for an associated Legendre function [82]. These substitutions redefine the coordinates and parameters as

$$u = \tanh\left(\frac{z}{\sqrt{2}}\right); \qquad \frac{s(s+1)}{2} = d; \qquad E = \omega^2 - m^2. \tag{6.15}$$

Note that E represents the energy of the solution. The Schrödinger equation in function of these substitutions becomes

$$((1-u^2)\delta\sigma_0')' + s(s+1)\delta\sigma_0 + \frac{2E}{1-u^2}\delta\sigma_0. = 0, \tag{6.16}$$

which is exactly the defining equation just mentioned. The associated Legendre function $P_s^\mu(u)$ is defined as the solution to this equation. The parameter μ can take on discrete values from 1 up to s: $\mu \in \{1, 2, ..., s\}$. The perturbation can hence be written as

$$\delta\sigma_0 = P_s^\mu(\tanh\left(\frac{z}{\sqrt{2}}\right)), \tag{6.17}$$

in which the coordinate u was already reverted back to its expression in z. The parameter μ is defined in function of the energy E as

$$\mu = \sqrt{-2E}. \tag{6.18}$$

The energy state for this solution is hence inversely proportional to the parameter μ. The original goal of this analysis was finding negative ω^2 values in the lowest energy state of the original problem. Since the energy E is linked to the parameter μ, we can define a lowest energy state in terms of the parameters. Combining the fact that μ has a maximum value of $\mu = s$ and the relation in Equation (6.18) yields a lowest energy state

$$E_0 = -\frac{s^2}{2}, \tag{6.19}$$

in which the subscript was added to denote the lowest possible value of E. Rewriting the expression in Equation (6.19) back to the original parameters yields an expression for the lowest possible eigenvalue ω_0^2 of the original problem,

$$\omega_0^2 = -\frac{(-1 + \sqrt{1 + 8d})^2}{8} + m^2. \tag{6.20}$$

The condition that will now be imposed is that in the lowest energy state this eigenvalue is negative $\omega_0^2 < 0$. This corresponds with an exponentially growing perturbation. This condition yields

$$\text{Condensate condition:} \quad m^2 < \frac{1}{4}(1 - \sqrt{1 + 8d}) + d. \tag{6.21}$$

Hence we have succeeded in finding a condition on the parameters m and d, for which a nontrivial condensate σ can form inside the domain wall solution ϕ. When this condition on the parameters is satisfied, any normal domain wall system i.e. $\phi \sim \tanh, \sigma = 0$ will decay into a nontrivial profile when σ is slightly perturbed [90].

In the remainder of this chapter we will assume Equation (6.21) to be the condition to be satisfied and neglect the condition set by Witten, since the Witten condition is automatically satisfied when the condensate condition is satisfied.

6.3 Analytical and numerical analysis

The previous pages were dedicated to finding conditions on the parameters m, d and λ for which a domain wall solution with a condensate i.e. a nontrivial σ profile would form. This first assumed the condition on the parameter space for which $\phi = \pm 1$ is the true vacuum. The perturbation analysis added an extra condition for which condensates could form. To clearly keep track of all parameter conditions they are collected here,

$$\text{Vacuum condition:} \quad (d - m^2)^2 < \lambda, \tag{6.22}$$

$$\text{Condensate condition:} \quad m < \sqrt{\frac{1}{4}(1 - \sqrt{1 + 8d}) + d}. \tag{6.23}$$

Before proceeding with the study of domain walls coupled to a condensate, it is important to note that for a certain choice of parameters the equations of motion of the Lagrangian (6.1) admit an analytical solution describing the domain wall with a non-vanishing condensate [89]. The choice of parameters yielding an analytical solution corresponds to a specific relation between the parameters in the potential. This specific analytical condition is

$$\text{Analytical condition:} \quad \lambda = \frac{d(d - 2m^2)}{1 - 2m^2}. \tag{6.24}$$

Note that this only makes up a small part of parameter space. Nevertheless, these analytical solutions will be crucial in testing the robustness of the numerical algorithm developed to solve the general equations of motion of Equations (6.6) and (6.7). The solutions for this parameter choice are

$$\begin{aligned} \phi(z) &= \tanh(mz), \\ \sigma(z) &= \pm\sqrt{\frac{1 - 2m^2}{d}}\,\operatorname{sech}(mz). \end{aligned} \tag{6.25}$$

The shape of these profiles is shown in Figure 6.2. This solution immediately demonstrates that there indeed do exist states with a nonzero σ profile.

For the interested reader: the analytical solution involves constructing the mechanical analogue of the equations of motion and observing polynomials of the fields that interpolate between different minima of the potential. These polynomials are denoted as orbits. The whole mathematically complete derivation can be found in [89].

Note that the choice of parameters in the contour plot of the potential shown in Figure 6.1 is now justified. They are chosen to both satisfy the Vacuum condition $(d-m^2)^2 < \lambda$ and the Analytical condition $\lambda = \frac{d(d-2m^2)}{1-2m^2}$ for natural values $m, d, \lambda \sim O(1)$.

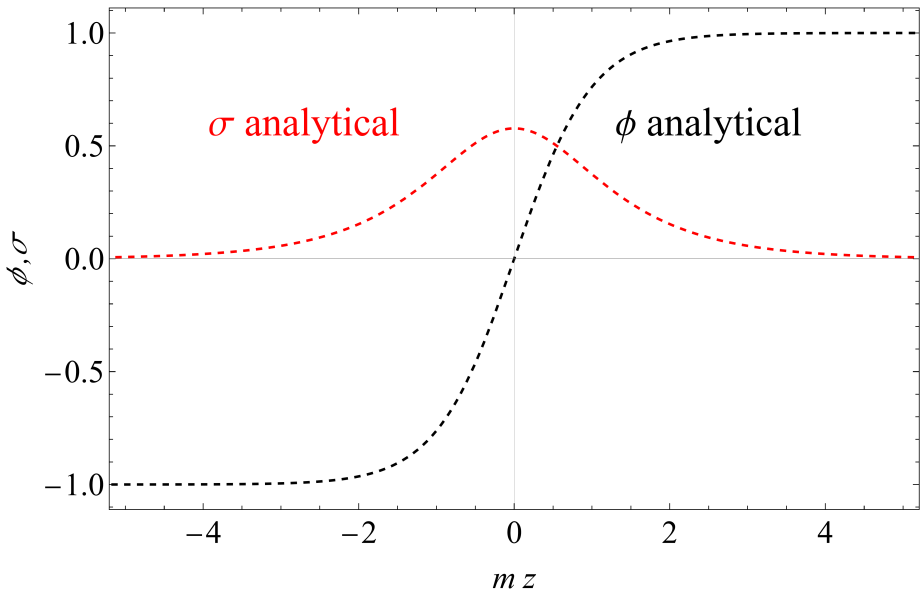

Figure 6.2: The analytical solutions of Equation (6.25) for parameters $m = 0.5$, $d = 1.5$ and λ chosen as in the analytical condition (6.24). The black dashed line denotes the domain wall profile, while the red dashed line denotes the condensate profile. The parameters satisfy the vacuum and condensate condition in Equations (6.22) and (6.23) . Note again that the asymptotes tend to $\phi = 1, \sigma = 0$. The horizontal axis is given in dimensionless units $m\, z$. All dimensional quantities are shown in units $vev_\phi = 1$.

Now that the analytical solution is known, we can test our numerical algorithm. This algorithm was already applied in Chapters 3, 4 and 5 to compute the field profiles of the introduced models. In the next part it will be applied to the Lagrangian (6.1). By first computing the solutions for a choice of parameters that satisfies the analytical condition (6.24) we are able to test whether the algorithm returns correct solutions. After that the algorithm will be applied to a broader part of parameter space to test the condensate condition (6.23).

6.3.1 Numerical domain wall profiles

Apart from the parameter space that allows for analytical solutions, this thesis intends to explore outside of this region by employing numerical methods. To accomplish this a relaxation scheme was constructed in Mathematica, the details of which can be consulted in Appendix B.1. A good check for the numerical methods is to compare it to the analytical solutions in the part of parameter space where the analytical solution exists, as defined in Equation (6.24). This comparison can be seen in Figure 6.3.

The numerical solution nicely lines up with the analytical profiles. The numerical techniques can now be used to extent the studied parameter space. Another good test

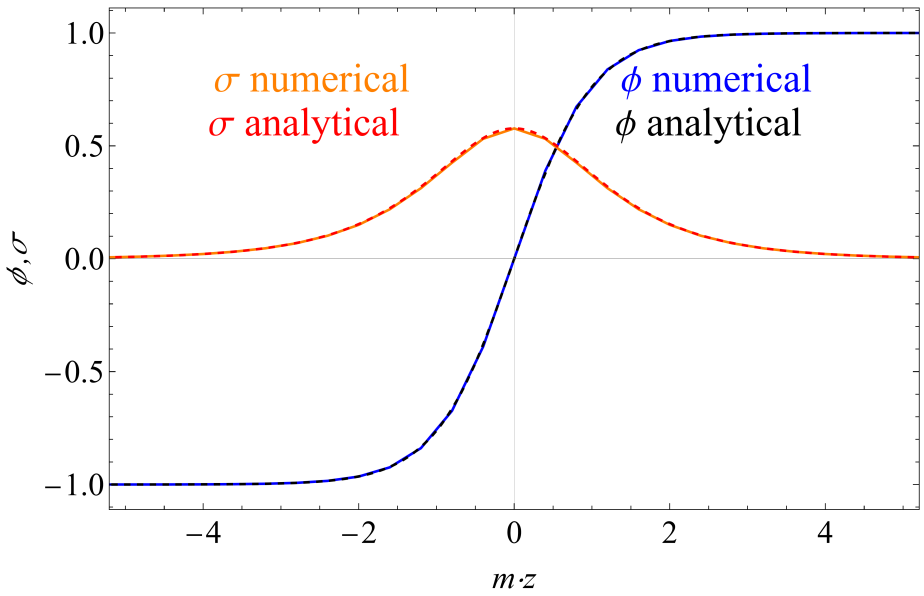

Figure 6.3: The comparison between numerical results, shown in solid lines, and analytical results, shown in dashed lines. The parameters are $m = 0.5$, $d = 1.5$, λ satisfying the Analytical condition (6.24). The horizontal axis is expressed in the dimensionless unit $m\,z$. All dimensional quantities are shown in units $vev_\phi = 1$.

for the numerical model is demanding only the Vacuum condition and exploring the parameter space (d, m) in a reasonable range for a fixed parameter λ. In this way the relaxation scheme can find a value for the condensate σ at the center of the domain wall, denoted as σ_{center} for every parameter combination d, m. The points (d, m, σ_{center}) can subsequently be represented in a contourplot, the colour indicating the value of σ_{center}. This can be seen in Figure 6.4.

The numerics delineate an area that nicely corresponds with the area implied by the Condensate condition. The contourplot also demonstrates that the argument made by Witten, while still including the parameter space where condensate formation is possible, is less exact than the perturbation analysis.

6.4 Complex condensate

Now that it was shown that for a correct choice of parameters d, m and λ a stable nonzero condensate σ forms inside the domain wall, one can try coupling a current to this formalism. To achieve this, the condensate field σ will be "upgraded" to a complex scalar field and gauged by U(1) gauge vector A^μ. The original Lagrangian of Equation (6.1) becomes:

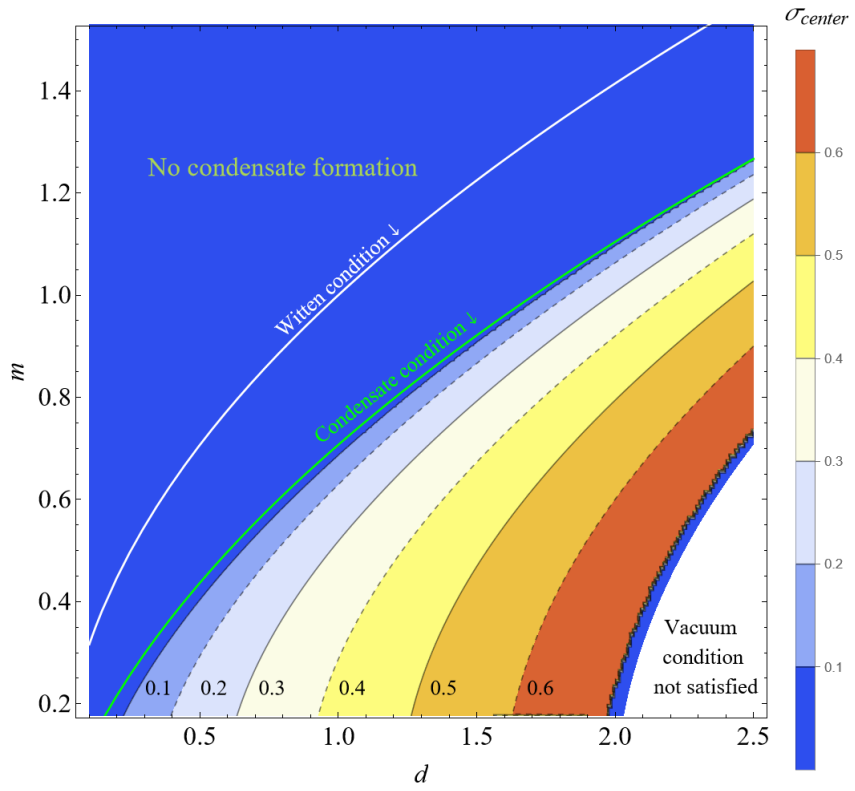

Figure 6.4: The contourplot representing (d, m, σ_{center}) for a fixed $\lambda = 4$. The region not satisfying the Vacuum condition is not included since the behaviour of the fields in this region would not even represent a domain wall. The green curve represents the limit of the Condensate condition. The white curve represents Witten's argument. All dimensionful quantities are given in units of $vev = 1$.

$$\mathcal{L} = \frac{1}{2}\partial_\mu\phi\partial^\mu\phi + \frac{1}{2}D_\mu\sigma(D^\mu\sigma)^* - V(\phi, |\sigma|) - \frac{1}{4}F_{\mu\nu}F^{\mu\nu}, \tag{6.26}$$

where the covariant derivative is defined as $D_\mu = \partial_\mu + ieA_\mu$ and a potential

$$V(\phi, |\sigma|) = \frac{1}{4}(\phi^2 - 1)^2 + \frac{1}{2}m^2|\sigma|^2 + \frac{1}{4}\lambda|\sigma|^4 + \frac{1}{2}d|\sigma|^2(\phi^2 - 1). \tag{6.27}$$

The equations of motion for the ϕ field remain the same:

$$\Box\phi + (\phi^2 - 1)\phi + d|\sigma|^2\phi = 0. \tag{6.28}$$

The new equations of motion for the complex σ field yield

$$(\partial_\mu + ieA_\mu)(\partial^\mu + ieA^\mu)\sigma + m^2\sigma + \lambda|\sigma|^2\sigma + d(\phi^2 - 1)\sigma = 0, \tag{6.29}$$

supplemented by the complex conjugate of this equation. The equation of motion for the gauge field yields

$$\partial_\mu F^\mu{}_\nu = e\mathrm{Im}\left(\sigma^*(\partial_\nu + ieA_\nu)\sigma\right). \tag{6.30}$$

It should now be possible to recreate the arguments made in Chapter 4 in order to study the electromagnetic current that can be generated along the domain wall. By picking an appropriate parameterization for the condensate field σ, one can model the condensates Goldstone bosons as excitations moving along the domain wall. This will allow proving the Meissner effect for a superconducting domain wall and defining a charging mechanism similar to the superconducting string.

The condensate will be parameterized for a domain wall perpendicular to the $z-$axis

$$\sigma(t, x, y, z) = \sigma_0(z)e^{i\theta(t,x,y)}. \tag{6.31}$$

$\rho(z)$ represents the static condensate solution set out in the previous Sections, while the phase $\theta(t, x, y)$ parameterizes the Goldstone bosons moving along the domain wall.

It is now possible to again define an effective theory by integrating out the behaviour over the $z-$axis, leaving only the dynamics of the bosons θ in $2 + 1$ dimensions.

$$S_{eff} = \int dz\sigma_0^2(z) \int dtdxdy \frac{1}{2} \left(\partial_\mu\theta + eA_\mu\right)\left(\partial^\mu\theta + eA^\mu\right) - \frac{1}{4}\int d^4x F_{\mu\nu}F^{\mu\nu}. \tag{6.32}$$

The equations of motion of this theory are

$$\Box\theta + e\partial_\mu A^\mu = 0 \tag{6.33}$$

for the Goldstone bosons and

$$\partial_\mu F^{\mu\nu} + eK\left(\partial^\nu\theta + eA^\nu\right) = 0 \tag{6.34}$$

for the gauge fields. Here the integral over the $z-$axis of the condensate was denoted with $K = \int dz\sigma_0^2(z)$. Similarly to Section 4.3.1, this K can be estimated by assuming a constant σ_0 over the z-axis. Substituting in the value of the condensate at $z = 0$ from Equation (6.4) yields

$$K \sim \frac{d - m^2}{\lambda}\delta_\sigma. \tag{6.35}$$

We are now ready to derive the superconductive properties of the domain wall coupled to a condensate.

6.4.1 Current and Meissner effect

The effective theory, which was inspired by Wittens effective theory of superconducting strings [7], can now be applied in a similar way to define a current and demonstrate the existence of the Meissner effect in superconducting domain walls. Since these calculations were performed covariantly in Chapter 4, it is straightforward to generalise them to domain walls. Note that we neglect to define a persistent current as was done in the superconducting string case of Chapter 4. This is due to the complex geometry associated to the topology of closing domain walls. This search for a persistent current equivalent for the superconducting domain wall warrants extra research. We will instead focus on the Meissner effect and the charging mechanism.

The current can be defined as

$$j^{\mu} = -eK(\partial^{\nu}\theta + eA^{\nu}). \tag{6.36}$$

Note that, contrary to the superconducting string, this current has spatial components along the $x-$ and $y-$axis. Equation (4.46) can be reused in this context,

$$\partial_j F^{ji} = \left(\nabla \times \vec{B}\right)^i. \tag{6.37}$$

This can be inserted in the spatial components of the equation motion for the gauge fields, outlined in Equation (6.34). This yields

$$\left(\nabla \times \vec{B}\right)^i = -Ke(\partial^i\theta + eA^i). \tag{6.38}$$

These spatial components run over x and y. Translating this equation into a vector equation can be done by defining the gradient vector as

$$\nabla\theta = \begin{pmatrix} \partial_x\,\theta \\ \partial_y\,\theta \\ 0 \end{pmatrix} \tag{6.39}$$

and the gauge three vector as

$$\vec{A} = \begin{pmatrix} A_x \\ A_y \\ 0 \end{pmatrix}. \tag{6.40}$$

Equation (6.38) in vector notation becomes

$$\nabla \times \vec{B} = Ke\left(\nabla\theta - e\vec{A}\right). \tag{6.41}$$

Taking the curl of both sides of the equation yields

$$\nabla(\nabla \cdot \vec{B}) - \nabla^2 \vec{B} = -Ke^2 \vec{B}. \tag{6.42}$$

Maxwell's equation $\nabla \cdot \vec{B} = 0$ brings this to the final result for the Meissner effect

$$\nabla^2 \vec{B} = Ke^2 \vec{B}. \tag{6.43}$$

6.4.2 Charging mechanism

The effective theory can also be utilised to illustrate a charging mechanism for domain walls. By assuming a uniform energy distribution along the domain wall i.e. the $xy-plane$, one can show that an electrical field polarised in the $xy-$plane leads to an increase of the current on the domain wall in the direction of the electrical field.

The assumption of a uniform energy distribution is equivalent to stating that the spatial derivatives along the domain wall are zero

$$\nabla j^t = 0. \tag{6.44}$$

since the left hand side is a gradient vector over x and y, solving this equation leads to two conditions

$$\partial_x \partial^t \theta = -e\partial_x A^t, \tag{6.45}$$
$$\partial_y \partial^t \theta = -e\partial_y A^t. \tag{6.46}$$

We will observe the time behaviour of the magnitude of the total spatial current, defined as

$$|\vec{j}| \coloneqq \sqrt{(j^x)^2 + (j^y)^2}. \tag{6.47}$$

Taking the time derivative of this expression yields

$$\partial_t |\vec{j}| = \frac{j^x \partial_t j^x + j^y \partial_t j^y}{\sqrt{(j^x)^2 + (j^y)^2}}. \tag{6.48}$$

Note that the spatial vector has components $\vec{j} = (j_x, j_y, 0)^T$ due to the effective theory only living on the domain wall. The domain walls in this thesis are always chosen to lie along the xy-plane. The spatial derivatives of the components can be calculated by plugging in the conditions (6.45), (6.46). The two derivations are equivalent. j_x will be calculated as an example. The definition of the current yields

$$\partial_t j^x = -Ke\partial_t \left(\partial^x \theta + eA^x\right). \tag{6.49}$$

The term $\partial_t \partial^x \theta$ can be substituted using Equation (6.45). This reduces the expression to

$$\partial_t j^x = Ke^2 \left(\partial_t A_x - \partial_x A_t\right), \tag{6.50}$$

in which the sign changes were obtained by pulling down the spatial indices.

The goal is to find an expression for the time derivative of the spatial current $\vec{j}$ in function of the electric field $\vec{E}$. The definition of the electric field can be substituted into Equation (6.50). The definition of the electric field is

$$E^i = -F^{0i} = \partial_0 A_i - \partial_i A_0. \tag{6.51}$$

Hence the change in time of the $x-$component of the current can be written as the electric field's $x-$component. This yields a final expression containing both the current's derivative and the electric field

$$\partial_t j^x = Ke^2 E^x. \tag{6.52}$$

The same calculation yields for the $y-$component

$$\partial_t j^y = Ke^2 E^y. \tag{6.53}$$

The complete behaviour can be written as

$$\partial_t |\vec{j}| = Ke^2 \frac{j^x E^x + j^y E^y}{\sqrt{(j^x)^2 + (j^y)^2}}, \tag{6.54}$$

$$= Ke^2 \, \hat{j} \cdot \vec{E}. \tag{6.55}$$

$\hat{j}$ denotes the unit vector in the direction of the current $\hat{j} = \vec{j}/|\vec{j}|$. One can conclude that an electric field generates a maximum current parallel to its direction. Hence an electric field in the x-direction generates a current in the x-direction.

We were able to show that an electric field acting on a superconducting domain wall will induce a current in the direction of the electric field.

As is the case with the superconducting string's charging mechanism, discussed in Section 4.4, the penetration of the electric field in the superconducting domain wall was

not included in the derivations. Inspired by [7], we estimate this efficiency by considering the fraction of the field that contributes to the current charging to be the ratio of the electric field value at the center of the domain wall over the amplitude of the incoming field. We did not calculate this fraction exactly, instead we are able to approximate the efficiency parameter by considering the superconducting domain wall as a $2+1$ dimensional object. A scattering problem determined by an incoming photon scattering on a superconducting domain wall can then be modelled as scattering on a δ-function potential. The desired ratio in this problem is then proportional to the transmission coefficient of the scattering problem [91]. In Section 6.5 of this chapter we compute the reflection coefficient of this scattering problem for more precise modelling of the scattering barrier for superconducting domain walls. This reflection coefficient R can then be used to find the transmission coefficient T (and hence the charging efficiency) as $T = 1 - R$.

An infinite charging of the domain walls is, similarly to the superconducting string case discussed in Section 4.4, not included in the theory. A sufficiently large current describes physics that fall outside the scale of the effective theory. The current appears in the potential as an effective mass term and by growing sufficiently large the potential reverts back to a parabola, restoring the symmetry. This can be seen in the effective action of Equation (6.32), without integrating out the $z-$behaviour the term $(\partial_\mu\theta + eA_\mu)(\partial^\mu + eA^\mu)\sigma_0^2$ contributes to the potential as described above.

A conservative guess can be found be considering the modified minimum of the field σ_0, which behaves exactly like the real field described before "promoting" the theory to a complex scalar field. The original minimum was given by

$$\sigma_{0\,min}^2 = \frac{d - m^2}{\lambda}. \tag{6.56}$$

The spatial current appears as a quadratic term with coefficient $\frac{1}{2Ke}(j_x^2 + j_y^2)$, adding this contribution to Equation (6.56) yields

$$\sigma_{0\,min\,mod}^2 = \frac{1}{\lambda}(d - m^2 - \frac{1}{Ke}(j_x^2 + j_y^2)), \tag{6.57}$$

To include this in the effective theory and make a guess for the maximum current, one can guess a modified $K = \int dz\sigma_0^2$ as was done in the beginning of this section. This can be achieved by guessing σ_0 as its largest value. Since σ_0 evolves from 0 outside the domain wall to $\sigma_{0\,min}$ inside, this can be taken as a guess. Plugging in the modified value yields

$$K_{mod} \approx \frac{1}{\lambda}(d - m^2 - \frac{1}{Ke}(j_x^2 + j_y^2))\delta_\sigma. \tag{6.58}$$

This expression shows that as the fields grow, K_{mod} decreases. Note that K still denotes the unmodified K. Equation (6.55) implies that the larger the current, the slower it grows until $K_{mod} \to 0$. This happens at a value:

$$j_x^2 + j_y^2 = Ke(d - m^2), \tag{6.59}$$
$$\Leftrightarrow \quad |\vec{j}| = \sqrt{Ke(d - m^2)}. \tag{6.60}$$

This can serve as a conservative guess for the maximum current and concludes the discussion on currents on a superconductive domain wall.

6.5 Photon reflection on a Superconducting Domain Wall

Now that the superconductive properties of a domain wall were explored, the thesis can start work on another area: friction. As described in Chapter 5, domain wall networks can evolve according to two distinct regimes; one dominated by the tension on the domain walls, called the scaling regime; the other by interactions with the cosmic plasma, called the friction regime. While most discussions on domain walls assume a scaling regime, the physics of the friction regime are intricate and warrant research of their own [11, 92, 93].

Modelling the friction acting on a domain wall can be achieved by calculating the reflection coefficient of the particle under investigation when encountering a domain wall. In this thesis, the encounter will consist of a photon scattering on the condensate formed inside a superconducting domain wall. When the reflection coefficient has been calculated, a pressure from the particles can be inferred [81] and one can calculate for which parameters the friction regime dominates the dynamics of the superconducting domain wall.

This Section aims to calculate the reflection coefficient for several scenarios. As a start, the calculations leading to the scattering equation will be set out. This will lead to a scenario where the scattering happens over a potential hill determined by the condensate. This potential hill will then be interpreted and numerics to calculate the reflection coefficient will be applied. First, the potential hill will be simplified to a delta function potential to test the robustness of the numerics. Afterwards the condensate parameters will be chosen such that the potential hill reduces to a sech^2. Both the scattering over a delta potential and scattering over a sech^2 can be analytically solved. Hence, we can compare our numerical solutions with these analytical solutions. As the final step, a potential hill found by numerically solving the condensate will be used.

6.5.1 Scattering equation

The equations stem from the assumptions that the domain wall lives in a $A^\mu = 0, \theta = 0$ background. In this background the ϕ and σ fields have their solutions found in the first Sections of this Chapter. These solutions obey the equations of motion given in (6.6) and (6.7).

The ansatz

$$\sigma = \sigma_0(z)e^{i\theta(t,x,y)} \tag{6.61}$$

can be plugged into the equations of motion, considering A^μ and θ to be perturbations. All higher orders of the perturbations A^μ and θ will be neglected. Before writing out this expression it saves time and space to note that any combination of the form $\partial_\mu\theta\partial^\mu\sigma_0$ can be set to 0 due to dependencies of θ and σ_0, since the only nonzero derivative of σ_0 is $\partial_z\sigma_0$, while $\partial_z\theta = 0$.

In the derivation of the Schrodinger equation, a particular gauge will be employed. This gauge will be briefly discussed as to avoid confusion later. Inspired by [94], a gauge choice $A_t = 0$, $A_z = 0$ is made. This does not completely fix the gauge. Consider the first gauge condition and a $U(1)$ gauge transformation under the phase $\varphi(t, x, y, z)$. Applying the gauge transformation on the condition yields

$$A_t = 0 \Rightarrow A_t + \frac{1}{e}\partial_t\varphi = 0 \Rightarrow \partial_t\varphi = 0, \tag{6.62}$$

which leaves a residual gauge freedom under the phase $\varphi(x, y, z)$, the same argument for $A_z = 0$ leaves a gauge freedom under the phase $\varphi(x, y)$. This freedom can be used to set the Goldstone boson $\theta(t, x, y)$ to be simply time dependent $\theta(t)$. The only gauge freedom left is under a constant phase φ. To demonstrate this the argument of (6.62) can be recreated for θ

$$\partial_x\theta = 0 \Rightarrow \partial_x\theta + \partial_x\varphi = 0 \Rightarrow \partial\varphi = 0. \tag{6.63}$$

The remaining gauge vector components are assumed to only depend on the direction perpendicular to the wall, in this case the $z-$axis $A_x = A_x(t, z)$ and $A_y = A_y(t, z)$.

The equations of motion will now be calculated, keeping into account these assumptions and the gauge choice. Plugging the ansatz into the equations of motion of σ (6.29) yields an expression

$$\begin{aligned} &\underline{\Box\sigma_0} + i\Box\theta\sigma_0 - \underline{\partial^\mu\partial_\mu\theta\sigma_0} + ie\partial\mu A^\mu\sigma_0 - 2\underline{A^\mu\partial_\mu\theta\sigma_0} \\ &-e^2\underline{A_\mu A^\mu\sigma_0} + \underline{m^2\sigma_0 + \lambda\sigma_0^2\sigma_0 + d(\phi^2 - 1)\sigma_0} = 0. \end{aligned} \tag{6.64}$$

Terms of the form $\partial^\mu\sigma_0\partial_\mu\theta$ were already set to 0. The expression $A_\mu\partial^\mu\sigma_0$ was likewise set to 0, since the chosen gauge ensures that $A_z = 0$, while σ_0's only nonzero derivative is ∂_z.

The parts underlined in (6.64) denote terms that can be set to 0. The terms underlined in red comprise the left hand side of the original background equation of motion of σ_0. Since σ_0 was not perturbed, the field still satisfies this equation and hence the terms in red combined can be set to 0. The terms underlined in blue denote terms that were neglected due to being of higher order in the perturbation (perturbation^2). The equation left is

$$\Box\theta + e\partial_\mu A^\mu = 0. \tag{6.65}$$

The gauge choice $\theta = \theta(t)$ and $A_t = A_z = 0$ can be employed to simplify this further

$$\partial_t^2\theta = 0. \tag{6.66}$$

Note that the equation of motion (6.65) is exactly the one for the effective theory described in Section 6.4.

The equation of motion for the gauge field yields:

$$\partial_\mu F^\mu{}_\nu + e\sigma_0^2(\partial_\nu\theta + eA_\nu) = 0. \tag{6.67}$$

The chosen gauge implies that $\partial_\mu A^\mu = \partial_t A^t - \partial_x A^x - \partial_y A^y - \partial_z A^z = 0$. The equations of motion for the x and y components yield

$$\Box A_x + e^2\sigma_0^2 A_x = 0 \tag{6.68}$$

and

$$\Box A_y + e^2\sigma_0^2 A_y = 0, \tag{6.69}$$

since $\theta = \theta(t)$ its derivatives to x and y are zero. Plugging in an ansatz $A_x = A_x(z)e^{-i\omega t}$ yields the final Schrödinger equations of the scattering problem.

$$-\partial_z^2 A_x + e^2\sigma_0^2 A_x = \omega^2 A_x \tag{6.70}$$

and its equivalent for the $y-$component,

$$-\partial_z^2 A_y + e^2\sigma_0^2 A_y = \omega^2 A_y. \tag{6.71}$$

Note that the potential hill is defined by the condensate profile perpendicular to the domain wall. We solve the reflection coefficient of the Schrödinger equations (6.70) (or equivalently (6.71)). The reflection coefficient corresponds to the probability of the gauge field A^μ to be reflected by the domain wall condensate, here represented by the profile σ_0, which constitutes a potential barrier in the Schrödinger equation. These results are used in Chapter 7 to estimate the pressure induced by the photon bath on the superconducting domain walls in the early Universe.

We perform these calculations for increasingly complex scenarios. Firstly, the potential hill will be simplified to a delta potential $\sigma_0^2 \to \delta$. In this configuration, analytical solutions for the reflection coefficient exist. These will be used as a comparison with our reflection coefficient, which is found by applying the numerical analysis outlined in Appendix B.2.

After discussing the delta potential we will assume the condensate's parameters allow for the analytical solution of the condensate, described in Equation (6.25), $\sigma_0^2 \to \text{sech}^2$. This reduces the Schrödinger equation to solving the Pöschl-Teller potential, which was already encountered in Section 6.2 and an analytical solution for the reflection coefficient is provided. Similarly to the delta potential, we compare our numerical result with the analytical solution.

Finally, we solve the equation of motion of the condensate (6.7) with our numerical algorithm used to compute the field profiles in the previous chapters. This numerically found condensate profile is then substituted into the Schrödinger equation (6.70) (or (6.71)), after which the reflections coefficients are numerically calculated. To maintain an overview, a table of the substituted potentials and the way in which they are solved is included in Table 6.1.

A wave polarised along the $x-$axis will be assumed, hence only Equation (6.70) need be solved.

Table 6.1: Table showing the potentials for which the reflection coefficient is computed on the left hand side and the methods by which the reflection coefficient is computed on the right hand side.

Potential hill	**Reflection coefficient**
δ potential	Analytical, numerical
sech^2 potential	Analytical, numerical
Numerical potential	Numerical

6.5.2 Delta potential

The simplest possible function to consider as a potential hill is the delta function. The motivation for this choice is based on the analytical solution to the condensate. The profile of the field σ_0 for the superconducting domain wall can have an analytic solution for a specific choice of parameters, as shown in Section 6.3, which reads

$$\sigma_0(z) = \pm\sqrt{\frac{1-2m^2}{d}}\,\text{sech}(mz). \tag{6.72}$$

Note that the prefactor $\sqrt{\frac{1-2m^2}{d}}$ seems wrong when looking at the dimensions of the terms. This can be rectified by interpreting 1 as a dimensionful quantity, since it denotes (1 times the *vev* of ϕ)^2. This confusion is due to the definition of the Lagrangian (6.1) in which ϕ was rescaled.

To simplify notation, the prefactor will be denoted as $S \coloneqq \frac{1-2m^2}{d}$. The positive solution will be utilised. The coordinate z can be rescaled to $Z \coloneqq m\,z$ in order to work with dimensionless quantities. m is the factor associated to the quadratic term of σ in the potential (6.27). Equation (6.70) reduces to the form

$$-\partial_Z^2 A_x + S\frac{e^2}{m^2}\operatorname{sech}^2(Z)A_x = \frac{\omega^2}{m^2}A_x. \tag{6.73}$$

This equation will be solved in the next step, but it will first be simplified further to illustrate the numerics. The sech^2 can be approximated as a delta function. To match dimensions one can use a property of the delta function that its dimension is the inverse of its argument. $\delta(mz) = \delta(Z)$ is dimensionless and can be used as an approximation.

The Schrödinger equation is

$$-\partial_Z^2 A_x + S\frac{e^2}{m^2}\delta(Z)A_x = \frac{\omega^2}{m^2}A_x. \tag{6.74}$$

The one dimensional scattering over a delta function potential is a well documented problem and has an analytical solution. The reflection coefficient R is found to be [91]

$$R = \frac{\beta^2}{1+\beta^2}, \tag{6.75}$$

in which β is defined as $\beta \coloneqq -\frac{e^2 S}{\omega m}$, which is dimensionless. The numerics described in Appendix B.2 can solve this equation to find a reflection coefficient. The results can be seen in Figure 6.5.

The figure shows good overlap between the developed numerics and the analytical solutions for a simple system like Equation (6.74). This section can hence conclude that the numerics agree with analytical solutions for the simplest approximation possible. To further explore the robustness of the numerical model, the analytical condensate solution can be used as a potential to scatter on.

6.5.3 Hyperbolic secant potential

Equation (6.73) was simplified by introducing a delta function potential to replace the sech^2 factor. This was done to test the numerics on the simplest possible problem. An analytical solution for Equation (6.73) is also available. This problem is scattering over a Pöschl-Teller potential and yields an analytical expression for the reflection coefficient [82]

$$R = \frac{\cos^2\left(\frac{\pi}{2}\sqrt{1-4e^2S/\,m^2}\right)}{\sinh^2\left(\pi\frac{\omega}{m}\right)+\cos^2\left(\sqrt{1-4e^2S/\,m^2}\right)}. \tag{6.76}$$

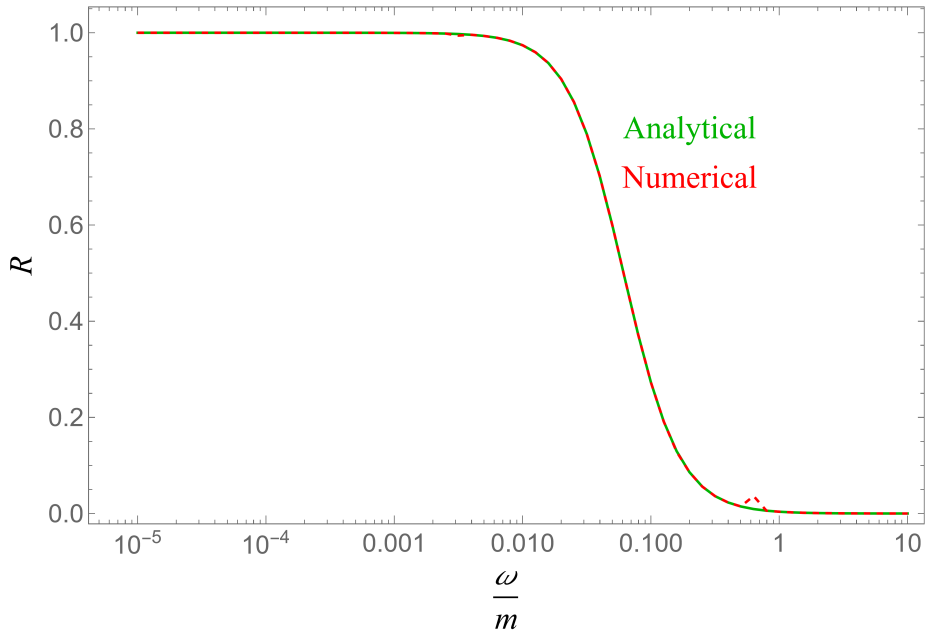

Figure 6.5: The results of the numerical and analytical analysis of Equation (6.74). The parameters are chosen as $e = 0.303$, $m = 0.5$ and $d = 1.5$. The numerics are denoted in a dashed, red line. The analytical solution is denoted in green. This simple system shows good overlap, except for a slight "bump". This deviation can be explained by the numerics having trouble with a non-continuous function like the delta function.

Solving this numerically yields the results seen in Figure 6.6.

Again the numerics agree with the analytical solutions. Hence the numerical model is robust enough to be used on a wider parameter space where no analytical solutions exist to double-check the results.

6.5.4 Numerical potential

As a final equation to solve, the factor σ_0^2 will be described by the numerically found condensate solution. This will at first be done with parameters that still allow for an analytical solution i.e. they satisfy the analytical condition of Equation (6.24). This "doubly numerical" result should coincide with the results from the Pöschl-Teller potential, since these were found by substituting in the analytical results of the condensate σ_0. The results can be seen in Figure 6.7.

Again, the numerics line up with the analytically expected results. These three examples provide enough robustness for the numerical model to confidently choose parameters m, d and λ to model a condensate without an analytical solution and compute its reflection coefficients. These results can be seen in Figure 6.8.

It can be concluded that the numerical methods for finding both the condensate

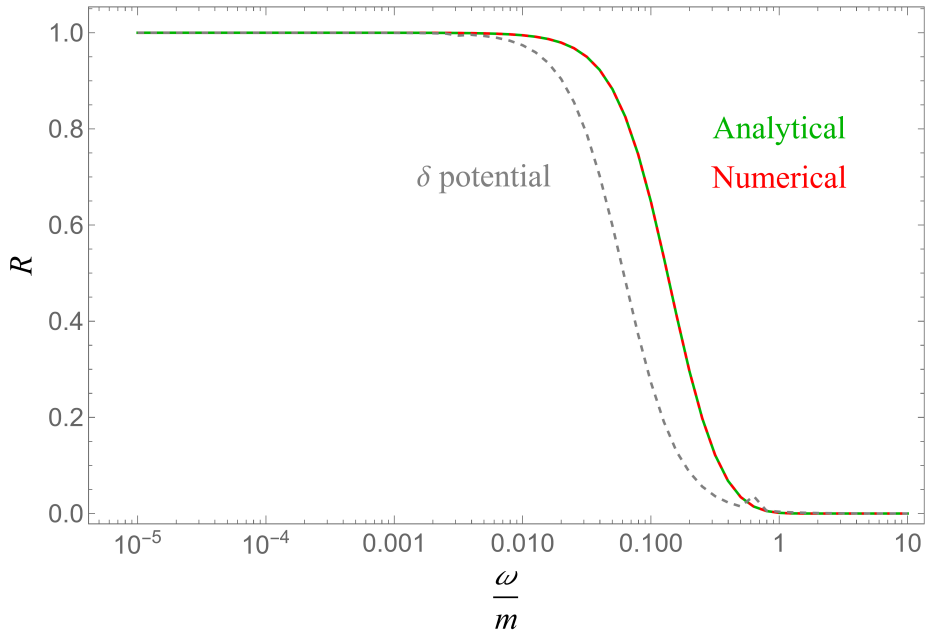

Figure 6.6: The results of the numerical analysis of the Pösch Teller potential scattering in Equation (6.73). The parameters were chosen as $e = 0.303$, $m = 0.5$ and $d = 1.5$. A comparison with the previous delta potential numerics is included to show the impact of simplifying a sech^2 to a delta potential.

profile σ_0 and reflection coefficient R of a photon interacting with the superconducting domain wall are sufficiently validated to be used with confidence in the next chapter.

6.6 Summary

This Chapter set out to explore all properties of superconducting domain walls relevant to this thesis. The general model of a domain wall coupled to a scalar field was first introduced without the complex phase and gauge fields. In this setup it was shown that stable solutions in which the condensate field σ takes on nonzero values inside the domain wall do exist. The conditions on the parameters to achieve such a model were specified and the parameter space in which a stable condensate forms was mapped. The parameters for which an analytical solution exists were defined.

This analytical solution allowed for testing a numerical algorithm which solved the equations of motion of the condensate field σ to find a profile inside the domain wall. This was first done for parameters that allow for an analytical solution to check the results of the numerics. After confirming the value of the numerical model, it was used to go beyond the analytical parameter space and explore for which values a stable condensate forms. This agreed with the conditions set in the beginning of the Chapter.

After this analysis the condensate field was "upgraded" to a complex scalar field,

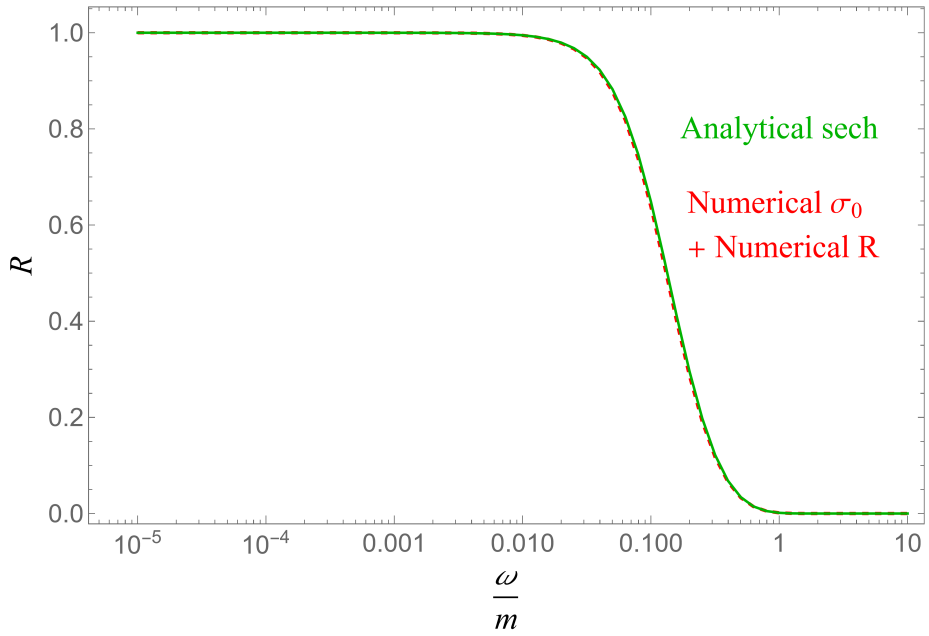

Figure 6.7: The numerical results for solving Equation (6.70) with a potential consisting of the numerically found condensate for parameters $m = 0.5$ and $d = 1.5$ and λ satisfying the analytical condition given in Equation (6.24).

gauged by a U(1) gauge vector. This allowed for defining a current on the domain wall and calculating both the Meissner effect and a charging mechanism for the superconducting domain wall to obtain a current.

The Chapter ended with calculating the scattering of a photon on the superconducting domain wall and testing a numerical algorithm for calculating the reflection coefficient R. This was done for increasingly more complex choices of potentials on which to scatter, ending with a numerical condensate profile. The thesis can now move on to the final Chapter, in which the friction regime will be explored in more detail.

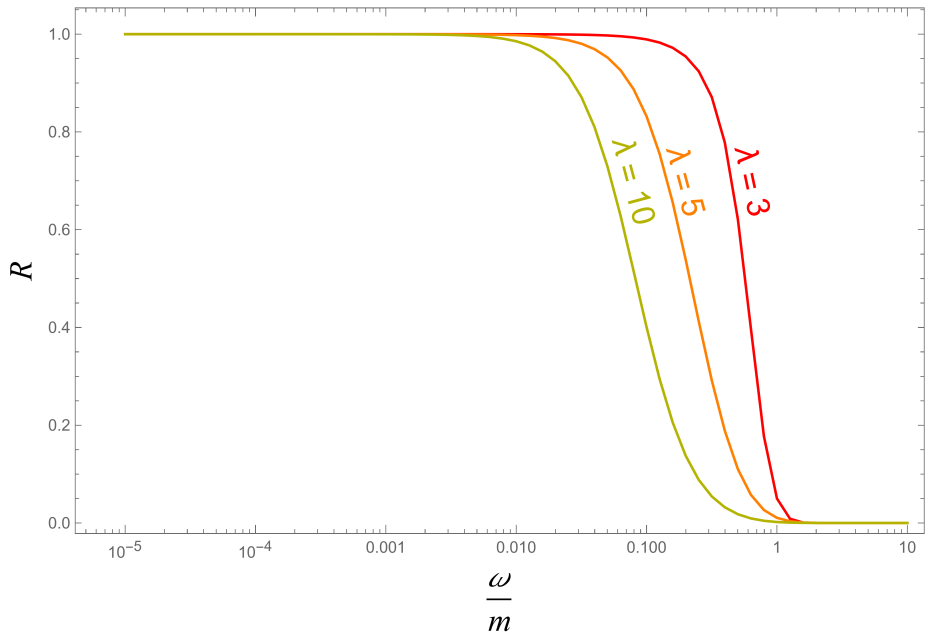

Figure 6.8: The purely numerical condensate results for parameters $m = 0.3$, $d = 1.7$ and $\lambda = 3, 5, 10$. All lines were found by numerically calculating the reflection coefficient R. A variation in the parameters was chosen to illustrate how the numerical algorithm can probe different parts of parameter space. The behaviour of the curves in function of the parameter λ can be explained by observing the height of the potential hill σ_0. The maximum of this hill is the maximum value of the field profile of σ_0, which is dependent on λ^{-1} as shown in Equation (6.4). Increasing λ, hence decreases the height of the potential hill, leading to a decrease in particles reflected in the potential hill.

7 Friction on superconducting domain walls

As a final application of the superconducting domain wall configuration, the friction regime will be explored in more detail. It will be shown that by calculating the pressure due to the interaction of superconducting domain walls with photons in the cosmic plasma, their friction due to radiation can be parameterized and calculated. This result will be compared with the scaling of the Hubble parameter to determine at what temperatures the friction regime dominates. A parameter space in $(T_{ann}, \sigma^{1/3})$ *will be constructed, for which the domain wall spectra will be compared to the sensitivity curves of current and future gravitational wave detectors. Finally, the comparison with the Hubble parameter will allow us to define an area in this parameter space in which domain wall behaviour will be characterised by the friction pressure.*

The friction computations on a superconducting domain wall are original work. The experimental sensitivity plot without a friction area is an extension of an existing result. The friction affected parameter space is original work.

7.1 Friction and Hubble

As mentioned in Section 5.3, domain walls can enter two regimes. Either a domain wall's dynamics are governed by the scaling regime, determined by the force their tension exerts [60] and described in Equation (5.16); or the equations of motion are dominated by a friction regime, in which the interactions between domain walls and the cosmic plasma of the early Universe determine the primary force acting on the domain walls [11, 81, 92], as described in Equation (5.42).

Domain walls are most often assumed to live in the scaling regime at later times. Since the Universe cools as time passes, the interactions with the cosmic plasma decrease as the temperature drops beneath the mass of the massive interacting particles (since the interacting particles become non-relativistic). Hence at sufficiently late times, one can assume that domain walls assume their scaling regime.

Later times are interesting to study because the size of the gravitational waves emitted by domain walls is dominated by their emission at later times i.e. when the domain wall network annihilates. This can be seen in Equation (5.65), in which the peak is dependent on T_{ann}^{-4} i.e. the latest time at which the source is active.

Hence, in many studies of domain walls the effect of friction on the dynamics of the domain walls is often neglected. However, it is not a priori obvious that the late time evolution of DWs is not influenced by friction. For example, the argument that interactions can be neglected at late times (lower temperature) fails to consider low mass particles.

In the case in which friction dominates at the final stage of the domain wall evolution, at T_{ann}, the domain wall's emission of gravitational waves would be modified [81, 92]. For this reason it is important to explicitly verify when friction is dominant at the annihilation time, where the GW signal is at its maximum. The derivation of the

frictional force that particles exert on a domain wall is reviewed in Appendix C. The friction pressure is derived from the reflection coefficient, as already explained in Section 5.3.

To study the parameter space for which friction becomes important, we will apply Equation (5.43). The equations that are reused will be rewritten here for clarity.

$$3H \lesssim \frac{1}{l_f}, \tag{7.1}$$

is the condition for friction on a domain wall to become relevant. The quantity l_f is the friction length and can be interpreted as a mean free path of interactions between domain wall and cosmic plasma. The condition is similar to a freeze-out condition, since it compares a mean interaction length with the expansion of the Hubble volume, the length of which is determined by the Hubble parameter as H^{-1}.

To calculate the friction length l_f, we will apply its approximation as given in Equation (5.44),

$$\frac{1}{l_f} \approx \frac{\Delta P}{\sigma v}. \tag{7.2}$$

This equation parameterises the mean interaction length of the particles by observing the pressure ΔP the cosmic plasma exerts on the domain walls. The velocity v of the domain wall will also appear in the expression to calculate ΔP and will hence have no influence on the friction length. One can see that highly dense domain walls will experience less friction since a high tension σ leads to a long friction length l_f. This behaviour was expected (imagine throwing a golf ball at a heavy truck).

The pressure calculations were performed in [81] and the result was already mentioned in Equation (5.42). The pressure exerted on a domain wall can be written as

$$\Delta P = v\frac{g}{\pi^2}\int_0^\infty dp_z p_z^3 \mathcal{R}(p_z) \exp\left(-\frac{\sqrt{m^2+p_z^2}}{T}\right). \tag{7.3}$$

The dampening of the friction force at temperatures T lower than the mass of the interacting particles m can be observed in the exponential. The biggest contributions to the pressure are determined by the particle momenta perpendicular to the domain wall p_z and the probability of interacting $\mathcal{R}(p_z)$. Note that this configuration again assumes a domain wall perpendicular to the z-axis.

To calculate the pressure, an expression for the probability $\mathcal{R}$ is required. In Section 6.5, the probability of interaction was interpreted as the reflection coefficient yielded by

considering a scattering problem of photons on the domain wall. The scattering yielded a Schrödinger equation of the form

$$-\partial_z^2 A_x + e^2\sigma_0^2 A_x = \omega^2 A_x, \tag{7.4}$$

in which σ_0 is the field profile of the condensate perpendicular to the domain wall and ω the frequency of the scattering photons. The numerics to solve these scattering problems were developed in Appendix B.2 and applied in Section 6.5. Figure 6.8 illustrates the resulting reflection coefficients.

We are now ready to apply these reflection coefficients to the friction problem. The goal is to calculate the friction length l_f and compare it with the Hubble parameter as in the condition defined in Equation (7.1). By applying this comparison at the correct time, we can define for what parameters a domain wall will still be in the friction regime at its annihilation temperature. Since the gravitational wave spectrum produced by a domain wall is mainly determined by its behaviour at the annihilation time, the friction regime at annihilation temperature will influence the gravitational wave spectrum .

To illustrate the procedure, an example of the comparison of friction length and Hubble scale for a fixed $vev_\phi = 10^5$ GeV can be seen in Figure 7.1. One can observe that the ratio between friction and Hubble scales over time. Note the inverse of the temperature on the horizontal axis. At early times friction dominates, as was expected. The position of the annihilation temperature of the domain wall on the horizontal axis dictates whether a domain wall is friction dominated at its annihilation. This region is shaded in red. After the Universe cools down sufficiently, the friction no longer dominates and the scaling regime takes over. This area is shaded in blue.

By applying this calculation and comparison over a range of parameters, we can determine in what areas of parameter space friction dominates up to the annihilation temperature. This procedure will be applied in the final Section of this chapter. As an intermediate step, we will first define the parameter space over which the friction calculations will be performed. To link these predictions to experiment, the parts of parameter space visible to current and future gravitational wave detectors will be illustrated.

7.2 The gravitational wave parameter space

In this section we explore the parameter space for domain walls (tension and annihilation temperature) and we study the corresponding gravitational wave signals and its detectability. This is done by considering the quantities that define a gravitational wave signal emitted by a domain wall, as described in Section 5.4. After defining the parameter space, we iterate over a grid on the parameter space to determine whether a domain wall with the chosen parameters emits a detectable gravitational wave, assuming that the dynamics of the domain wall are determined by the scaling regime. In the next Section, we identify the area of parameter space over which the friction regime dominates at the annihilation temperature. Hence, in this area the formalism for determining the

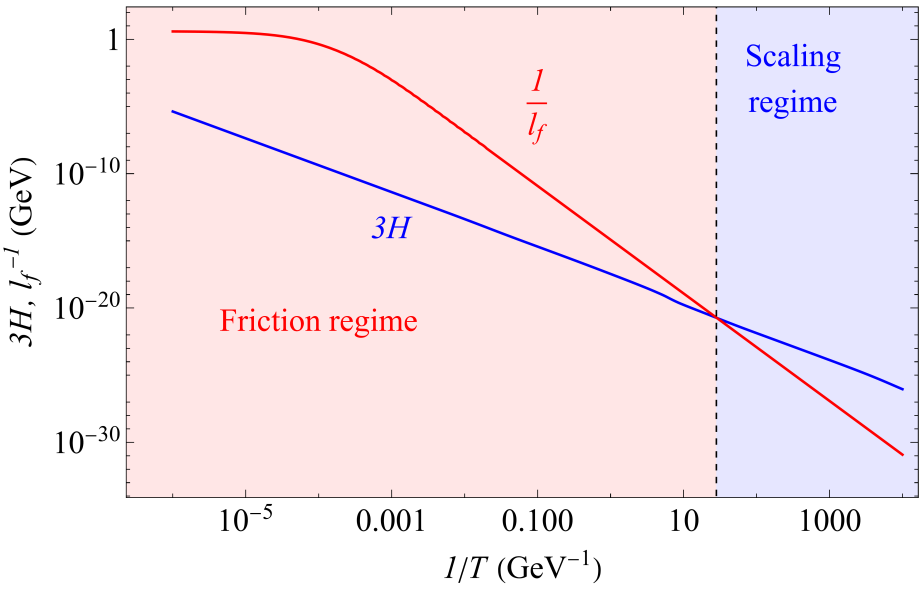

Figure 7.1: The friction regime condition of Equation (7.1) illustrated by calculating the behaviour of the friction length in function of temperature and comparing it with the Hubble parameter. The friction length was calculated with a numerically found reflection coefficient. The condensate that acts as a potential hill to scatter on was found by numerically calculating the field profile σ_0 for parameters $m = 0.5 vev_\phi$, $d = 1.5$, $\lambda = 3$ and a fixed $vev_\phi = 10^5$ GeV.

detectability should be modified.

To define the parameter space, observe the quantities that determine the spectrum Ωh^2 of a gravitational wave emitted by a domain wall. The peak f_{peak} of the spectrum, observed in the current epoch $t = t_0$, is located at

$$f_{peak}(t_0) = 1.1 \times 10^{-9}\ \text{Hz} \left(\frac{g_*(T_{ann})}{10}\right)^{\frac{1}{2}} \left(\frac{g_{*s}(T_{ann})}{10}\right)^{-\frac{1}{3}} \left(\frac{T_{ann}}{10^{-2}\ \text{GeV}}\right). \tag{7.5}$$

One can observe that this quantity only depends on the annihilation temperature T_{ann}. Therefore, the annihilation temperature is a good parameter to study the phenomenology of domain walls and their gravitational wave signatures.

The amplitude of the spectrum at the peak Ωh^2_{peak} can be deduced as

$$\Omega_{GW} h^2(t_0)_{peak} = 7.2 \times 10^{-18} \tilde{\epsilon}_{GW} A^2 \left(\frac{g_{*s}(T_{ann})}{10}\right)^{-\frac{4}{3}} \left(\frac{\sigma}{1\ \text{TeV}}\right)^2 \left(\frac{T_{ann}}{10^{-2}\ \text{GeV}}\right)^{-4}, \tag{7.6}$$

which depends on both the annihilation temperature T_{ann} and the tension σ. The other parameter that we will use is hence the tension σ and one can define a 2 dimensional

parameter space dependent on the tension and annihilation temperature. To define both directions with the same dimension the parameter space is defined with coordinates

$$\text{parameter space:} \quad (T_{ann},\, \sigma^{1/3}). \tag{7.7}$$

We can already exclude parts of this parameter space by considering the conditions under which domain walls can form and exists in the early Universe. By considering the maximum bias V_{bias} for which domain walls can form and the lowest temperature T_{ann} for which domain walls annihilate before dominating the energy density of the Universe, Section 5.4 set two conditions on T_{ann} and σ, an upper and lower bound. These will be repeated here for clarity.

Upper bound:

$$T_{ann} < 3.04 \times 10^4 \text{ GeV } C_{ann}^{-\frac{1}{2}} A^{-\frac{1}{2}} \left(\frac{g_*(T_{ann})}{10}\right)^{-\frac{1}{4}} \left(\frac{\sigma}{\text{GeV}}\right)^{-\frac{1}{2}} \left(\frac{V_0}{\text{GeV}^4}\right)^{\frac{1}{2}}, \tag{7.8}$$

Lower bound:

$$T_{ann} > 1.62 \times 10^{-5} \text{ GeV } C_{ann}^{\frac{1}{4}} A^{\frac{1}{2}} \left(\frac{g_*(T_{ann})}{10}\right)^{-\frac{1}{4}} \left(\frac{\sigma}{\text{TeV}^3}\right)^{\frac{1}{2}}. \tag{7.9}$$

The upper bound ensures that the bias introduced in Chapter 5 is sufficiently small to allow for formation of domain walls. The lower bound demands that the bias is sufficiently large such that domain walls annihilate before dominating the Universe.

The values not excluded by the bounds in Equations (7.8) and (7.9) can be used to compare the gravitational wave spectra of the domain walls with the sensitivity curves of several experiments. These sensitivity curves represent the frequencies and amplitudes visible to the experiment. As an example one can again consult Figure 5.6. In this figure an example of a spectrum visible to the experiments LISA and ET is plotted. One can state its visibility by observing that the spectrum intersects the sensitivity curves. In other words the area in $(f, \Omega h^2)$ space that lies above the sensitivity curves represents visible points of potential spectra. Appendix A.1 can be consulted for the details on how these curves are calculated.

We can now define a spectrum for every point $(T_{ann},\, \sigma^{1/3})$ and check whether the spectrum intersects with the sensitivity curves of several important gravitational wave detectors. The results of this procedure can be seen in Figure 7.2. The colored areas represent points that yield a spectrum visible to the corresponding experiment. The areas excluded by the upper (domain wall domination) and lower (percolation exclusion) bounds are shaded in gray.

The experiments in the lower temperature range represent lower frequency measurements. The North American Nanohertz Observatory for Gravitational waves (NANOGrav) [95] and the Square Kilometre Array (SKA) [96] are pulsar timing arrays (PTA) and

both measure pulsar emitted radio waves. LISA [97] and BBO [98] will be space based interferometes. CE [99], ET [100] are proposed ground based interferometers and HLVK [101] is a current ground based collaboration.

One can observe that a significant part of parameter space will be detectable when all these experiments are operational. Note from left to right the difference in parameter space sensitivity between the PTA's, space based interferometers and ground based interferometers.

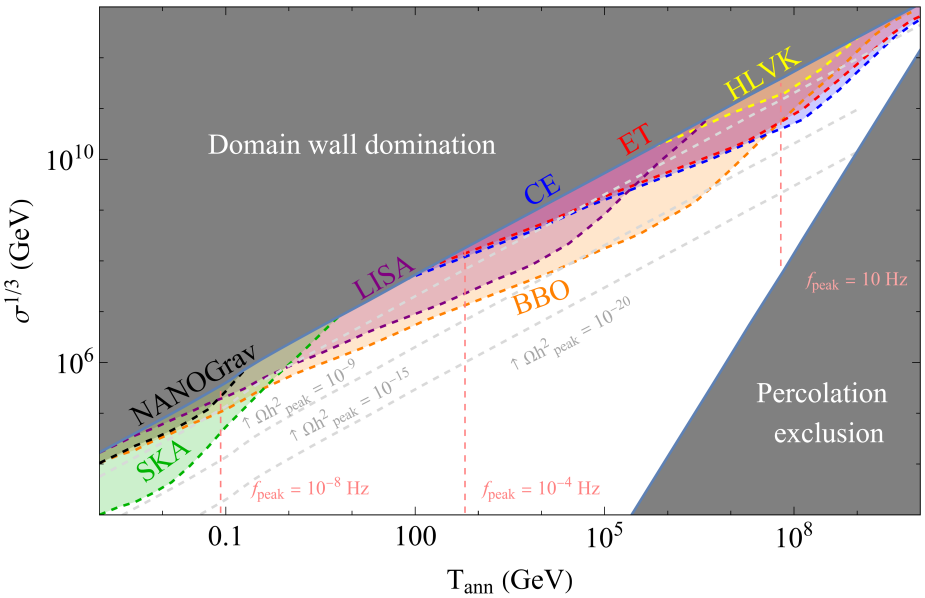

Figure 7.2: The parameter space (T_{ann}, $\sigma^{1/3}$) and the experiments sensitivities. The areas shaded in gray are excluded by the bounds in Equations (7.8) and (7.9). The colored regions represents regions visible to the corresponding experiments. The low frequency range is situated in the lower temperature range (due to $f_{peak} \sim T_{ann}$). NANOGrav [95] and SKA [96] are pulsar timing arrays. LISA [97] and BBO [98] are both future space based interferometes. CE [99], ET [100] and HLVK [101] are ground based interferometer experiments. HLVK consists of a collaboration of the Hanford, LIGO, Virgo and KAGRA detectors. Note that $T_{ann} = 100$ GeV corresponds with looking for domain wall GW signals originating from annihilation around the electroweak phase transition. The dashed gray and pink lines indicate contours of constant peak amplitude and frequency. The Figure is an extension of a similar figure shown in [60].

7.3 Friction domination

We are now ready to evaluate the friction regime and compare the friction length, induced by interactions between (dark) photons and superconducting domain walls, with the Hubble parameter for different values of (T_{ann}, $\sigma^{1/3}$). We iterate over a grid and for every value (T_{ann}, $\sigma^{1/3}$) the friction length at annihilation temperature $T = T_{ann}$ is

calculated and compared with the Hubble scale at annihilation, as in the condition (7.1). This delineates an area in which the friction regime dominates the superconducting domain wall at its annihilation. In this area, the estimates made in the previous section and shown in Figure 7.2, which assumed scaling domination, are no longer valid. On general grounds one expects that in the friction dominated region the gravitational wave signal will be modified and possibly suppressed [81]. More investigation on this effect is necessary and our results about superconducting domain walls provide further motivation to study the gravitational wave signal emitted by friction dominated domain walls in more detail.

The results of this analysis and the friction dominated area can be seen in Figure 7.3. Note that the analysis shown in this chapter assumes interactions between electromagnetic photons and superconducting domain walls. We hence choose a coupling $e = 0.303$ in natural units.
One can observe that the friction indeed makes up a nontrivial part of the parameter space, indicating that the friction regime can not be neglected. Note that the horizontal axis was rescaled to T/vev_ϕ to build a general picture without fixing a vacuum energy. Instead, the ratio $\sigma^{1/3}/vev_\phi$ was chosen to be kept fixed as $\sigma^{1/3}/vev_\phi \approx 1$ (note that the quartic coupling of the field ϕ is set to 1 for simplicity, as mentioned when introducing the Lagrangian (6.1)). We can observe that the friction regime dominates mostly high annihilation temperatures i.e. early annihilation times as can be expected from the early times characteristic to the friction regime (see e.g. Figure 7.1). For these annihilation times the scaling regime did not come to dominate in a sufficiently short time.

All in all, we were able to determine a parameter space sensitive to the influences of the friction regime. As a prediction we can even state that the SKA, NANOGrav, BBO, ET, CE and LISA experiments all have a chance of measuring a spectrum influenced by the friction regime of superconducting domain walls. After predicting where the superconducting domain wall's friction regime is important, we will briefly illustrate some possible theories that can produce superconducting domain walls.

7.4 Summary

This chapter set out to explore the parameters for which friction on superconducting domain walls is still active at their latest gravitational wave emission. To accomplish this, the friction discussion of Chapter 5.3 was refreshed and enhanced by calculating the mean friction length for a specific choice of parameters. This yielded a friction length in function of temperature, which could be compared with the expansion of the Universe, governed by H. Evaluating the friction length and Hubble functions at the annihilation temperature shows whether the domain wall dynamics are dominated by the friction pressure.

By applying this comparison on a complete parameter space, an area was defined in which domain walls maintain the friction regime up to their annihilation. With this information, we can predict that the SKA, NANOGrav, BBO, ET, CE and LISA experiments could be able to measure the fingerprints of friction on the gravitational wave spectrum of early Universe domain walls.

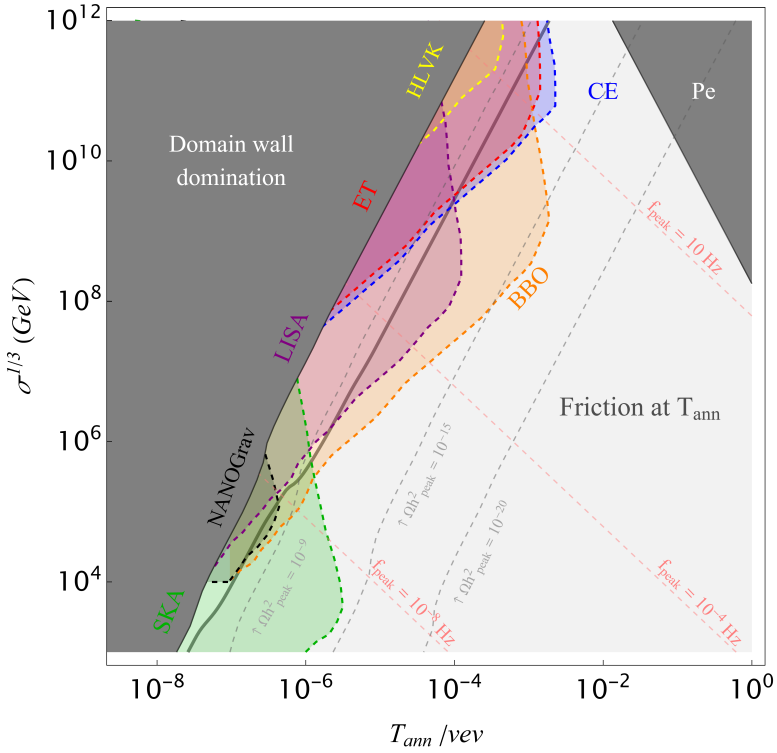

Figure 7.3: The parameter space as shown in Figure 7.2, with the addition of the area in which superconducting domain walls experience friction domination. To avoid fixing a vacuum energy for the ϕ field vev_ϕ, the horizontal axis was rescaled to units T/vev_ϕ. Since we are using the Lagrangian of Equation (6.26), the quartic of ϕ is set to 1. The ratio $\sigma^{1/3}/vev_\phi$ can be found by observing the expression for the tension given in Equation (2.12), this yields approximately 1. The gauge coupling was chosen as the electromagnetic coupling, $e = 0.303$ in natural units. Pe denotes the area excluded by percolation exclusion i.e. the demand that the bias V_{bias} is sufficiently small such that domain walls can form. We can observe that a friction regime induced by photon scattering would be visible to experiments in all frequency ranges, albeit for a particular choice of parameters. Note that the horizontal axis goes up to $T_{ann} = vev_\phi$. Since the temperature at which domain walls form is of order vev_ϕ, annihilation temperatures higher than this would represent domain walls that annihilate before forming.

8 Summary and conclusion

This thesis set out to explore the possibilities of superconducting domain walls.

The first steps in this direction were taken by studying cosmic strings in the early Universe in Chapter 3. Their properties were studied by introducing the simplest case, the global string. A complex scalar field ϕ governed by a global $U(1)$ symmetry served as the building block for such a string to form. The natural lowest energy state of this field is to break the symmetry and take a nonzero vacuum expectation value. By running through its complete phase modulo 2π over a closed loop, the field is forced to assume a zero *vev* at the center of the loop and a string is born. This idea was made concrete by introducing the Mexican hat potential that governs the dynamics of the field ϕ. The equations of motion were calculated and a numerical analysis was applied to solve for the field's profile. The discussion was finished by noting that the energy density of such a system required the introduction of a cutoff to avoid divergence.

After concluding the global string case, the system was generalised to couple with a $\tilde{U}(1)$ gauge field $\tilde{A}^\mu$. This could be motivated by noting that the dynamics of the gauge field offset the divergence of the string's energy. Hence, a local string setup is stable without the need for a cutoff. The same procedures were followed as the global string discussion. The same potential was used and the Lagrangian was supplemented by the covariant derivative and the dynamics of the gauge fields. The equations of motion were calculated and, by applying a correct ansatz, they were reduced to a system of one dimensional, second order differential equations. The numerical analysis was generalised to compute the field profile's of both the scalar field and the gauge field. These results confirmed the expected behaviour of both fields. The local string section ended with a brief discussion on their properties e.g. string width and energy density.

Chapter 3's final section was focused on the behaviour of strings in the early Universe. Their formation mechanism was briefly illustrated.

Chapter 4 aimed to generalise the model even further. Another complex scalar field σ under a $U(1)$ symmetry was introduced, which coupled to the original field ϕ. The goal was finding solutions in which ϕ takes its string profile and σ takes a zero *vev* everywhere except inside the string core, in which it breaks the $U(1)$ symmetry. Hence it was named a condensate.

We introduced the Lagrangian for this configuration and spend time to elaborate on the conditions the parameters must obey to yield the desired field profiles. After these conditions were set the remainder of the discussion assumed them to be satisfied. The question whether such a setup was stable was answered by performing a perturbation analysis on the condensate field σ. We found that the superconducting string is indeed stable when the parameters of the Lagrangian satisfy an extra condition.

With the system and its conditions defined, the superconductivity could be explored. This was done in three steps; looking for a persistent current, proving the Meissner effect and looking for a mechanism to charge the strings. The persistent current was

recreated according to the arguments made by Witten in [7]. Using the formalism of electromagnetism, it was shown that a dampening of external fields takes place in the superconducting string setup. A charging mechanism was identified to produce a current on superconducting strings in the early Universe cosmic plasma. To conclude this discussion, the solutions to the equations of motion were numerically computed.

These chapters concluded the discussion on strings and superconducting strings. We set the goal of applying the same formalism to domain walls. In Chapter 5, the domain wall configuration was theoretically built, together with a discussion on the potential and the parameters of the model. The general properties were discussed and a numerical analysis was applied to solve the equations of motion. We also introduced a possible force acting on the domain wall in the early Universe due to interactions with the thermal plasma. This friction regime is important since its physics are non-trivial and being able to neglect friction is not guaranteed.

To couple domain walls to experimentally measurable quantities, their gravitational wave signal was discussed. This spectrum was explained and approximated as a piecewise function of power laws. Both the friction and gravitational wave signal become important later in Chapter 7.

Hence we arrive at the central goal of this thesis, building a model which allows for domain wall solutions that can behave like superconductors. To achieve this a model was introduced in which domain wall solutions were coupled to a complex scalar field coupled to a $U(1)$ symmetry, called the condensate field. The idea is that the condensate takes nonzero values inside the domain wall, breaking the $U(1)$ symmetry. Chapter 6 elaborates on this configuration and defines an effective theory to model the condensate behaviour on the domain wall. It is shown that this model indeed leads to superconducting effects, in particular the Meissner effect and a charging mechanism.

The remainder of the chapter is devoted to calculating the reflection of (dark) photons on a superconducting domain wall. This is important, both to model the charging mechanism and to predict for what parts of parameter space the friction regime cannot be neglected.

This leads to the final chapter. Chapter 7 aims to calculate when friction dominates the dynamics of superconducting domain walls by comparing the friction with the expansion of the Universe.

The parameter space of gravitational waves was mapped to predict the sensitivities of several current and future experiments. To supplement this parameter space, the friction calculations were used to predict what parts of this space will be affected by the friction regime. We were able to predict that experiments such as SKA, NANOGrav, ET, CE, LISA and BBO could measure a signal that is affected by friction.

Outlook The subject of superconducting domain walls and friction is far from exhausted. We have shown that friction can be relevant for domain wall dynamics and can potentially affect the gravitational wave spectrum. The detailed characterization of the effect of friction on the gravitational wave signal is still an open research area.

In calculating the charging mechanism of a domain wall in Chapter 6, we mention that only a fraction of an external electric field can penetrate as to charge the domain wall. This ratio was linked to the transmission coefficient. Further investigation is needed to confirm this estimate and the mechanism under which the superconducting domain walls can get charged in the early Universe. Observing this mechanism more closely and explicitly calculating this fraction could make for an interesting research topic.

Additionally we did not investigate the procedures of defining a persistent current for superconducting domain walls. The geometry of closing the walls in such a way as to define a persistent current could make for interesting research in the field of topology.

An important question that remains is the symmetry groups generating these superconducting domain walls. Many of Beyond the Standard Model (BSM) symmetry groups and theories are able to generate and break the discrete symmetries to generate domain walls, the subtleties lie in what $U(1)$ symmetry governs the condensate.

In particular, the friction calculation in this thesis is performed assuming the domain wall interacts with the Standard Model (SM) photons. This was chosen as an illustrative case to show the importance of friction on the parameter space of the model. Note however, that in periods before the electroweak phase transition ($T \sim 100$ GeV) the electromagnetic symmetry group, $U(1)_{EM}$, is embedded in the electroweak symmetry group, $SU(2)_L \times U(1)_Y$. In this regime, the friction on superconducting domain walls could be induced by particles charged under the hypercharge. More generally our scenario of superconducting domain walls could instead involve a new $U(1)$ gauge group extending the SM symmetry group. This is a type of dark radiation.

In general, there can exist many Beyond the Standard Model theories that exhibit the required Z_2 and $U(1)$ symmetries needed to generate superconducting domain walls. As an illustrative example, we consider the Two Higgs Doublet Model (2HDM), as described in [102].

This model introduces a second complex scalar Higgs doublet to the standard model. The model exhibits 5 physical scalars, two of which behave like the known Higgs particle of the standard model. The vacua state of these two particles exhibits a Z_2 symmetry, which is broken as the Universe cools down. This breaking of a discrete symmetry can lead to the formation of domain walls, as described in Section 5.2. One of the Higgs scalars can tend to a domain wall solution. This leaves the other Higgs scalar to assume the role of the condensate. In a certain region of parameter space it could occur that this model leads to the formation of superconducting domain walls [102], even if more investigations are needed given the complexity of the model and the possible field configurations.

This discussion was intentionally kept brief. The study of Beyond the Standard

model physics is an extensive research field and the detailed model building which can lead to superconducting domain wall formation goes beyond the scope of this thesis. This short example serves to connect the theoretical ideas presented in this work with the particle content of the early Universe.

In conclusion the field of superconducting domain walls is still very much open to further research. To obtain a complete and rigorous model of their dynamics, properties and gravitational wave signals, more research will be needed.

In this thesis we have performed the first step to unraveling the rich dynamics and phenomenology of these extended defects.

A Sensitivity Curves

This appendix aims to elaborate on the sensitivity curves of the GW ewperiments. These curves act as a tool to determine whether a GW signal would be detectable by the experiment.

This particular discussion will be focused on detecting gravitational waves from early universe phase transitions with the goal to use these sensitivity curves to predict what parameter space of the domain wall gravitational wave spectrum is observable for several different experiments.

Most of what is handled in this appendix can be found in [41], which is a great review of the topic and includes several currently relevant examples. The calculations and concepts in this appendix are based on [103] in which the sensitivities of Laser Interferometer Space Antenna (LISA) are explored.

The gravitational wave spectrum is defined as

$$h^2\Omega_{GW}(t,f) \coloneqq \frac{h^2}{\rho_c(t)}\frac{d\rho_{GW}(t)}{d\ln(f)}, \tag{A.1}$$

in which h denotes the reduced Hubble parameter $h = (H_0/100)\frac{\text{km}}{\text{s}}/\text{Mpc}$. Hence the spectrum represents the fractional energy density of gravitational waves over the total critical density of the universe at a time t per logarithmic frequency [22].

The quantity that defines whether a signal is visible is the Signal-to-Noise Ratio (SNR). A higher SNR allows for the signal to be detected clearly within the background of detector noise. This noise consists of effects like quantum effects in the interferometer mirrors [104, 105].

A formal definition of the SNR in terms of the energy density spectra is

$$\text{SNR} = \sqrt{\Delta t \int_{f_{min}}^{f_{max}} df \left(\frac{\Omega_{GW}(f)}{\Omega_s(f)}\right)^2}, \tag{A.2}$$

in which Δt denotes the detection time and $[f_{min}, f_{max}]$ is the frequency range in which the experiment can detect signals. The quantity $\Omega_s(f)$ is the output energy density spectrum of the detector noise.

A Power Law Sensitivity curve (PLS) can now be defined by parameterising the spectrum of the incoming gravitational waves as

$$\Omega_{GW}(f) = C_\beta f^\beta \tag{A.3}$$

and demanding a minimum signal to noise ratio that need be satisfied. For a choice of β one can calculate

$$\mathrm{SNR}_{\mathrm{min}} = \sqrt{\Delta t \int_{f_{min}}^{f_{max}} df \left(\frac{C_\beta f^\beta}{\Omega_s(f)} \right)^2} \tag{A.4}$$

for a given detector and detection time. The noise spectrum Ω_s will depend on what detector is under investigation. The only parameter left to find is C_β, which is determined by Equation A.4. In other words, for every possible power law f^β, a coefficient C_β is determined for which the power law signal would be sufficiently visible in the detector.

After performing these calculations for a sufficiently large set of β's (both negative and positive), one can combine all the curves found and pick at each frequency the maximum. In this manner a curve is obtained above which any power law signal would be larger than the given SNR_{min}. Examples for several GW detectors are included in Figure A.1.

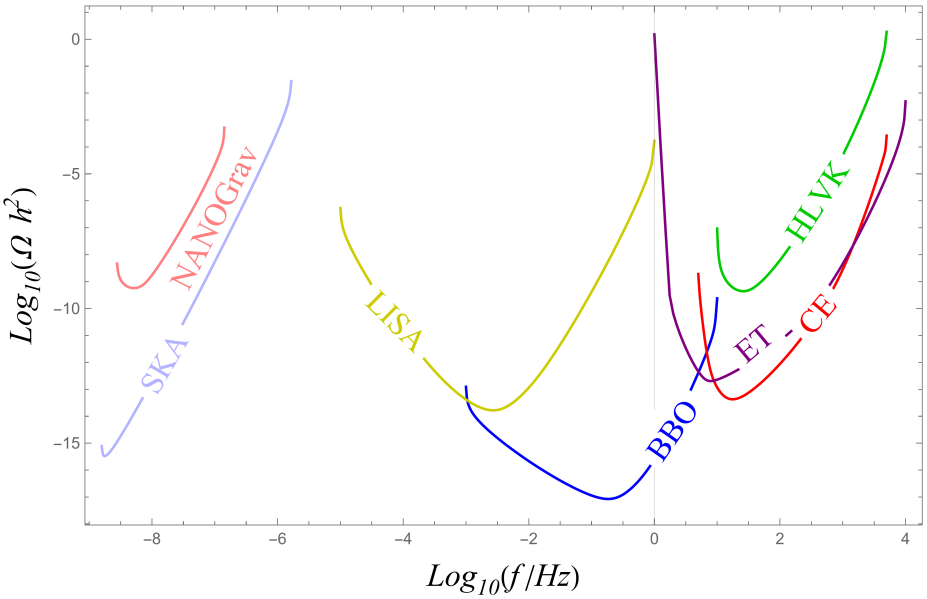

Figure A.1: Sensitivity curves of important GW experiments plotted on a log-log scale. These curves were constructed in [41]. One can see the different frequency ranges to which current and future experiments are sensitive.

B Numerical methods

Throughout the thesis two numerical methods were used. One to calculate the field profiles of superconducting topological defects and the other to calculate a reflection coefficient given a potential in a scattering problem. This appendix aims to explain both methods to provide an insight into the workings behind numerically found plots.

B.1 String and domain wall profiles

Throughout Chapter 4 and 6, a numerical method is used to calculate the field profiles of both superconducting strings and superconducting domain walls. This appendix aims to elaborate on the method used to solve the equations of motion.

The equations of motion to be solved are second order ordinary differential equations. These can be solved by utilising a relaxation method. One starts with a guess for the field profiles that satisfies the boundary conditions of the problem. After this the guess can be updated step by step. The way these steps are taken is determined by the discretised differential equation. At each step the boundary conditions are re-imposed. When the steps change the profiles less than a preset accuracy the algorithm stops and the final form of the field profiles should agree with the solution to the differential equation. This method was based on [106] and will by outlined below.

The method will be illustrated by considering a general equation of motion for a field ϕ,

$$\nabla^2\phi - \partial_\phi V = 0. \tag{B.1}$$

The field ϕ is assumed to be static since this is true for the fields when applying the method in the thesis. One can define a measure of how much a field Φ does not agree with this equation as

$$\nabla^2\Phi - \partial_\Phi V = \mathcal{R}. \tag{B.2}$$

$\mathcal{R}$ is called the residual. A normal relaxation scheme would define a coordinate grid and make a guess for the field ϕ at each grid point. After this, the code can iterate over each point and update the guess to satisfy Equation (B.1). Instead we implement a discretised. As an example consider the field ϕ to only depend on x. The derivative can be discretised using a Taylor series expansion

$$\phi(x+h) = \phi(x) + \phi'(x)h + \phi''(x)\frac{h^2}{2} + O(h^3). \tag{B.3}$$

such that

$$\partial_x^2\phi = \frac{\phi(x+h) + \phi(x-h) - 2\phi(x)}{h^2}. \tag{B.4}$$

in which h is the distance between grid points. Plugging this into the equation of motion (B.1) yields

$$\phi(x) = \frac{\phi(x+h) + \phi(x-h) - h^2 \partial_\phi V}{2} \tag{B.5}$$

at a grid point on coordinate x. Hence one can sweep across the grid and update each point with formula (B.5).

A more sophisticated method can parameterise this updating, choosing how "far" the guess can evolve. In order to achieve this, a new coordinate s can be defined. One can then rewrite the residual as

$$\mathcal{R} = \frac{d\Phi}{ds}. \tag{B.6}$$

The problem is in essence rewritten to a system looking to evolve to a steady state $\frac{d\Phi}{ds} = 0$,

$$\frac{d\Phi}{ds} = \nabla^2 \Phi - \partial_\Phi V. \tag{B.7}$$

On a spatial grid with seperations h, this equation can be discretised. The derivative over the step coordinate can also be discretised. The distance between steps will be denoted as Δs. As an example a grid over the $xy-$plane will be considered. A field at coordinates (s, x, y) will be denoted as $\Phi^n_{i,j}$. Increments of h or Δs will be denoted by a ± 1 e.g. $\Phi(s + \Delta s, x + h, y - h) = \Phi^{n+1}_{i+1,j-1}$, allowing us to rewrite Equation (B.7).

$$\frac{\Phi^{n+1}_{i,j} - \Phi^n_{i,j}}{\Delta s} = \frac{\Phi^n_{i+1,j} + \Phi^n_{i-1,j} + \Phi^n_{i,j+1} + \Phi^n_{i,j-1} - 4\Phi^n_{i,j}}{h^2} - \partial_\Phi V \tag{B.8}$$

which can be rewritten to an expression for the time step at coordinates (i, j)

$$\Phi^{n+1}_{i,j} = \frac{\Delta s}{h^2} \left(\Phi^n_{i+1,j} + \Phi^n_{i-1,j} + \Phi^n_{i,j+1} + \Phi^n_{i,j-1} - 4\Phi^n_{i,j} - h^2 \partial_\Phi V \right) + \Phi^n_{i,j}. \tag{B.9}$$

The quantity $\frac{\Delta s}{h^2} \coloneqq \zeta$ parameterises the time steps. The smaller ζ, the more detailed the model. This comes at a cost of speed. Both the choice of h and ζ need to be balanced between accuracy and efficiency.

By discretising the equations of motion and applying equations like (B.9) until a certain accuracy is achieved, one obtains the profiles shown in Chapter 4 and 6. The accuracy ε is defined as the maximum difference of all points between the time steps

$$\varepsilon = \max \left(\Phi^n_{i,j} - \Phi^{n-1}_{i,j} \quad \forall (i,j) \in \text{grid} \right) \tag{B.10}$$

If a system of equations is being solved the accuracy is defined as the maximum of all field accuracies. This thesis demands an accuracy of $\varepsilon < 10^{-6}$ before accepting the results of the relaxtion algorithm.

This concludes the Appendix section on the numerical relaxation method used in the thesis. The equations of motion were discretised and a step coordinate s was introduced to parameterise the relaxation steps. By interpreting the problem as a system relaxing to a steady state, an algorithm could be build to implent in the thesis.

B.2 Reflection coeficient

In the later part of the thesis, the reflection coefficient of a Schrödinger equation scattering problem is required to further advance both the analogy with the Witten Superconducting strings in Chapter 4 and the pressure acting on the superconducting domain walls of Chapter 6. While in some cases an analytical solution can be found, ** a numerical solution allows for solving more general potentials and even the numerical potentials found by relaxing the DW profile, the numerics of which are described in the previous Section B.1. The numerical methods described in this Section can be found in [107]

The starting point for the analysis is the Schrödinger equation:

$$(-\frac{d^2}{dz^2} + V(z))\psi(z) = k^2\psi(z) \tag{B.11}$$

The use of the z coordinate is simply to remain in analogy to the Schrödinger equations eventually found in the DW calculations. V(z) is the potential, while k denotes the wave number.

The general idea of the analysis is defining the potential as a piecewise function: a constant region before the barrier, the barrier itself and a constant region after the potential. This indicates that any potential will have to be simplified to an extent by demanding that outside a region $[a, b]$, the potential behaves as a constant.

$$V(z) = \begin{cases} V_1 & z \in (-\infty, a) \\ V_0(z) & z \in [a, b] \\ V_2 & z \in (b, \infty) \end{cases} . \tag{B.12}$$

In the regions $(-\infty, a)$ and (b, ∞) the equation is easy to solve and takes on exponential solutions. The solution in the region $[a, b]$ is not obvious and maybe not even analytically solvable. Since the equation is a second order differential equation, the general solution can be written as a linear combination of two specific solution $\psi_1(z)$ and $\psi_2(z)$.

**as is the case for the δ and sech^2 potential.

$$\psi(z) = \begin{cases} e^{ik_1(z-a)} + A_R e^{-ik_1(z-a)} & z \in (-\infty, a) \\ c_1\psi_1(z) + c_2\psi_2(z) & z \in [a, b] \\ A_T e^{ik_2(z-b)} & z \in (b, \infty) \end{cases} \tag{B.13}$$

Note that these solutions assume a wave incoming from $z \to -\infty$ in the normalized form $\psi(z) = e^{ik_1(z-a)}$. The reflection amplitude A_R and transmission amplitude A_T are denoting the amplitudes of the wave that bounced on the barrier and the wave that is transmitted.

Demanding continuity on the boundaries $z = a$ and $z = b$ for both $\psi(z)$ and its derivative $\psi'(z)$, allows for solving this system to A_R and A_T. Following [107], we assume that the solutions ψ_1 and ψ_2 satisfy the following conditions,

$$\begin{aligned} \psi_1(a) = 1, \quad \psi_1'(a) = 0, \\ \psi_2(a) = 0, \quad \psi_2'(a) = 1. \end{aligned} \tag{B.14}$$

Solving the system yields expression for R and T:

$$A_R = \frac{\psi_1'(b) + k_2 k_1 \psi_2(b) + i[k_1\psi_2'(b) - k_2\psi_1(b)]}{k_2 k_1 \psi_2(b) - \psi_1'(b) + i[k_2\psi_1(b) + k_1\psi_2'(b)]]} \tag{B.15}$$

$$A_T = [(1 + R)\psi_1(b) + ik_1(1 - R)\psi_2(b)] \tag{B.16}$$

The reflection coefficient R is now given by the reflection amplitude squared

$$R = A_R^2, \tag{B.17}$$

$$T = A_T^2. \tag{B.18}$$

C Friction derivations

This appendix elaborates on the calculations leading up to the formulas used in Section 5.3. The formulas leading up to the criterion for which friction enters the equation of motion and the expression for the friction pressure ΔP will be discussed. It is not the goal of this appendix to reconstruct the calculations, rather to give the intuitive steps leading up to an expression for ΔP. The interested reader can consult the derivations in detail in [81], on which this appendix is based.

A domain wall can be approximated as a two dimensional object when its width is small in the dimensions of the problem discussed. The domain wall will be considered to be perpendicular tot the $z-$axis. The dynamics of such a two dimensional object are described by considering its three dimensional worldvolume coordinates[††],

$$x^\mu = x^\mu(\zeta^a), \tag{C.1}$$

in which ζ^α denotes the coordinates of the world volume. The structure of the world-volume is dependent on its imposed metric

$$\gamma_{ab} = g_{\mu\nu}\frac{\partial x^\mu}{\partial \zeta^a}\frac{\partial x^\nu}{\partial \zeta^b}. \tag{C.2}$$

$g_{\mu\nu}$ is the flat FLRW metric. The action governing the dynamics is [11]

$$S = -\sigma \int d^3\zeta \sqrt{\gamma}. \tag{C.3}$$

γ represents the determinant of the metric γ_{ab}. σ is the domain wall tension.

Solving the action of Equation (C.3) for its equations of motion in the gauge $\zeta_0 = \tau$, with τ the conformal time, yields

$$\sigma\frac{1}{\sqrt{\gamma}}\frac{\partial}{\partial\zeta^a}\left(\sqrt{\gamma}\gamma^{ab}\partial_{\zeta^i}x^\mu\right) + \sigma\Gamma^\mu{}_{\nu\sigma}\gamma^{ab}\partial_{\zeta^a}x^\nu\partial_{\zeta^b}x^\sigma = 0. \tag{C.4}$$

These equations are modified to include friction by implementing a force [93].

$$F^\nu = \frac{\sigma}{l_f}(u^\nu - \partial_{\zeta^a}x^\nu\gamma^{ab}\partial_{\zeta^b}x^\mu g_{\mu\sigma}u^\sigma). \tag{C.5}$$

u represents the velocity of the particles causing the friction with the domain wall. l_f is a parameterization, which we will later identify as the friction length. The equation of motion for the time component can be further derived and yields

[††]Just like a particle has a worldline and a string has a two dimensional worldsheet.

$$\ddot{x} + \left(3\frac{\dot{a}}{a^2} + \frac{1}{l_f}\right)(1-\dot{x}^2)a\dot{x} = \frac{1}{\epsilon}\frac{\partial}{\partial\zeta^1}\left(\left(\partial_{\zeta^2}x\right)^2\frac{\partial_{\zeta^1}x}{\epsilon}\right) + \frac{1}{\epsilon}\frac{\partial}{\partial\zeta^2}\left(\left(\partial_{\zeta^1}x\right)^2\frac{\partial_{\zeta^2}x}{\epsilon}\right). \quad \text{(C.6)}$$

The important term here is $\left(3\frac{\dot{a}}{a^2} + \frac{1}{l_f}\right) = \left(3H + \frac{1}{l_f}\right)$. Which shows that friction is to be taken into account for describing a domain walls dynamics when $\frac{1}{l_f} \gtrsim 3H$.

In the domain walls rest frame, the force (C.5) can be rewritten as

$$F^i = -\frac{\sigma}{l_f}\frac{v^i}{\sqrt{1-v^2}}. \quad \text{(C.7)}$$

This force can be calculated by considering the pressure the particles in the cosmic plasma exert on the domain wall. This is governed by their Bose Einstein/Fermi Dirac, distribution $f(v)$ depending on whether they are bosons or fermions, their velocity w.r.t. the wall $\frac{p_z}{E}$, the momentum exchange with the wall $2p_z$ and the probability of interaction $\mathcal{R}(p)$. The pressure exerted from particles incoming from $z \to +\infty$ is given by

$$P_R = \int \frac{d^2p}{(2\pi)^3}\int_{-\infty}^{0} dp_z \frac{p_z}{E}(2p_z)f(v)\mathcal{R}(p). \quad \text{(C.8)}$$

The difference in pressure over the wall is then $\Delta P = P_R - P_L$, where P_L is the pressure from particles incoming from $z \to -\infty$.

Approximating this in the low velocity and Boltzmann statistics limit yields an expression for the pressure difference.

$$\Delta P \approx v\frac{g}{\pi^2}\int_0^\infty dp_z p_z^3 \mathcal{R}(p_z)\exp\left(-\frac{\sqrt{m^2+p_z^2}}{T}\right), \quad \text{(C.9)}$$

where g denotes the degrees of freedom of the particles interacting with the wall. This is the final formula which is used in the thesis, concluding this appendix.

References

[1] The LIGO Scientific Collaboration and the Virgo Collaboration. "Observation of Gravitational Waves from a Binary Black Hole Merger". In: *Physical Review Letters* 116.6 (Feb. 2016). DOI: 10.1103/PhysRevLett.116.061102. arXiv: 1602.03837v1. URL: http://arxiv.org/abs/1602.03837%20http://dx.doi.org/10.1103/PhysRevLett.116.061102.

[2] Michael Edward Peskin and Daniel V. Schroeder. *An Introduction to Quantum Field Theory*. Reading, USA: Addison-Wesley (1995) 842 p. Westview Press, 1995.

[3] John R. Ellis et al. "Supersymmetric Relics from the Big Bang". In: *Nucl. Phys. B* 238 (1984). Ed. by M. A. Srednicki, pp. 453–476. DOI: 10.1016/0550-3213(84)90461-9.

[4] Apostolos Pilaftsis. "Heavy Majorana neutrinos and baryogenesis". In: *Int. J. Mod. Phys. A* 14 (1999), pp. 1811–1858. DOI: 10.1142/S0217751X99000932. arXiv: hep-ph/9812256.

[5] Abdelhak Djouadi. "The Anatomy of electro-weak symmetry breaking. II. The Higgs bosons in the minimal supersymmetric model". In: *Phys. Rept.* 459 (2008), pp. 1–241. DOI: 10.1016/j.physrep.2007.10.005. arXiv: hep-ph/0503173.

[6] T. Kobayashi. "Experimental verification of the standard model of particle physics." In: *Proceedings of the Japan Academy. Series B, Physical and biological sciences* 97(5) (20021), pp. 211–235. DOI: https://doi.org/10.2183/pjab.97.013.

[7] Edward Witten. "Superconducting Strings". In: *Nucl.Phys.B* 249.4 (Feb. 1985), pp. 557–592. ISSN: 05503213. DOI: 10.1016/0550-3213(85)90022-7.

[8] W. de Boer. "Grand unified theories and supersymmetry in particle physics and cosmology". In: *Prog. Part. Nucl. Phys.* 33 (1994), pp. 201–302. DOI: 10.1016/0146-6410(94)90045-0. arXiv: hep-ph/9402266.

[9] J. M. D. Coey. *Magnetism and Magnetic Materials*. Cambridge University Press, 2010. DOI: 10.1017/CBO9780511845000.

[10] Mathias Kläui. *Flipping a domain wall switch*. Accessed on 24/05/2023. 2008. URL: https://physics.aps.org/articles/v1/17.

[11] A. (Alexander) Vilenkin and E. P. S. (E. Paul S.) Shellard. "Cosmic Strings and Other Topological Defects". In: (2000), p. 517.

[12] Michael Kachelriess. "Phase transitions and topological defects". In: *Quantum Fields: From the Hubble to the Planck Scale*. Oxford University Press, Oct. 2017. ISBN: 9780198802877. DOI: 10.1093/oso/9780198802877.003.0016. eprint: https://academic.oup.com/book/0/chapter/195372166/chapter-pdf/46467425/oso-9780198802877-chapter-16.pdf. URL: https://doi.org/10.1093/oso/9780198802877.003.0016.

[13] Tom Lancaster and Stephen J Blundell. *Quantum field theory for the gifted amateur*. Oxford: Oxford University Press, 2014. DOI: 0199699321. URL: https://cds.cern.ch/record/1629337.

[14] Steven Weinberg. "Gauge and Global Symmetries at High Temperature". In: *Phys. Rev. D* 9 (1974), pp. 3357–3378. DOI: 10.1103/PhysRevD.9.3357.

[15] L. Dolan and R. Jackiw. "Symmetry Behavior at Finite Temperature". In: *Phys. Rev. D* 9 (1974), pp. 3320–3341. DOI: 10.1103/PhysRevD.9.3320.

[16] D. A. Kirzhnits and Andrei D. Linde. "Symmetry Behavior in Gauge Theories". In: *Annals Phys.* 101 (1976), pp. 195–238. DOI: 10.1016/0003-4916(76)90279-7.

[17] J. I. Kapusta and Charles Gale. *Finite-temperature field theory: Principles and applications*. Cambridge Monographs on Mathematical Physics. Cambridge University Press, 2011. ISBN: 978-0-521-17322-3, 978-0-521-82082-0, 978-0-511-22280-1. DOI: 10.1017/CBO9780511535130.

[18] Mariano Quiros. "Finite temperature field theory and phase transitions". In: *ICTP Summer School in High-Energy Physics and Cosmology*. Jan. 1999, pp. 187–259. arXiv: hep-ph/9901312.

[19] T. W. B. Kibble. "Topology of Cosmic Domains and Strings". In: *J. Phys. A* 9 (1976), pp. 1387–1398. DOI: 10.1088/0305-4470/9/8/029.

[20] H. Poincaré. "Sur la dynamique de l' électron". In: (). URL: https://www.academie-sciences.fr/pdf/dossiers/Poincare/Poincare_pdf/Poincare_CR1905.pdf.

[21] Joel M. Weisberg, Joseph H. Taylor, and Lee A. Fowler. "Gravitational Waves from an Orbiting Pulsar". In: *Scientific American* 245.4 (Oct. 1981), pp. 74–82. ISSN: 0036-8733. DOI: 10.1038/SCIENTIFICAMERICAN1081-74. URL: https://www.scientificamerican.com/article/gravitational-waves-from-an-orbitin/.

[22] Michele Maggiore. "Gravitational Waves (Volume I)". In: *Oxford University Press* 53.9 (2007), pp. 197–210. ISSN: 1098-6596.

[23] Craig Cahillane and Georgia Mansell. "Review of the Advanced LIGO Gravitational Wave Observatories Leading to Observing Run Four". In: *Galaxies* 10.1 (2022), p. 36. DOI: 10.3390/galaxies10010036. arXiv: 2202.00847 [gr-qc].

[24] Nelson Christensen. "Stochastic Gravitational Wave Backgrounds". In: (). arXiv: 1811.08797v1.

[25] Chiara Caprini and Daniel G. Figueroa. "Cosmological Backgrounds of Gravitational Waves". In: *Class. Quant. Grav.* 35.16 (2018), p. 163001. DOI: 10.1088/1361-6382/aac608. arXiv: 1801.04268 [astro-ph.CO].

[26] P. A. R. Ade et al. "Planck 2015 results. XIII. Cosmological parameters". In: *Astron. Astrophys.* 594 (2016), A13. DOI: 10.1051/0004-6361/201525830. arXiv: 1502.01589 [astro-ph.CO].

[27] B. P. Abbott et al. "GW170817: Observation of Gravitational Waves from a Binary Neutron Star Inspiral". In: *Physical Review Letters* 119.16 (Oct. 2017), p. 161101. ISSN: 10797114. DOI: 10.1103/PHYSREVLETT.119.161101/FIGURES/5/MEDIUM. URL: https://journals.aps.org/prl/abstract/10.1103/PhysRevLett.119.161101.

[28] Scott Dodelson and Fabian Schmidt. "Modern Cosmology, Second Edition". In: *Modern Cosmology, Second Edition* (Jan. 2020), pp. 1–494. DOI: 10.1016/C2017-0-01943-2. URL: http://www.sciencedirect.com:5070/book/9780128159484/modern-cosmology.

[29] Leonardo Senatore. "Lectures on Inflation". In: (). arXiv: 1609.00716v1.

[30] Julien Lesgourgues. "TASI Lectures on Cosmological Perturbations". In: (Feb. 2013). arXiv: 1302.4640. URL: https://arxiv.org/abs/1302.4640v1.

[31] Satoshi Iso, Pasquale D. Serpico, and Kengo Shimada. "QCD-Electroweak First-Order Phase Transition in a Supercooled Universe". In: *Physical Review Letters* 119.14 (Oct. 2017), p. 141301. ISSN: 10797114. DOI: 10.1103/PHYSREVLETT.119.141301/FIGURES/4/MEDIUM. arXiv: 1704.04955. URL: https://journals.aps.org/prl/abstract/10.1103/PhysRevLett.119.141301.

[32] Djuna Croon et al. "GUT Physics in the era of the LHC". In: *Frontiers in Physics* 7.JUN (Mar. 2019). DOI: 10.3389/fphy.2019.00076. arXiv: 1903.04977v2. URL: http://arxiv.org/abs/1903.04977%20http://dx.doi.org/10.3389/fphy.2019.00076.

[33] Marc Kamionkowski, Arthur Kosowsky, and Michael S. Turner. "Gravitational radiation from first-order phase transitions". In: *Physical Review D* 49.6 (1994), pp. 2837–2851. ISSN: 05562821. DOI: 10.1103/PHYSREVD.49.2837.

[34] Pau Amaro-Seoane et al. "Laser Interferometer Space Antenna". In: (Feb. 2017). arXiv: 1702.00786. URL: https://arxiv.org/abs/1702.00786v3.

[35] ESA. *ESA Science & Technology - Mission Summary*. URL: https://sci.esa.int/web/lisa/-/61367-mission-summary (visited on 04/24/2023).

[36] B. P. Abbott et al. "GW150914: Implications for the stochastic gravitational-wave background from binary black holes". In: *Physical Review Letters* 116.13 (Mar. 2016), p. 131102. ISSN: 10797114. DOI: 10.1103/PHYSREVLETT.116.131102/FIGURES/2/MEDIUM. arXiv: 1602.03847. URL: https://journals.aps.org/prl/abstract/10.1103/PhysRevLett.116.131102.

[37] B P Abbott. "GW170817: Implications for the Stochastic Gravitational-Wave Background from Compact Binary Coalescences". In: *Physical Review Letters* 120 (2018). DOI: 10.1103/PhysRevLett.120.091101.

[38] R. Abbott et al. "Upper limits on the isotropic gravitational-wave background from Advanced LIGO and Advanced Virgo's third observing run". In: *Phys. Rev. D* 104.2 (2021), p. 022004. DOI: 10.1103/PhysRevD.104.022004. arXiv: 2101.12130 [gr-qc].

[39] Travis Robson, Neil J. Cornish, and Chang Liu. "The construction and use of LISA sensitivity curves". In: *Class. Quant. Grav.* 36.10 (2019), p. 105011. DOI: 10.1088/1361-6382/ab1101. arXiv: 1803.01944 [astro-ph.HE].

[40] B. Sathyaprakash et al. "Scientific Objectives of Einstein Telescope". In: *Class. Quant. Grav.* 29 (2012). Ed. by Mark Hannam et al. [Erratum: Class.Quant.Grav. 30, 079501 (2013)], p. 124013. DOI: 10.1088/0264-9381/29/12/124013. arXiv: 1206.0331 [gr-qc].

[41] Kai Schmitz. "New Sensitivity Curves for Gravitational-Wave Signals from Cosmological Phase Transitions". In: *JHEP* 01 (2021), p. 097. DOI: 10.1007/JHEP01(2021)097. arXiv: 2002.04615 [hep-ph].

[42] Zaven Arzoumanian et al. "The NANOGrav 12.5 yr Data Set: Search for an Isotropic Stochastic Gravitational-wave Background". In: *Astrophys. J. Lett.* 905.2 (2020), p. L34. DOI: 10.3847/2041-8213/abd401. arXiv: 2009.04496 [astro-ph.HE].

[43] P. A.R. Ade et al. "Planck early results. I. The Planck mission". In: *Astronomy & Astrophysics* 536 (Dec. 2011), A1. ISSN: 0004-6361. DOI: 10.1051/0004-6361/201116464. arXiv: 1101.2022. URL: https://www.aanda.org/articles/aa/full%7B%5C_%7Dhtml/2011/12/aa16464-11/aa16464-11.html%20https://www.aanda.org/articles/aa/abs/2011/12/aa16464-11/aa16464-11.html.

[44] Planck Collaboration et al. "Planck 2015 results. XIII. Cosmological parameters". In: 594, A13 (Sept. 2016), A13. DOI: 10.1051/0004-6361/201525830. arXiv: 1502.01589 [astro-ph.CO].

[45] R. K. Sachs et al. "Perturbations of a Cosmological Model and Angular Variations of the Microwave Background". In: *ApJ* 147 (Jan. 1967), p. 73. ISSN: 0004-637X. DOI: 10.1086/148982. URL: https://ui.adsabs.harvard.edu/abs/1967ApJ...147...73S/abstract.

[46] B. J. Carr. "Cosmological gravitational waves - Their origin and consequences". In: 89.1-2 (Sept. 1980), pp. 6–21.

[47] Richard H. Cyburt et al. "New BBN limits on physics beyond the standard model from ^4He". In: *Astropart. Phys.* 23 (2005), pp. 313–323. DOI: 10.1016/j.astropartphys.2005.01.005. arXiv: astro-ph/0408033.

[48] London F. and London H. "The electromagnetic equations of the supraconductor". In: *Proc. R. Soc. Lond.* A14971–88 (1935). DOI: https://doi.org/10.1098/rspa.1935.0048.

[49] Rainer Wesche. "High-Temperature Superconductors". In: *Springer Handbook of Electronic and Photonic Materials*. Ed. by Safa Kasap and Peter Capper. Cham: Springer International Publishing, 2017, pp. 1–1. ISBN: 978-3-319-48933-9. DOI: 10.1007/978-3-319-48933-9_50. URL: https://doi.org/10.1007/978-3-319-48933-9_50.

[50] J. Bardeen, L. N. Cooper, and J. R. Schrieffer. "Microscopic Theory of Superconductivity". In: *Phys. Rev.* 106 (1 Apr. 1957), pp. 162–164. DOI: 10.1103/PhysRev.106.162. URL: https://link.aps.org/doi/10.1103/PhysRev.106.162.

[51] Bertrand Damien. "A relativistic BCS theory of superconductivity: an experimentally motivated study of electric fields in superconductors". Prom.: Govaerts, Jan, http://hdl.handle.net/2078.1/5380. PhD thesis. Université catholique de Louvain, 2005.

[52] Tom Lancaster and Stephen J. Blundell. *Quantum Field Theory for the Gifted Amateur*. Oxford University Press, 2014. ISBN: 978-0-19-969933-9.

[53] Michael Tinkham. "Introduction to Superconductivity: Second Edition". In: 1 (2004), pp. 102–104.

[54] David Tong. *Lectures on Gauge Theory*. URL: http://www.damtp.cam.ac.uk/user/tong/gaugetheory.html (visited on 05/10/2023).

[55] A. A. Abrikosov. "On the Magnetic properties of superconductors of the second group". In: *Sov. Phys. JETP* 5 (1957), pp. 1174–1182.

[56] Holger Bech Nielsen and P. Olesen. "Vortex Line Models for Dual Strings". In: *Nucl. Phys. B* 61 (1973). Ed. by J. C. Taylor, pp. 45–61. DOI: 10.1016/0550-3213(73)90350-7.

[57] A. Vilenkin. "Gravitational Field of Vacuum Domain Walls and Strings". In: *Phys. Rev. D* 23 (1981), pp. 852–857. DOI: 10.1103/PhysRevD.23.852.

[58] M. B. Hindmarsh and T. W. B. Kibble. "Cosmic strings". In: *Rept. Prog. Phys.* 58 (1995), pp. 477–562. DOI: 10.1088/0034-4885/58/5/001. arXiv: hep-ph/9411342.

[59] H. Kleinert. "Critical Poperties of Phi4 Theories". In: (2001).

[60] Ken ' Ichi Saikawa. "A review of gravitational waves from cosmic domain walls". In: *Universe* 3.2 (Mar. 2017), p. 40. DOI: 10.3390/universe3020040. arXiv: 1703.02576v2. URL: http://arxiv.org/abs/1703.02576%20http://dx.doi.org/10.3390/universe3020040.

[61] William H. Press, Barbara S. Ryden, and David N. Spergel. "Dynamical Evolution of Domain Walls in an Expanding Universe". In: *Astrophys. J.* 347 (1989), pp. 590–604. DOI: 10.1086/168151.

[62] Theodore Garagounis and Mark Hindmarsh. "Scaling in numerical simulations of domain walls". In: *Phys. Rev. D* 68 (2003), p. 103506. DOI: 10.1103/PhysRevD.68.103506. arXiv: hep-ph/0212359.

[63] J. C. R. E. Oliveira, C. J. A. P. Martins, and P. P. Avelino. "The Cosmological evolution of domain wall networks". In: *Phys. Rev. D* 71 (2005), p. 083509. DOI: 10.1103/PhysRevD.71.083509. arXiv: hep-ph/0410356.

[64] P. P. Avelino, C. J. A. P. Martins, and J. C. R. E. Oliveira. "One-scale model for domain wall network evolution". In: *Phys. Rev. D* 72 (2005), p. 083506. DOI: 10.1103/PhysRevD.72.083506. arXiv: hep-ph/0507272.

[65] A. M. M. Leite and C. J. A. P. Martins. "Scaling Properties of Domain Wall Networks". In: *Phys. Rev. D* 84 (2011), p. 103523. DOI: 10.1103/PhysRevD.84.103523. arXiv: 1110.3486 [hep-ph].

[66] A. M. M. Leite, C. J. A. P. Martins, and E. P. S. Shellard. "Accurate Calibration of the Velocity-dependent One-scale Model for Domain Walls". In: *Phys. Lett. B* 718 (2013), pp. 740–744. DOI: 10.1016/j.physletb.2012.11.070. arXiv: 1206.6043 [hep-ph].

[67] C. J. A. P. Martins et al. "Extending the velocity-dependent one-scale model for domain walls". In: *Phys. Rev. D* 93.4 (2016), p. 043534. DOI: 10.1103/PhysRevD.93.043534. arXiv: 1602.01322 [hep-ph].

[68] Takashi Hiramatsu, Masahiro Kawasaki, and Ken'ichi Saikawa. "On the estimation of gravitational wave spectrum from cosmic domain walls". In: *JCAP* 02 (2014), p. 031. DOI: 10.1088/1475-7516/2014/02/031. arXiv: 1309.5001 [astro-ph.CO].

[69] Mark Hindmarsh. "Analytic scaling solutions for cosmic domain walls". In: *Phys. Rev. Lett.* 77 (1996), pp. 4495–4498. DOI: 10.1103/PhysRevLett.77.4495. arXiv: hep-ph/9605332.

[70] Mark Hindmarsh. "Level set method for the evolution of defect and brane networks". In: *Phys. Rev. D* 68 (2003), p. 043510. DOI: 10.1103/PhysRevD.68.043510. arXiv: hep-ph/0207267.

[71] Daniel Baumann. *Cosmology*. Cambridge University Press, July 2022. ISBN: 978-1-108-93709-2, 978-1-108-83807-8. DOI: 10.1017/9781108937092.

[72] George Efstathiou and Steven Gratton. "The evidence for a spatially flat Universe". In: *Mon. Not. Roy. Astron. Soc.* 496.1 (2020), pp. L91–L95. DOI: 10.1093/mnrasl/slaa093. arXiv: 2002.06892 [astro-ph.CO].

[73] Ya. B. Zeldovich, I. Yu. Kobzarev, and L. B. Okun. "Cosmological Consequences of the Spontaneous Breakdown of Discrete Symmetry". In: *Zh. Eksp. Teor. Fiz.* 67 (1974), pp. 3–11.

[74] A. Lazanu, C. J. A. P. Martins, and E. P. S. Shellard. "Contribution of domain wall networks to the CMB power spectrum". In: *Phys. Lett. B* 747 (2015), pp. 426–432. DOI: 10.1016/j.physletb.2015.06.034. arXiv: 1505.03673 [astro-ph.CO].

[75] D. Coulson, Z. Lalak, and Burt A. Ovrut. "Biased domain walls". In: *Phys. Rev. D* 53 (1996), pp. 4237–4246. DOI: 10.1103/PhysRevD.53.4237.

[76] Graciela B. Gelmini, Marcelo Gleiser, and Edward W. Kolb. "Cosmology of Biased Discrete Symmetry Breaking". In: *Phys. Rev. D* 39 (1989), p. 1558. DOI: 10.1103/PhysRevD.39.1558.

[77] Jean-Marc Dubois, Gilles Ouanounou, and Béatrice Rouzaire-Dubois. "The Boltzmann equation in molecular biology". In: *Progress in Biophysics and Molecular Biology* 99.2 (2009), pp. 87–93. ISSN: 0079-6107. DOI: https://doi.org/10.1016/j.pbiomolbio.2009.07.001. URL: https://www.sciencedirect.com/science/article/pii/S0079610709000522.

[78] D. Stauffer. "Scaling theory of percolation clusters". In: *Phys. Rept.* 54 (1979), pp. 1–74. DOI: 10.1016/0370-1573(79)90060-7.

[79] Sebastian E. Larsson, Subir Sarkar, and Peter L. White. "Evading the cosmological domain wall problem". In: *Phys. Rev. D* 55 (1997), pp. 5129–5135. DOI: 10.1103/PhysRevD.55.5129. arXiv: hep-ph/9608319.

[80] Masahiro Kawasaki, Ken'ichi Saikawa, and Toyokazu Sekiguchi. "Axion dark matter from topological defects". In: *Phys. Rev. D* 91.6 (2015), p. 065014. DOI: 10.1103/PhysRevD.91.065014. arXiv: 1412.0789 [hep-ph].

[81] Simone Blasi et al. "Friction on ALP domain walls and gravitational waves". In: *JCAP* 04 (2023), p. 008. DOI: 10.1088/1475-7516/2023/04/008. arXiv: 2210.14246 [hep-ph].

[82] L. D. (Lev Davidovich) Landau and E. M. (Evgeniĭ Mikhaĭlovich) Lifshits. "Quantum Mechanics : Non-Relativistic Theory." In: 2nd edition (1977), p. 72.

[83] Takashi Hiramatsu, Masahiro Kawasaki, and Ken'ichi Saikawa. "Gravitational Waves from Collapsing Domain Walls". In: *JCAP* 05 (2010), p. 032. DOI: 10.1088/1475-7516/2010/05/032. arXiv: 1002.1555 [astro-ph.CO].

[84] Masahiro Kawasaki and Ken'ichi Saikawa. "Study of gravitational radiation from cosmic domain walls". In: *JCAP* 09 (2011), p. 008. DOI: 10.1088/1475-7516/2011/09/008. arXiv: 1102.5628 [astro-ph.CO].

[85] Jean Francois Dufaux et al. "Theory and Numerics of Gravitational Waves from Preheating after Inflation". In: *Phys. Rev. D* 76 (2007), p. 123517. DOI: 10.1103/PhysRevD.76.123517. arXiv: 0707.0875 [astro-ph].

[86] Chiara Caprini et al. "General Properties of the Gravitational Wave Spectrum from Phase Transitions". In: *Phys. Rev. D* 79 (2009), p. 083519. DOI: 10.1103/PhysRevD.79.083519. arXiv: 0901.1661 [astro-ph.CO].

[87] Anson Hook, Gustavo Marques-Tavares, and Davide Racco. "Causal gravitational waves as a probe of free streaming particles and the expansion of the Universe". In: *JHEP* 02 (2021), p. 117. DOI: 10.1007/JHEP02(2021)117. arXiv: 2010.03568 [hep-ph].

[88] Takashi Hiramatsu et al. "Axion cosmology with long-lived domain walls". In: *JCAP* 01 (2013), p. 001. DOI: 10.1088/1475-7516/2013/01/001. arXiv: 1207.3166 [hep-ph].

[89] R. Rajaraman. *Solitons and Instantons. An Introduction to Solitons and Instantons in Quantum Field Theory*. 1982.

[90] Simone Blasi and Alberto Mariotti. "Domain Walls Seeding the Electroweak Phase Transition". In: *Phys. Rev. Lett.* 129.26 (2022), p. 261303. DOI: 10.1103/PhysRevLett.129.261303. arXiv: 2203.16450 [hep-ph].

[91] David J. Griffiths and Darrell F. Schroeter. *Introduction to Quantum Mechanics*. 3rd ed. Cambridge University Press, 2018. DOI: 10.1017/9781316995433.

[92] Kazunori Nakayama, Fuminobu Takahashi, and Norimi Yokozaki. "Gravitational waves from domain walls and their implications". In: *Phys. Lett. B* 770 (2017), pp. 500–506. DOI: 10.1016/j.physletb.2017.05.010. arXiv: 1612.08327 [hep-ph].

[93] A. Vilenkin. "Cosmic string dynamics with friction". In: *Phys. Rev. D* 43 (1991), pp. 1060–1062. DOI: 10.1103/PhysRevD.43.1060.

[94] Prateek Agrawal et al. "Axion string signatures II: A cosmological plasma collider". In: (Oct. 2020). arXiv: 2010.15848v2. URL: http://arxiv.org/abs/2010.15848.

[95] Virgile Dandoy, Valerie Domcke, and Fabrizio Rompineve. "Search for scalar induced gravitational waves in the International Pulsar Timing Array Data Release 2 and NANOgrav 12.5 years dataset". In: (Feb. 2023). arXiv: 2302.07901 [astro-ph.CO].

[96] Guan-Sen Wang et al. "SKA sensitivity for possible radio emission from dark matter in Omega Centauri". In: (Mar. 2023). arXiv: 2303.14117 [astro-ph.HE].

[97] K. G. Arun et al. "New horizons for fundamental physics with LISA". In: *Living Rev. Rel.* 25.1 (2022), p. 4. DOI: 10.1007/s41114-022-00036-9. arXiv: 2205.01597 [gr-qc].

[98] C. Cutler and J. Harms. "BBO and the neutron-star-binary subtraction problem". In: *Phys. Rev. D* 73 (2006), p. 042001. DOI: 10.1103/PhysRevD.73.042001. arXiv: gr-qc/0511092.

[99] Daniel Finstad, Laurel V. White, and Duncan A. Brown. "Prospects for a precise equation of state measurement from Advanced LIGO and Cosmic Explorer". In: (Nov. 2022). arXiv: 2211.01396 [astro-ph.HE].

[100] Antonino Chiummo. "The Einstein Telescope: Status of the project". In: *EPJ Web Conf.* 280 (2023), p. 03003. DOI: 10.1051/epjconf/202328003003.

[101] B. P. Abbott et al. "Prospects for observing and localizing gravitational-wave transients with Advanced LIGO, Advanced Virgo and KAGRA". In: *Living Rev. Rel.* 21.1 (2018), p. 3. DOI: 10.1007/s41114-020-00026-9. arXiv: 1304.0670 [gr-qc].

[102] Richard A. Battye, Apostolos Pilaftsis, and Dominic G. Viatic. "Simulations of Domain Walls in Two Higgs Doublet Models". In: *JHEP* 01 (2021), p. 105. DOI: 10.1007/JHEP01(2021)105. arXiv: 2006.13273 [hep-ph].

[103] Chiara Caprini et al. “Reconstructing the spectral shape of a stochastic gravitational wave background with LISA”. In: *JCAP* 11 (2019), p. 017. DOI: 10.1088/1475-7516/2019/11/017. arXiv: 1906.09244 [astro-ph.CO].

[104] Lucia Trozzo and Francesca Badaracco. “Seismic and Newtonian Noise in the GW Detectors”. In: *Galaxies* 10.1 (2022), p. 20. DOI: 10.3390/galaxies10010020.

[105] Janyce Franc et al. “Mirror thermal noise in laser interferometer gravitational wave detectors operating at room and cryogenic temperature”. In: (Dec. 2009). arXiv: 0912.0107 [gr-qc].

[106] Mario Gutierrez Abed. “Numerical Cosmology Bubble Nucleation & Scalar Fields in Numerical Relativity”. MA thesis. Newcastle U., United Kingdom, July 2020.

[107] V. Rabinovich and F. Urbano-Altamirano. “Application of the SPPS method to the one-dimensional quantum scattering”. In: *Communications in Mathematical Analysis* 17.2 (2014), pp. 295–310. URL: https://ipn.elsevierpure.com/en/publications/application-of-the-spps-method-to-the-one-dimensional-quantum-sca.